A NUMERICAL STUDY ON NON-EQUILIBRIUM MULTI-TEMPERATURE THERMO-CHEMISTRY

A Dissertation
Presented to
The Academic Faculty

by

Pratibha Raghunandan

In Partial Fulfillment
of the Requirements for the Degree
Doctor of Philosophy in the
School of Aerospace Engineering

Georgia Institute of Technology

May 2019

A NUMERICAL STUDY ON NON-EQUILIBRIUM MULTI-TEMPERATURE THERMO-CHEMISTRY

Approved by:

Prof. Stephen Ruffin, Advisor
School of Aerospace Engineering
Georgia Institute of Technology

Prof. Jechiel Jagoda
School of Aerospace Engineering
Georgia Institute of Technology

Prof. Suresh Menon
School of Aerospace Engineering
Georgia Institute of Technology

Dr. Wenting Sun
School of Aerospace Engineering
Georgia Institute of Technology

Dr. Suman Muppidi
Aerothermodynamics Branch
NASA Ames Research Center

Date Approved: March 27, 2019

ACKNOWLEDGEMENTS

First, I would like to thank my advisor Prof. Stephen Ruffin for providing an opportunity to pursue this thesis, and for mentoring me during my graduate studies. It was a great pleasure to learn from such an inspiring educator, and to be given the independence to pursue my own learning in graduate school. I am grateful for the advice, encouragement and fellowships he provided for my academic pursuits. I would also like to thank members of my dissertation committee: Prof. Jechiel Jagoda, Prof. Suresh Menon, Dr. Wenting Sun and Dr. Suman Muppidi for reviewing my thesis amidst their busy schedules. The financial support received by the School of Aerospace Engineering during the course of my education is gratefully acknowledged.

I would like to express my heartfelt gratitude to Prof. Jagoda for being caring and supportive of me throughout my doctoral education. I thank him for instilling hope, and for the several pleasant conversations about research, education and life. Special thanks are also due to Dr. David Hash for his mentorship, encouragement, and for providing a wonderful and memorable summer at NASA Ames Research Center during my graduate studies. I would like to thank several scholars such as Brett Cruden, Suman Muppidi, Jeffrey Hill, Ryan McDaniel, Joshua Monk and Chun Tang for all the help and feedback provided while at Ames.

I would like to thank all AE faculty and staff that I was able to learn from and interact with. My gratitude is due to Prof. Jerry Seitzman for the countless hours that he spent over the years in training me in experimental studies and for the encouragement he provided. Thanks also to Prof. Brian German, Prof. Mitchell Walker and all other supervising faculty for their support in teaching activities. I would like to thank the research engineers at the Combustion Lab, Mr. Scott Moseley, Mr. Scott Elliott, Mr. Henry Russell, Ms. Tasha Koon, Mr. Howard Simpson and Mr. Jinwoo Lee for the help provided in various forms since the start of my education at Georgia Tech, and for doing it so readily and joyfully.

I am thankful to the past and present members of the Aerothermodynamics, Research and Technology lab, and my friends for their companionship over the years. The words of wisdom imparted by Susheel when I started the program at Tech helped me at critical

times and must not go unmentioned. The times spent with Matthew and David in the lab and during our outdoor adventures made graduate school enjoyable.

Finally, it would not have been possible to pursue this challenging journey in my life without the support and encouragement received by my family. I am thankful to them for their many sacrifices and for inspiring through all their achievements.

TABLE OF CONTENTS

ACKNOWLEDGEMENTS iii

LIST OF TABLES viii

LIST OF FIGURES ix

NOMENCLATURE xiv

SUMMARY xvii

1 INTRODUCTION 1

1.1 Problem Definition and Importance 1

1.2 Overview of Previous Research 3

1.2.1 Multi-Temperature Modeling 3

1.3 Objectives and Scope of Proposed Study 7

2 GOVERNING EQUATIONS 9

2.1 Introduction 9

2.2 Assumptions 9

2.3 Mathematical Formulation 10

2.3.1 Equations of State and Other Ancillary Relations 11

2.4 Energy Exchange Rate Equations 12

2.5 Chemical Model 14

3 NUMERICAL METHODS 16

3.1 Introduction 16

3.2 NASCART-GT 16

3.3 Governing Equations in Vector Form 17

3.4 AUSMPW+ Scheme for Weakly Ionized Flows 18

3.5 Point Implicit Scheme 20

3.6 Calculation of temperatures 20

4 NON-EQUILIBRIUM RATE RESULTS 22

4.1 Introduction 22

4.2 Previous Studies on Heat Baths 23

4.3 Thermo-Chemical Relaxation Rates: Two-Temperature Model 25

4.3.1 Universal transition phase 27

4.3.2 Modeling Effects: Non-Preferential models 33

4.3.3 Molecular/Atomic Effects 36

4.3.4 Pressure Effects 38

4.4 Thermo-Chemical Relaxation Rates: Multi-Vibrational, Single Translational Temperature Model 42

4.4.1 Numerical definition of equilbrium characteristics 46

4.4.2 Variation of Initial Temperature Difference 47

5 HYPERSONIC FLOW RESULTS FOR MULTI-TEMPERATURE MODELS 49

5.1 Introduction 49

5.2 Conical flows 49

5.3 Double wedge flows 56

5.3.1 Effect of freestream Mach number 57

5.3.2 Effect of second wedge angle 67

5.4 Cylinder flow 76

5.4.1 Two temperature model 76

5.4.2 Multi-vibrational, single translational temperature model 78

5.4.3 Multi-vibrational, two translational temperature model 78

5.4.4 Sensitivity to chemical kinetics 79

6 CONCLUSIONS 102

6.1 Numerical Implementation 102

6.2 Conclusions from Finite Heat Bath Results 103

6.3 Conclusions from Hypersonic Flow Simulations 104

6.4 Key findings of numerical study 106

6.5 Recommendations for future work 107

REFERENCES 114

LIST OF TABLES

4.1 Effects of initial pressure in an O_2-N heat bath system 38

4.2 Effects of initial thermal non-equilibrium 47

5.1 Freestream conditions used for the cylinder test case 76

LIST OF FIGURES

4.1 Validation of the present code developed, NASCART-GT, with results obtained by Boyd et al. 27

4.2 Two temperature heat bath results for an initial mole fraction of O_2 of 0.1 . 28

4.3 Two temperature model temperature results for varying initial mole fractions of an O_2-N_2 system 28

4.4 Two temperature model enthalpy results for varying initial mole fractions of an O_2-N_2 system 29

4.5 Two temperature model temperature results for varying initial mole fractions of an O_2-N system 29

4.6 Two temperature model enthalpy results for varying initial mole fractions of an O_2-N system 30

4.7 Two temperature model results for initial mole fractions of an O_2-N_2 system in the range of 0.1 and 0.2 30

4.8 Two temperature model results for initial mole fractions of an O_2-N system in the range of 0.1 and 0.2 31

4.9 Time accurate Gibb's free energy results for an O_2-N_2 system at 1 atm . . . 32

4.10 Variation in non-equilibrium temperatures between T-based and $\sqrt{TT_v}$ non-preferential models 34

4.11 Variation in non-equilibrium mass fractions between two non-preferential models 35

4.12 Time accurate Gibb's free energy results for an O_2-N system at 1 atm using a $\sqrt{TT_v}$ model 37

4.13 Time accurate Gibb's free energy results for an O_2-N system at 0.1 atm using a $\sqrt{TT_v}$ model 39

4.14 Time accurate mass fractions for an O_2-N system at different pressures using a $\sqrt{TT_v}$ model 40

4.15 Time accurate mass fractions for an O_2-N system at different pressures using a $\sqrt{TT_v}$ model 41

4.16 Comparisons between select multi-vibrational and two-temperature heat bath results for initial mole fraction of O_2 of 0.1 in an O_2-N_2 system 43

4.17 Comparisons between select multi-vibrational and two-temperature heat bath results for initial mole fraction of O_2 of 0.5 in an O_2-N_2 system 43

4.18 Comparisons between select multi-vibrational and two-temperature temperature model mass fraction results for initial mole fraction of O_2 of 0.1 in an O_2-N_2 system 44

4.19 Comparisons between select multi-vibrational and two-temperature temperature model mass fraction results for initial mole fraction of O_2 of 0.5 in an O_2-N_2 system 44

4.20 Comparison of equilibrium characteristics between two temperature and multi-vibrational temperature model results 46

4.21 Equilibrium temperature surface response to variations in initial mole fraction of O_2 and initial temperature difference between the translational and vibrational modes: T_{tr} = 10000 K 48

4.22 Equilibrium inter-species relaxation time (between O_2-O_2, O_2-N_2 and N_2-N_2) surface response to variations in initial mole fraction of O_2 and initial temperature difference between the translational and vibrational modes: T_{tr} = 10000 K 48

5.1 Computational grid used for a 45^0 1/2 cone angle geometry thermo-chemical non-equilibrium simulation in NASCART-GT 50

5.2 Pressure contours for a 45^0 1/2 cone angle geometry simulations 51

5.3 Mach contours for a 45^0 1/2 cone angle geometry simulations 52

5.4 Temperature contours for a 45^0 1/2 cone angle geometry simulations 53

5.5 Comparison between NASCART-GT results and Spurk's data for a 45^0 1/2 angle cone for a Mach 9.42 flow of O_2. 54

5.6 Schematic diagrams of Type VI (a) and Type V (b) interactions [72] 58

5.7 Computational grids in NASCART-GT for a Double Wedge using a calorically perfect gas, chemical non-equilibrium and thermo-chemical non-equilibrium assumptions: θ_1 = 15 and θ_2 = 45 in Mach 9 air flow 59

5.8 Comparison of computational grids in NASCART-GT for a Double Wedge using calorically perfect gas air assumptions at M_∞ = 11 (left) and at M_∞ = 15 (right): θ_1 = 15 and θ_2 = 45 60

5.9 Comparison of computational grids in NASCART-GT for a Double Wedge using chemical non-equilibrium (1-temperature model) at M_∞ = 11 (left) and at M_∞ = 15 (right): θ_1 = 15 and θ_2 = 45 61

5.10 Comparison of computational grids in NASCART-GT for a Double Wedge using thermo-chemical non-equilibrium (2-temperature model) at M_∞ = 11 (left) and at M_∞ = 15 (right): θ_1 = 15 and θ_2 = 45 61

5.11 Mach and Temperature contours using a calorically perfect gas model for a Double Wedge: θ_1 = 15 and θ_2 = 45 in Mach 9 air flow 62

5.12 Mach and temperature contours using a one temperature model for a Double Wedge: θ_1 = 15 and θ_2 = 45 in Mach 9 air flow 62

5.13 Mass fraction contours using a one temperature gas model for a Double Wedge: θ_1 = 15 and θ_2 = 45 in Mach 9 air flow 63

5.14 Double wedge results obtained by Coratekin et al. [69]: $\theta_1 = 15^0$, $\theta_2 = 45^0$, M_∞ = 11 with calorically perfect gas assumptions 64

5.15 Mach and Temperature contours using a calorically perfect gas model for a Double Wedge: θ_1 = 15 and θ_2 = 45 in Mach 11 air flow 64

5.16 Mach and Temperature contours using a one-temperature gas model for a Double Wedge: θ_1 = 15 and θ_2 = 45 in Mach 11 air flow 64

5.17 Mach contours using a two-temperature gas model for a Double Wedge: θ_1 = 15 and θ_2 = 45 in Mach 11 air flow 65

5.18 Translational and Vibrational Temperature contours using a two-temperature gas model for a Double Wedge: θ_1 = 15 and θ_2 = 45 in Mach 11 air flow . . 65

5.19 Mass fraction contours using a two temperature gas model for a Double Wedge: θ_1 = 15 and θ_2 = 45 in Mach 11 air flow 66

5.20 Mach and temperature contours using a calorically perfect gas model for a Double Wedge: θ_1 = 15 and θ_2 = 45 in Mach 15 air flow 67

5.21 Mach and temperature contours using a one temperature gas model for a Double Wedge: θ_1 = 15 and θ_2 = 45 in Mach 15 air flow 68

5.22 Mass fraction contours using a one temperature gas model for a Double Wedge: θ_1 = 15 and θ_2 = 45 in Mach 15 air flow 69

5.23 Mach Contours in NASCART-GT for a Double Wedge using a calorically perfect gas assumptions for θ_2 = 46.3 (left) and θ_2 = 48 (right): θ_1 = 15 and M_∞ = 11 70

5.24 Mach Contours in NASCART-GT for a Double Wedge using chemical non-equilibrium for θ_2 = 46.3 (left) and θ_2 = 48 (right) : θ_1 = 15 and M_∞ = 11 . 71

5.25 Mass fraction contours using a one temperature gas model for a Double Wedge: θ_1 = 15 and θ_2 = 46.3 in Mach 11 air flow 72

5.26 Mass fraction contours using a one temperature gas model for a Double Wedge: θ_1 = 15 and θ_2 = 48 in Mach 11 air flow 73

5.27 Surface pressure distributions along the double wedge using calorically perfect gas assumptions: θ_1 = 15 and Mach 11 air flow 74

5.28 Surface pressure distributions along the double wedge using chemical non-equilibrium: θ_1 = 15 and Mach 11 air flow 74

5.29 Surface pressure distributions along the double wedge using thermo-chemical non-equilibrium: θ_1 = 15 and Mach 11 air flow 75

5.30 NASCART-GT and DPLR Computational grid for a cylinder in Mach 12.7 air 81

5.31 Comparative stagnation line density and pressure for a cylinder in a 5-species Mach 12.7 air flow between NASCART-GT and DPLR 82

5.32 Comparative stagnation line temperatures and mole fractions for a cylinder in a 5-species Mach 12.7 air flow between NASCART-GT and DPLR 83

5.33 Comparative shock stand-off distances between experimental cold hypersonic wind tunnel data (γ = 1.4) and present result using a two-temperature thermo-chemical model for cylinder flows 84

5.34 NASCART-GT and DPLR Translational temperature contours for a cylinder in Mach 12.7 air 85

5.35 NASCART-GT and DPLR Vibrational temperature contours for a cylinder in Mach 12.7 air 86

5.36 NASCART-GT and DPLR Density contours for a cylinder in Mach 12.7 air 87

5.37 NASCART-GT and DPLR Pressure contours for a cylinder in Mach 12.7 air 88

5.38 NASCART-GT and DPLR N_2 mole fraction contours 89

5.39 NASCART-GT and DPLR O_2 mole fraction contours 90

5.40 NASCART-GT and DPLR NO mole fraction contours 91

5.41 NASCART-GT and DPLR N mole fraction contours 92

5.42 NASCART-GT and DPLR O mole fraction contours 93

5.43 N_2 vibrational temperature contours using a multi-vibrational temperature formalism: A cylinder in a Mach 12.7 5-species air 94

5.44 O_2 vibrational temperature contours using a multi-vibrational temperature formalism: A cylinder in a Mach 12.7 5-species air 94

5.45 NO vibrational temperature contours using a multi-vibrational temperature formalism: A cylinder in a Mach 12.7 5-species air 95

5.46 NO+ mole fraction contours using a multi-vibrational temperature formalism: A cylinder in a Mach 12.7 7-species air 95

5.47 Comparative stagnation line density and pressure for a cylinder in a 7-species Mach 12.7 air flow 96

5.48 Comparative stagnation line translational and vibrational temperatures for a cylinder in a 7-species Mach 12.7 air flow 97

5.49 NO+ mole fraction contours using a multi-vibrational temperature, two translational temperature formalism: A cylinder in a Mach 12.7 7-species air . . 98

5.50 Plasma pressure contours using a multi-vibrational, two-translational temperature formalism: A cylinder in a Mach 12.7 7-species air 98

5.51 Comparative stagnation line density and pressure for a cylinder in a 5 5- and 7-species Mach 12.7 air flow 99

5.52 Comparative stagnation line translational and vibrational temperatures for a cylinder in a 5- and 7-species Mach 12.7 air flow 100

5.53 Comparative stagnation line mole fractions using a 2-temperature and multi-vibrational temperature for a cylinder in a 7-species Mach 12.7 air flow . . . 101

5.54 Comparative stagnation line mole fractions for a cylinder in a 5- and 7-species Mach 12.7 air flow 101

NOMENCLATURE

A	Pre-exponential factor in the Arrhenius rate, constant in polynomial expansion
B	Constant in polynomial expansion
c_v	Specific heat at constant volume
C	Constant in polynomial expansion
d	Diameter of molecule
D	Constant in polynomial expansion, Diameter
δ	Shock stand-off distance
δ_{ij}	Kronecker delta function
E	Energy, constant in polynomial expansion
e	Internal energy
F	Constant in polynomial expansion
f	Pressure-based weight function
$\vec{\boldsymbol{F}}, \vec{\boldsymbol{G}}$	Flux vectors in x and y directions respectively
$\hat{g}$	Gibb's free energy per unit mole
h	Planck's constant, enthalpy
h_0	Enthalpy of formation
$\boldsymbol{I}$	Identity matrix
k	Reaction rate
k_B	Boltzmann constant
m	Mach number
M	Molecular weight (of species s), Mach number
μ_{sr}	Effective molecular weight due to species s and r
$\hat{N}$	Avogadro number
N_s	Total number of species s in the mixture
N_R	Number of reactions
ν	Stoichiometric coefficient, vibrational level

ω	Rate of production, weight function
p	Pressure
P	Probability of collision (between species s and r)
$\boldsymbol{P}$	Pressure flux vector
$\boldsymbol{\Phi}$	Convective flux vector
Q	Source Term
$\vec{\boldsymbol{R}}$	Vector denoting the sum total of flux terms
$\bar{R}$	Universal gas constant
ρ	Density
$\vec{\boldsymbol{S}}$	Source vector due to chemical reactions & vibrational excitations
σ_{sr}	Collision cross-section between vibrating species s and r
t	Time
T	Temperature
θ	Characteristic temperature
τ	Relaxation time or Inter-species relaxation time
$\vec{\boldsymbol{U}}$	State vector
u	Velocity in the x-direction
V	Cell volume
v	Velocity in the y-direction
x	Distance along the Cartesian x-direction
X	Mole fraction
y	Distance along the Cartesian y-direction
Y	Mass fraction
Z	charge

Subscript

atm	Atmospheres
b	Backward reaction
c	Equilibrium
ds	Dissociation
e	Electron
eq	Equilibrium
eff	Effective (reaction rate or temperature)
$e-T$	Electron-translation energy exchange
$e-V$	Electron-vibration energy exchange
f	Forward reaction
N_s	Total number of species in the mixture
p	Pressure-based
rot	Rotational energy
i	Species i in a gaseous mixture
i, j	Unit vectors along Cartesian directions
L	Left
$L-T$	Landau-Teller
R	Right
s, r	Vibrating species s or r in the mixture
rk, sr	between species r and k, and s and r respectively
t	Total (energy)
tr	Translational (energy or temperature)
$T-V$	Translation-vibration energy exchanges
$V-V$	Vibration-vibration energy exchanges
ve, vib	Vibrational energy
v	Vibration
$\frac{1}{2}$	At cell interface

Superscript

n	Exponential factor for temperature dependence of reaction rate
$*$	Equilibrium state
$'$	of reactants
$''$	of products
n	size of square matrix

SUMMARY

The accurate computation of hypersonic flowfields is an ongoing endeavor and is important for the accurate prediction of heat transfer and space vehicle design. The governing equations for hypersonic flowfields have been evolving from multi-temperature modeling, state-to-state modeling to the more recent reduced order modeling. Of the various models existing till date of varying levels of complexity, multi-temperature modeling continues to be the most widely implemented and computationally least expensive form of modeling hypersonic flows. This thesis explores the resulting physics from various forms of multi-temperature modeling.

The non-equilibrium flows at typical hypersonic re-entry conditions can be modeled by considering varying extents of non-equilibrium: chemical, thermo-chemical with the typical two temperature formalism, and thermo-chemical with more than two temperatures used to represent the gas under consideration. Most initial numerical verification studies examine non-equilibrium relaxation rates using zero-dimensional heat bath systems. Literature abounds with heat bath relaxation rate studies at isothermal conditions, and consequently for very dilute systems with negligible chemical non-equilibrium. Nonetheless, the same verified representative equations, including the Landau-Teller translation-vibration energy exchange, are used to compute multi-dimensional flows involving high degrees of chemical non-equilibrium. Thus, despite a well-established understanding of the temperature limitations of Park's empirical two-temperature model, and the original form of the Landau-Teller formulation, the effects of system dilution levels on the resulting non-equilibrium characteristics have not been well understood. The present work focuses on the effects of such dilution on the thermo-chemical non-equilibrium characteristics of isochoric, finite heat baths represented by varying resolutions of multi-temperature models.

The non-equilibrium characteristics for such heating systems reveal non-linear effects in attaining thermal non-equilibrium which are enhanced by the mixing-type Millikan-White relaxation time empirical curve fit. Multi-vibrational, single translational temperature modeling leads to significantly altered time-scales of non-equilibrium chemistry relative to a simple two-temperature model representation for internal energy. This was further confirmed

during the two-dimensional flows studied where thermo-chemical modeling with first order effects exhibited altered shock stand-off, near-surface temperatures, and flow field chemistry with multi-vibrational, single translational temperature modeling.

The implementation of an increased resolution of thermal non-equilibrium representation for any weakly ionized flows present in the system closely followed the trends exhibited by a system in which electron and heavy particle translational temperatures were assumed to be in equilibrium with each other. However, the shock structure showed an enhanced sensitivity to a more complete representation of the underlying chemical kinetics.

For the aerothermodynamics community, this work contributes to understanding the resultant thermo-chemical non-equilibrium rate effects for various forms of representing the effective temperature of a reaction, within a multi-temperature modeling perspective. In particular, it emphasizes the temporal and spatial sensitivity of non-equilibrium energy modeling approaches for various zero-dimensional and two-dimensional flow fields. Such intermediate non-equilibrium chemistry effects could be leveraged for aerodynamic flow control and controlled heat transfer applications.

CHAPTER 1
INTRODUCTION

1.1 Problem Definition and Importance

Hypersonic flight, is the subject of heightened interest in light of the development of new experimental diagnostic techniques for ground based tests, and improved numerical modeling. The evolution of hypersonic designs, from the era of the National Aero-Space Plane (NASP) program to more recent programs such as the X-51A, HyFly [1], and Hypersonic Testing Vehicle-2 (HTV-2), has been made possible by CFD computations that well support experimental findings.

In the pursuit of expanding the operational envelope of this frontier, accurate aerothermal loading predictions, and a correct understanding of the flow physics associated at intermediate and high Mach numbers are of prime importance. Such Mach numbers yield significant dissociation and ionization during atmospheric re-entry, and necessitate modeling of themal, chemical and ionizational non-equilibrium to predict the associated aerothermodynamics. Such non-equilibrium modeling has many applications including plasma aerodynamics, magneto-hydrodynamic(MHD) flow control, drag reduction techniques, and for telemetry blackout mitigation.

The development of governing equations for hypersonic flow fields involves the solution to the conservation of species mass, momentum, and energy equations for neutral species and charged particles. These governing equations in their complete form, as is used currently in literature, include translation-vibration (T-V), vibration-vibration (V-V), translation-electron (T-e) and electron-vibration (e-V) energy exchange rate equations. The range of applicability of these equations to expanding and compressible flows, as well as, across a wide range of temperatures has been typically investigated through solutions to master equations that include various state-to-state transitions. Macroscopic thermal and chemical models offer quick solutions for multi-dimensional flows.

Despite several macrosopic and state-to-state models that exist in literature, the non-

compliance of numerical models with experimental ground-based or flight test results is still intriguing [2, 3, 4]. Discrepancies can be found between these studies with regard to electron number densities obtained. A recent study by Surzhikov and Shang [5] demonstrated the variations in stagnation point and surface electron density predictions between various models using different chemical kinetics models. Some of the common chemical kinetics models used are those of Park [6], Treanor-Marrone [7] and Marrone-Treanor [8]. While the study [5] described above found that the satisfactory prediction of electron densities was attainable at all altitudes by coupling the Park's model with the Marrone-Treanor model, determination of universally suitable physical and chemical kinetics models is still an open problem, one that some recent studies [9, 10, 11] have begun to examine.

While validation with flight test data presents challenges as described above, ground-based tests and computation of corresponding data at hypersonic planetary entry conditions also present challenges. These include accurate determination of flow conditions [12], the ability to define the test medium or environment [13], the need for special instrumentation in any existing plasma environment, to name a few. The ability to numerically determine the flow fields for weakly ionized gases present in such ground-based tests hinges upon understanding the physics associated with such environments, as well as factoring in the important limitations of the facilities. The consideration of such key parameters are imperative to determine suitable chemical and physical models for hypersonic gases.

The present work proposes to systematically examine the effects of various macroscopic thermo-chemical non-equilibrium models on the resultant equilibration rates in static environments, as well as to examine the flow physics in hypersonic high-temperature environments. The next section presents an overview of some of the relevant experimental and computational work in the numerical study of hypersonic gases. In addition, the thermal non-equilibrium models developed thus far are also discussed.

The attainment of the overall goal discussed above can be made possible through a series of objectives as presented in section 1.3 of this chapter.

1.2 Overview of Previous Research

The governing physico-chemical processes, such as dissociation and ionization of the constituent molecules, depend upon the shock intensity in hypersonic flow. Several metrics of interest for accurate aerothermal loading predictions, such as, internal energy distribution functions, resulting shock stand-off distances, and concentration of gas species, stem from the use of appropriate models describing the underlying non-equilibrium processes. The energy exchange rates have a particularly significant effect on such predictions.

Some of the most commonly used models in the aerospace community are the multi-temperature models where the gas under consideration is assumed to possess multiple temperatures such as a translational temperature, a vibrational temperature, or electronic temperature, if applicable. However, the applicability poses challenges as the models have inherent uncertainties that are hard to quantify and define universally [14]. Some of the uncertainties in multi-temperature models, as stated by Park [15], include the accuracy of determination of chemical reaction rates, the influence of state-specific reactions in Zeldovich processes [16], and the influence of over-population of high vibrational states on the flow around a body. The following section outlines some of the work performed in analyzing such multi-temperature models.

1.2.1 Multi-Temperature Modeling

Multi-temperature models are quite computationally inexpensive to apply to multi-dimensional flow codes. Such multi-temperature fomulations primarily emerged from the two-temperature model. In a seminal work on two-temperature models, one representing translating temperatures of all atoms/molecules, and the second representing the vibrational temperature of all diatomic molecules, Park[17] was able to effectively capture the important features of non-equilibrium flow. This model, which is one level more sophisticated than the one temperature model commonly used for all chemically reacting flows, was derived based on the following principal assumptions, as stated by Park in a recent study [18]:

(i) “A quasi-steady state distribution of internal energy

(ii) Preferential dissociation and ionization phenomena

(iii) Diffusional model for vibrational relaxation, and

(iv) Collision limiting correction for vibrational relaxation times"

This two-temperature resolution was able to successfully explain the radiation overshoot phenomenon as well as the observed radiation in expanding nozzles. However, at low temperatures, the important consideration of rotational temperature was ignored. In addition, there were a few violations of assumptions at high temperatures. These include, the energy content in the rotational mode is less than $k_B T$ at temperatures beyond 30,000 K, the optimal range for vibrational and electronic excitation extends from 7000 K to 12,000 K, and extrapolation of rate coefficients were made from data that are known to be valid only below 10,000 K.

Several studies [19, 20] have been carried out recently that examine the coupling of rotational and vibrational modes. At sufficiently high temperatures (>= 1000 K), vibration-rotation coupling has been observed through experimental shock tube experiments [21]. At temperatures below approximately 1000 K, although vibration-translation coupling was shown to be absent, slower rotational relaxations (compared to vibrational relaxation) were observed at high translational temperatures. Recent studies [20] on thermochemical modeling of electronically excited molecular oxygen also confirm that rotational temperatures need to be considered at high temperatures. However, their heat bath studies indicated that this deciding cut-off temperature is 10000 K. Another study [22] on isochoric N_2 systems also identified the need to incorporate rotational-vibrational, or rovibrational, states at high temperatures. With increasing computational resources, dissociation-rovibrational coupling using master equations are being studied [23]. However, the lack of empirical rovibrational energy coupling models for dissociated air does not allow for their incorporation in to macroscopic multi-temperature models.

In the development of a holistic set of macroscopic thermo-chemical non-equilibrium governing equations for weakly ionized hypersonic flows, Candler [2] utilized electron-vibration energy exchanges with diatomic nitrogen only, whereby the rate of energy transfer between the electron translational energy mode and the nitrogen vibrational energy mode was set to be proportional to the energy transfer rate between the two energy levels and the number density of the electrons. The original expression for this energy transfer rate was developed

by Lee [24], and involved the solution for master equations accounting for transitions from multiple vibrational energy levels. Candler matched the electron-relaxation time to the results of Lee using quadratic forms of the logarithmic electron temperature. An important aspect about this quadratic form is that there was a strong resonance observed between the electron and vibrational modes near 7000 K, with a quick departure from this value observed at other temperatures. Bourdon and Vervisch [25] remodeled the coefficient of the vibrational excitation rate of N_2 by electrons with a polynomial function of electron temperature. However, it was found that the electron-vibrational relaxation time resulted in negative rate coefficients below 2000 K and above 50,000 K. More recently, Kim et al. [26] have further modified this rate coefficient term and have successfully shown, through explicit and implicit methods, that significant thermal non-equilibrium at very high and low electron temperatures can be modeled. Furthermore, they were able to replicate the theoretical findings of Lee in this regard. However, a common finding from the original work, later studies, as well as Kim et al.'s [26] recent work is that the e-V excitation rate coefficients differ significantly from the experimental results for higher vibrational states. The causes of the differences between experimental and numerical results are yet to be addressed. The prediction of ionization dynamics behind a shock wave is largely dependent on identifying the major source terms or the electron energy budget. In a study by Guy et al. [27] involving vibrationally excited N_2 and electronically excited N, it was found that the e-V source term was the major energy creation term followed by the replacement with the electron-ions elastic energy exchange term. Such an energy budget determination using state-to-state models has resulted in macroscopic multi-internal temperature models that predict weaker e-V coupling than other models existent in literature.

Other high temperature studies for non-equilibrium plasmas have focused on chemical reaction rates. Reaction rate coefficients that can be used up to a temperature of 30,000 K were proposed [28] in 1990 that included electron-number density corrections for the transport properties of charged species. In their study, Gupta et al. [28] found that accounting for non-rigidity of rotors and anharmonicity of oscillators improved high temperature predictions.

In a very recent work by Liu et al. [29], macroscopic moment equations and rate co-

efficients have been obtained from microscopic equations using the method of weighted residuals. Their work has demonstrated that macroscopic internal energy transfer occurs through non-linear collisional processes. In addition, the resultant macroscopic models obtained from grouping of microscopic equations show significant deviations from the Landau Teller rate equations for the description of vibrational relaxation. It has been envisioned that the application of such grouping techniques to microscopic models in order to obtain macroscopic equations help better predict thermal and chemical non-equilibrium for a broad range of problems [29, 30] than existing empirical models. Grasso and Capano [31], through their simulations, showed that ionization is an inviscid phenomenon in the presence of a strong bow shock. They also found that charged particles formed near the stagnation zone are convected away and recombine due to flow expansion. Other recent work on weakly ionized hypersonic flows have been more focussed on modeling them for rarefied flows [32, 33]. In DSMC [32] and CFD simulations [2] the electron number densities were found to be sensitive to the dissociation model as the associative ionization reaction involved only atoms as reactants.

Very recent efforts with respect to simulating the plasma sheath to study radio blackout include using chemical non-equilibrium and Park's two temperature model by Qian et al.[34]. It was seen in this study that the plasma sheath region becomes prominent between Mach 7 and Mach 8 when the incident EM incident wave frequency is greater than 1 GHz. The effect of plasma sheath on the Backscattering Radar Cross-Section (BRCS) was found to be negligible for incident frequencies greater than 300 MHz. While the study did conclude about some key parameters for BRCS, it did not include realistic geometries and required greater parametic variations to lead to conclusive plasma sheath effects. Kim et al. [35] found that the reduction of the plasma number density of the plasma layer, through the creation of an $E \times B$ layer allowed for radio signals to be transmitted through the plasma layer. Other efforts to mitigate blackout include aerodynamic shaping, use of magnetic windows, liquid injection and quenching of reentry plasma using ceramic metal-oxide particulates [36]. Angle of attack studies [37], for signals of the order of a THz, have indicated that the signal strength can be weakened if it gets bracketed between the range of 0 deg - 10 deg. Such studies, however, do need to incorporate complex non-linear convection

effects to produce more definitive effects of plasma density on transmission of waves.

1.3 Objectives and Scope of Proposed Study

From the discussion in the previous section on studies performed on hypersonic flows, it can be concluded that successful validation of numerical simulations using experimental data is highly dependent on the modeling of internal energy. Irreversible thermodynamic and nonequilibrium chemical kinetics is often considered to be the pacing item for hypersonic flow simulations [38]. In the light of all these studies, the following research questions are developed for the thesis:

(i) Are the current empirical relaxation models adequate for hypersonic flows?

(ii) What degree of thermo-chemical coupling is required for the accurate prediction of non-ionized and weakly ionized hypersonic flows?

The overarching goal of this thesis is to perform a systematic study of the resultant flow physics observed in non-equilibrium gas mixtures and hypersonic flows upon the implementation of various macroscopic energy exchange models on an adaptive Cartesian grid-based flow solver. The effects of using different macroscopic internal energy models for non-equilibrium flows are not fully understood yet in this field. This work is intended to contribute to an increased comprehension through achieving several non-equilibrium simulation capabilities in the Cartesian adaptive solver, NASCART-GT. The objectives of the proposed study are:

(i) To create and simulate a non-equilibrium framework for chemically reacting flows using an object oriented framework for an adaptive Cartesian grid-based flow solver.

(ii) To develop effective coupling of chemical and thermal non-equilibrium computational capabilities that are associated with a two-temperature model.

(iii) To develop effective coupling of chemical and thermal non-equilibrium capabilities for a multi-vibrational, single translational temperature model.

(iv) To determine the range of validity of the implemented multi-temperature models for various dilution levels and study their effectiveness at different pressures.

(v) To investigate the change in shock structure resulting from the implementation and

coupling of the electron energy balance equation to the set of governing equations.

The following chapters will discuss the mathematical and numerical formulations followed by a discussion of the results.

CHAPTER 2
GOVERNING EQUATIONS

2.1 Introduction

The governing equations used in this work to simulate hypersonic reacting flows comprise of the Euler equations that account for chemical non-equilibrium, vibrationally excited molecules as well as weakly ionized plasmas. In addition to the basic equations including equations of state, the underlying assumptions in obtaining the form of equations presented are also summarized.

2.2 Assumptions

In this work, the governing equations were solved assuming continuum flow fields and inviscid conditions. For continuum flow fields the Knudsen number, which is the ratio of the mean free path to the characteristic length of the body, is less than one.

The chemical non-equilibrium aspect of the governing equations is dealt with by including conservation of mass equation for each species involved. For thermo-chemical non-equilibrium flows, the species' mass conservation equations were coupled to equations that accounted for conservation of vibrational energy and/or electron energy.

In particlar, thermal non-equilibrium resulted in equations that considered the flow-field to be represented by multiple temperatures. Calorically perfect gas simulations or chemical non-equilibrium flows required the need for a single temperature to define the flowfield. The difference in the representations stemmed from the use of perfect gas assumptions or real gas effects only. The usage of a two temperature model in this study refers to the representation of the translational and average vibrational energy by separate temperatures. The rotational mode is assumed to be in equilibrium with the translational mode and therefore is set to be equal to the translational temperature. The multi-vibrational model assumes each diatomic molecule in the gaseous mixture to be described by a unique vibrational

temperature based on the harmonic oscillator model. This assumption is reasonable for the flow fields considered in this study where that temperatures involved are fairly low, and exempts the need to consider anharmonicity in the vibrational states. While recent studies [39] based on collisional models have successfully developed rovibrational models based on non-Boltzmann energy distributions, their complexity renders them hard for incorporation in to a multi-temperature fomulation. Therefore, the present study does not assume that the rotational modes and vibrational modes are in equilibrium.

For weakly ionized flows, the multi-temperature formulation may be more appropriately characterized by multiple vibrational temperatures, and two separate translational temperatures for electrons and other constituent atoms/molecules in the mixture. To compute weakly ionized flows, the terms related to strong electro-magnetic field effects are neglected which is a reasonable assumption for the flows considered in the present study.

2.3 Mathematical Formulation

The time accurate simulations conducted in this study consider the unsteady form of Euler equations for conservation of species mass, momentum and energy. The mass conservation equation is given by:

$$\frac{\partial \rho_s}{\partial t} + \frac{\rho_s u_j}{\partial x_j} = -\frac{\partial \rho_s v_j}{\partial x_j} + \omega_s \tag{2.1}$$

The species momentum equation is given by:

$$\frac{\partial \rho u_i}{\partial t} + \frac{(\rho u_i u_j + p\delta_{ij})}{\partial x_j} = N_s e Z_s \hat{E}_i + P_{si} \tag{2.2}$$

The species energy conservation equation is given by:

$$\frac{\partial E_s}{\partial t} + \frac{\partial (E_s + p_s) u_{sj}}{\partial x_j} = N_s e Z_s \hat{E}_i u_{si} + Q_{si} \tag{2.3}$$

The mass source term, ω_s, is the rate of production of species s for reacting flows. P_s and Q_s represent the momentum and energy rates respectively. $\hat{E}_i$ represents the electric field in the i direction due to charge separation, and is activated only for weakly ionized hypersonic flows.

In addition to the above set of equations, the vibrational energy conservation equation for each diatomic species may be considered for multi-vibrational temperature formulations. These sets of equations are represented in the following form.

$$\frac{\partial E_{vs}}{\partial t} + \frac{\partial (E_{vs} u_j)}{\partial x_j} + \frac{\partial (E_{vs} v_j)}{\partial x_j} = Q_{vs} + \omega_s e_{vs} \tag{2.4}$$

The above formulation accounts for the addition and removal of vibrational energy due to chemical reactions taking place in the system. This does not allow for any preferential removal of vibrational energy due to dissociation.

Finally, the electron energy conservation equation is given by:

$$\frac{\partial E_e}{\partial t} + \frac{\partial ((E_e + p_e) u_j)}{\partial x_j} + \frac{\partial (E_e v_j)}{\partial x_j} = Q_{T-e} - \sum_{s=1}^{m} Q_{e-vs} + \omega_e e_e \tag{2.5}$$

2.3.1 Equations of State and Other Ancillary Relations

The total density and pressure as used in the above equations relate to the the species densities and pressures as follows:

$$\rho = \sum_{s=1}^{n} \rho_s \tag{2.6}$$

$$p = \sum_{s \neq e}^{n} \rho_s \frac{R}{M_s} T + p_e \tag{2.7}$$

where, the the electron pressure, p_e, is represented by

$$p_e = \rho_e \frac{R}{M_e} T_e \tag{2.8}$$

The total energy, E, is represented by the following individual contributions acting together:

$$E = \sum_{s \neq e}^{n} \rho_s c_{v_s} T + \frac{1}{2} \sum_{s \neq e}^{n} \rho_s u_i u_i + \sum_{s=1}^{m} E_{v_s} + E_e + \sum_{s \neq e}^{n} \rho_s h_s^o \tag{2.9}$$

In the equations represented above, the vibrational energy per particle is related to the vibrational energy per unit volume by the relation

$$E_{v_s} = \rho_s e_{v,s} = \rho_s e_{v,s} \frac{\hat{N}}{M_s} \tag{2.10}$$

The vibrational energy defined by the harmonic oscillator model is

$$E_{v_s} = \rho_s \frac{R}{M_s} \frac{\theta_{v_s}}{e^{\theta_{v_s}/T_{v_s}} - 1} \tag{2.11}$$

Through the above equation, the vibrational temperature of any species can be obtained. Similarly, the electron energy equation provides the electron temperature,

$$E_e = \rho_e c_{v_e} T_e + \frac{1}{2} \rho_e u_i u_i \tag{2.12}$$

Also, the electron pressure is assumed to be far more dominant than electron dynamic pressure. The resulting electric field [40] is denoted by

$$E_i \approx -\frac{1}{N_e e} \frac{\partial p_e}{\partial x_i} \tag{2.13}$$

and, finally, the enthalpy per unit mass is defined to be

$$h_s = c_{v_s} T + \frac{p_s}{\rho_s} + e_{v_s} + h_s^o \tag{2.14}$$

2.4 Energy Exchange Rate Equations

The various energy exchange models used in the governing equations are described below. The empirical models are assumed to be representative of the dominant energy exchange processes occuring in the class of weakly ionized flows considered. The translation-vibration energy exchange rate is descibed by the Landau-Teller form where only single quantum transitions are considered.

$$Q_{T-V_s} = \rho_s \frac{e_{v_s}^*(T) - e_{v_s}}{< \tau_{s_{L-T}} >} \tag{2.15}$$

The molar-averaged relaxation time given by Lee [41] is used.

$$< \tau_{s_{L-T}} >= \frac{\Sigma_{r,r\neq e} X_r}{\Sigma_{r,r\neq e} X_r / \tau_{sr_{L-T}}} \tag{2.16}$$

The inter-species relaxation time as developed by Millikan and White [42] is

$$\tau_{sr_{L-T}} = \frac{1}{p_{atm}} exp[A_{sr}(T^{-1/3} - 0.015\mu_{sr}^{1/4}) - 18.42], where \tag{2.17}$$

$$A_{sr} = 1.16 \times 10^{-3} \mu_{sr}^{1/2} \theta_{vs}^{4/3}, and \tag{2.18}$$

$$\mu_{sr} = M_s M_r / (M_s + M_r) \tag{2.19}$$

The overprediction of the collision cross-section is overcome by adding a limiting cross-section as suggested by Park [43], i.e.

$$\tau_{v_s} = < \tau_{s_{L-T}} > + \tau_{cs}, where \tag{2.20}$$

$$\tau_{cs} = \frac{1}{c_s \sigma_v N_s}, \tag{2.21}$$

$$c_s = \sqrt{\frac{8RT}{\pi M_s}}, and \tag{2.22}$$

$$\sigma_v = 10^{-21} (50,000/T)^2 \tag{2.23}$$

The vibration-vibration energy rate, as developed by Candler [40] from kinetic theory and experimental studies, is given as,

$$Q_{V-V_s} = Q_{V-V_{sr}} - Q_{V-V_{rs}} \tag{2.24}$$

The two terms on the right hand side of the above equation represent the energy exchange processes occuring in the forward and backward directions. The forward v-v exchange rate, when derived from first principles, results in

$$Q_{V-V_{sr}} = P_{sr} \sigma_{sr} \sqrt{\frac{8RT}{\pi \mu_{sr}}} \frac{\rho_s}{M_s} \hat{N} E_{v_r} \tag{2.25}$$

The probability of exchange, as can be deduced from the experimental work of Taylor et al. [44], was taken to be a constant value of 10^{-2}, and the collision cross-section was computed from the same work [44] using the relation, $\sigma_{sr} = d_s d_r$.

The translation-electron energy exchange rate was taken from Lee's formulation [41]. The exchange rate equation is,

$$Q_{T-e} = 3R\rho_e(T - T_e)\sqrt{\frac{8RT_e}{\pi M_e}}\sum_{r\neq e}\frac{\rho_r \hat{N}}{M_r^2}\sigma_{er} \tag{2.26}$$

where the collision cross-section involving ions can be represented as [41],

$$\sigma_{e,ions} = \frac{8\pi}{27}\frac{e^4}{k_B^2 T_e^2} ln\left[1 + \frac{9k_B^3 T_e^3}{4\pi N_e e^6}\right] \tag{2.27}$$

The unknown form of $\sigma_{e,neutrals}$ was assumed to be 10^{-20} m^2 [40].

Lee [45] showed that the coupling of electron energy with diatomic nitrogen for typical air composition is the only interaction of considerable magnitude. This exchange rate is represented as,

$$Q_{e-V,s} = \rho_e \frac{M_s}{M_e}\frac{e^*_{v,s}(T_e) - e_{v,s}}{\tau_{e,s}}, \quad s = N_2 \quad only \tag{2.28}$$

The relaxation parameter, $p_e\tau_{es}$, as derived by Lee [45] consisted of an integral of a set of master equations. Candler's curve fits [40] to the integrated system was used in the formulation here,

$$log(p_e\tau_{es}) = 7.50(logT_e)^2 - 57.0(logT_e) + 98.70, \qquad for \qquad T_e < 7000K \tag{2.29}$$

$$log(p_e\tau_{es}) = 2.36(logT_e)^2 - 17.9(logT_e) + 24.35, \qquad for \qquad T_e >= 7000K \tag{2.30}$$

2.5 Chemical Model

For the generic chemical reaction,

$$\sum_{i=1}^{N_s}\nu_i' X_i \rightleftharpoons \sum_{i=1}^{N_s}\nu_i'' X_i \tag{2.31}$$

the rate of production of species, s, is related to the rate of change of the concentration of the species X_i due to the forward and backward reactions taking place simultaneously. The following two reactions encapsulate this concept:

$$\omega_s = M_s \sum_{i=1}^{N_R} \frac{dX_i}{dt} \tag{2.32}$$

$$\frac{dX_i}{dt} = (\nu_i^{'} - \nu_i^{"}) \left\{ k_f \prod_N [X_i]^{\nu_i^{'}} - k_b \prod_N [X_i]^{\nu_i^{"}} \right\} \tag{2.33}$$

The forward and backward reaction rates, which are assumed to take place at a certain effective temperature depending upon the type of reaction involved, are computed as follows.

$$k_f(T_{eff_1}) = C_f T_{eff_1}^{\eta} exp(-E_f/kT_{eff_1}), and \tag{2.34}$$

$$k_b(T_{eff_2}) = \frac{k_f(T_{eff_1})}{K_{eq}(T)}, where, \tag{2.35}$$

$$k_{eq}(T) = exp(A_{k_{eq}}\Theta^5 + B_{k_{eq}}\Theta^4 + C_{k_{eq}}\Theta^3 + D_{k_{eq}}\Theta^2 + E_{k_{eq}}\Theta + F_{k_{eq}}) \tag{2.36}$$

$$\Theta = ln(10^4/T) \tag{2.37}$$

It should be noted here that the effective temperatures of the forward and backward temperatures are not necessarily the same for a given reaction. For instance, dissociation reactions involving heavy particles have a forward reaction rate that depends on the geometric average of the translational temperature of the impacting species and the vibrational temperature of the dissociating molecule [17]. However, the backward reaction rate depends upon the translating temperature of the impacting third body. The forward reaction rate for associative ionization reactions take a similar formulation as the dissociation reactions. However, the backward reaction is known to be dependent on the vibrational temperature of the positive ion. Such choices of the effective temperatures can greatly impact the solution; varied governing temperatures have led to wide variations in results obtained by different researchers.

CHAPTER 3
NUMERICAL METHODS

3.1 Introduction

This chapter outlines the form of the compressible Euler equations in Cartesian coordinates used to solve the multi-temperature problem involved in this work.

3.2 NASCART-GT

The code, NASCART-GT, uses an unstructured Cartesian grid, where a binary tree data structure is used to explicity state the grid connectivity. The main components of the binary tree adopted include :information about the geometry, the fluid, and connectivity such as pointers to parent or children cells [46]. The geometry-based adaptation process used in the code, that requires the information of neighboring nodes, involves the use of linked lists for easy updating of neighboring information at each time step. Grid generation is performed automatically through recursive refinement of the root cell in the computational domain. This removes the human in the loop that is unavoidable for the generation of structured grids. To ensure accurate capture of flow physics, the computational cells adjacent to the geometry must be refined to a sufficient level. This is achieved via adaptation of the cut cells. This refinement of the cell near the body is dependent on a user-defined length scale.

NASCART-GT is also designed to solve the flow structures using solution-based grid adaptation. Error indicators based on some pre-defined adaptation criteria help add more cells in regions of high gradients to more precisely capture the flow physics. The newly developed object-oriented code has the capability of solving Euler, Euler+Integral boundary layer, and Navier-Stokes equations. This present work incorporates thermo-chemical non-equilibrium and ionization computing capabilities for Euler equations.

3.3 Governing Equations in Vector Form

The governing equations for weakly ionized continuum hypersonic flows have been largely solved on structured grids using fully implicit methods and Roe's scheme [2, 4, 31]. In this study, the fluid equations have been solved explicitly while the rate equations involving chemistry are solved in an implicit manner. The Roe's flux differencing scheme in its original form proved to be dissipative for hypersonic flow simulations and led to shock instability such as the carbuncle phenomenon. Only recently [47], reduction of the rate at which pressure oscillation feeds the density field have been proposed for the Rho's scheme. Another scheme that has been shown to be less dissipative and more stable for hypersonic flows is the AUSMPW+ scheme [48]. This is the scheme that is being used in the present study. The conservation equations in two dimensions and vector form can be represented as:

$$\frac{\partial \vec{U}}{\partial t} + \frac{\partial \vec{F}}{\partial x} + \frac{\partial \vec{G}}{\partial y} = \vec{S} \tag{3.1}$$

The vectors in the above equation are,

$$\vec{\boldsymbol{U}} = \begin{pmatrix} \rho \\ \rho u \\ \rho v \\ \rho E_t \\ \rho_1 \\ . \\ \rho_i \\ . \\ \rho_{N_s} \\ \rho_1 e_{v_1} \\ . \\ \rho_s e_{v_s} \\ . \\ \rho_{N_{v,s}} e_{v_{N_{v,s}}} \\ \rho_e e_e \end{pmatrix}, \quad \vec{\boldsymbol{F}} = \begin{pmatrix} \rho u \\ \rho u^2 + p \\ \rho uv \\ \rho u(E_t + p) \\ \rho_1 u \\ . \\ \rho_i u \\ . \\ \rho_{N_s} u \\ \rho_1 e_{v_1} u \\ . \\ \rho_s e_{v_s} u \\ . \\ \rho_{N_{v,s}} e_{v_{N_{v,s}}} u \\ \rho_e e_e u \end{pmatrix}, \quad \vec{\boldsymbol{G}} = \begin{pmatrix} \rho v \\ \rho uv \\ \rho v^2 + p \\ \rho v(E_t + p) \\ \rho_1 v \\ . \\ \rho_i v \\ . \\ \rho_{N_s} v \\ \rho_1 e_{v_1} v \\ . \\ \rho_s e_{v_s} v \\ . \\ \rho_{N_{v,s}} e_{v_{N_{v,s}}} v \\ \rho_e e_e v \end{pmatrix}, \quad \vec{\boldsymbol{S}} = \begin{pmatrix} 0 \\ 0 \\ 0 \\ 0 \\ \dot{\omega_1} \\ . \\ \dot{\omega_i} \\ . \\ \dot{\omega_{N_s}} \\ \dot{\omega_{v_1}} \\ . \\ \dot{\omega_{v_s}} \\ . \\ \dot{\omega_{v_{N_{v,s}}}} \\ \dot{\omega_e} \end{pmatrix} \tag{3.2}$$

3.4 AUSMPW+ Scheme for Weakly Ionized Flows

Considering the flux in one direction only, the the inviscid flux in the x-direction, according to the AUSMPW+ scheme [48] is:

$$F_{\frac{1}{2}} = \bar{M}_L^+ c_{\frac{1}{2}} \boldsymbol{\Phi}_L + \bar{M}_R^- c_{\frac{1}{2}} \boldsymbol{\Phi}_R + (P_L^+|_\alpha[\boldsymbol{P}_L] + P_R^+|_\alpha[\boldsymbol{P}_R]) \tag{3.3}$$

The Mach number at the cell interface is given to be

$$m_{\frac{1}{2}} = \bar{M}_L^+ + \bar{M}_R^- \tag{3.4}$$

The mathematical relations that define $\bar{M}_L^+$ and $\bar{M}_R^-$ depend upon the cell interface-Mach number. When $m_{\frac{1}{2}} \geq 0$,

$$\bar{M}_L^+ = M_L^+ + M_R^-[(1-\omega_p)(1+f_R) - f_L] \tag{3.5}$$

$$\bar{M}_R^- = M_R^-\omega_p(1+f_R) \tag{3.6}$$

When $m_{\frac{1}{2}} \leq 0$,

$$\bar{M}_L^+ = M_L^+\omega_p(1+f_L) \tag{3.7}$$

$$\bar{M}_R^- = M_R^- + M_L^+[(1-\omega_p)(1+f_L) - f_R] \tag{3.8}$$

where,

$$\omega_p(p_L, p_R) = 1 - min\left(\frac{p_L}{p_R}, \frac{p_R}{p_L}\right)^3 \tag{3.9}$$

and,

$$f_{L,R} = \left(\frac{p_{L,R}}{p_s} - 1\right) min\left[1, \frac{min(p_{1,L}, p_{1,R}, p_{2,L}, p_{2,R})}{min(p_L, p_R)}\right]^2, p_s \neq 0 \tag{3.10}$$

$$f_{L,R} = 0, \qquad p_s = 0 \tag{3.11}$$

Furthermore,

$$p_s = P_L^+ p_L + P_R^- p_R \tag{3.12}$$

The modifications for weakly ionized flows get expressed in the $\boldsymbol{\Phi}$ and $\boldsymbol{P}$ vectors. These vectors, when accounting for multiple vibrational temperatures and the electron energy conservation equation take on the form:

$$\boldsymbol{\Phi} = [\rho, \rho u, \rho v, \rho w, \rho h, \rho_1, ..., \rho_{N_s}, \rho_1 e_{v_1}, ..., \rho_{N_s} e_{v_{N_{v,s}}}, \rho_e e_e]^T \tag{3.13}$$

$$\boldsymbol{P} = [0, p, 0, 0, 0, 0, ..., 0, 0, ..., 0, p_e]^T \tag{3.14}$$

The remainder of the formulation remains unchanged for the definition of quantities such as the pressure splitting function, the critical speed of sound at the cell interface, and the average sensible total enthalpy for chemically reacting flows. Further details of the scheme

can be found in the original work by Kim et al. [48].

3.5 Point Implicit Scheme

For reasonable accuracy of computations, a second order explicit predictor-corrector scheme was used thoroughout this work. However, the chemical source terms were solved using a point-implicit method which had been previously incorporated in NASCART-GT [49]. For each cell, the conservation equations take the following vector form:

$$\frac{\partial[\vec{U}]}{\partial t}V + \vec{R}(\vec{U^n}) = [\vec{S}]^{n+1}V \tag{3.15}$$

where, $\vec{R}$ is the sum total of the flux terms, and V is the cell volume. The Taylor series expansion of the species production term gives

$$[\vec{S}]^{n+1} \approx [\vec{S}]^n + \frac{\partial[\vec{S}]^n}{\partial[\vec{U}]^n}\frac{d[\vec{U}]}{dt}\Delta t \tag{3.16}$$

The final integration scheme, after LU decomposition, results in the following form:

$$\frac{d[\vec{U}]}{dt}V = \left\{\mathbf{I} - \Delta t\frac{\partial[\vec{S}]^n}{\partial[\vec{U}]^n}\right\}^{-1}\left\{[\vec{S}]^nV - \vec{R}(\vec{U^n})\right\} \tag{3.17}$$

3.6 Calculation of temperatures

An initial guess value for the translational temperature is used to obtain the enthalpy and specific heat at constant pressure from the thermodynamic curve fits. Through Newton's iterative method, the final value of the translational temperature is obtained. For this root finding technique, the convergence criterion was based on a relative error of 10^{-6} in temperature estimates. The general form of the equation to estimate temperature for the highest fidelity non-equilibrium model implemented in this work can be represented in the following form:

$$T_{new} = T_{old} + \frac{\Delta H_{mix}(T_{old}, \vec{T_{v,s}}, \vec{Y_s}, T_{el})}{\Delta C_{p,mix}(T_{old}, \vec{T_{v,s}}, \vec{Y_s}, T_{el})} \tag{3.18}$$

The vibrational temperature of the gas mixture/ a particular gas species is obtained from the updated relevant vibrational energy. Sufficient checks corresponding to the freestream conditions are implemented in the solver in order to produce physically meaningful vibrational temperatures. In particular, for multi-vibrational temperature model simulations, very small trace amounts ($\mathcal{O}(10^{-12})$ % or lesser by volume) of minor diatomic species are introduced in the freestream to prevent undefined vibrational temperatures in the computation. Similarly, the electron temperature is calculated from the electron energy in the updated state vector. The enthalpy calculation takes in to account coupling between the various energy modes. For all the temperature calculations, a lower clipping temperature of 100 K was set in the code.

The following sections describe the results obtained upon implementing the above set of governing equations and using the AUSMPW+ scheme.

CHAPTER 4
NON-EQUILIBRIUM RATE RESULTS

4.1 Introduction

The classical Landau-Teller theory is used to describe the vibrational-translational energy exchange in diatomic gases with the resulting mean vibrational energy relaxation equation widely used in hypersonic flow simulations till date. This Landau-Teller equation, in the macroscopic form and as described previously, is represented by the following equation:

$$\frac{dE_v(T)}{dt} = \frac{E_v(T) - E_v^{eq}}{\tau_{vib}} \tag{4.1}$$

The performance of this equation is typically studied by computing the relaxation time and/or temperature dependence of the relaxation rate for diatomic gases in a heat bath. While several studies in the past have well established the inverse temperature dependence of thermal relaxation times of N_2 [50] and H_2 [51], as well as other recent studies have focused on O_2 relaxation times [20], the studies pertaining to the Landau-Teller equation have been limited to the following assumptions :

(i) The dilution effects in a heat bath are limited to 5% of harmonic oscillators immersed in a constant temperature bath

(ii) The typical models considered have been limited to pressures of 1 atm

This chapter presents a study that examines the various chemical and multi-temperature thermo-chemical non-equilibrium models developed in the in-house C++ code. Due to the bounds placed on typical non-equilibrium heat baths, there is insufficient study of the behavior of the commonly used Landau Teller equation with harmonic oscillators in a concentration greater that 5% by volume.

4.2 Previous Studies on Heat Baths

In this section, some of the previous heat bath studies are highlighted. Tietelbaum [52] solved the steady state master equation to obtain the collision induced dissociation rate constants for hydrides diluted in Ar. At high temperatures, dissociation rates are determined by energy transfer processes. Their results which included the Landau-Teller energy formalism showed an explicit dependence on the oscillator energy, $mh\nu$. Landrum et al. [53] investigated the nonequilibrium vibrational relaxation of N_2 under isothermal and isochoric conditions. They found that the recombination rate for a heating bath is a function of the translational temperature and not the vibrational energy distribution. Gonzalez et al. [54] used the master equation to study shock heated N_2 in dilute Ar. They found that the approximated model near equilibrium replicated Landau-Teller results well at the start of their simulations. They found a two-step relaxation process for the average vibrational energy using master equations, which was not captured by their linearized model. Between 1000 and 3600 K, Andrienko et al. [55] were able to replicate Landau Teller relaxation times for an O_2-O system. However, solution to the master equations resulted in significantly different temperature dependence compared to the Millikan-White equation.

Boyd et al. [56] considered a heat bath with initial translational and vibrational temperature modes set to 10000 K and 1000 K respectively. The equilibration of such a heat bath initialized to a Boltzmann distribution was studied using CFD and DSMC models of varying levels of fidelity. In congruence to the previous studies [54], [53] where final Boltzmann distributions of constituent vibrational energies are to be expected, the same was verified through computations using the Landau Teller equation. In addition, the commonly observed bi-modal vibrational energy distributions that result from invoking a Larsen-Borgnakke model [57] in the DSMC framework were also verified. Several studies since the 1980s have experimentally and numerically verified the temperature range of validity for diatomic molecules. Furthermore, master equation formulations have well established temperature regimes where a Landau Teller approach does not well encapsulate the non-equilibrium states. Nonetheless, the Landau Teller equation that utilizes a Millikan-White relaxation time correlation is the single most widely used method to obtain quick

estimates of translation-vibration energy exchanges between diatomic as well as polyatomic molecules. In light of these previous studies, the investigations described in this chapter serve to answer the following questions:

(i) How do thermo-chemical non-equilibrium relaxation rates vary from thermal relaxation rates?

(ii) What are the effects of including less dilution of harmonic oscillators on the non-equilibrium characteristics of the gas system?

(iii) How does time to reach equilibrium scale with reduced initial pressure?

4.3 Thermo-Chemical Relaxation Rates: Two-Temperature Model

The hypersonics community has widely used the findings of Millikan and White experiments and the Landau Teller equation to characterize the translation-vibration energy exchange for flows such as those typically encountered during re-entry. As described above, N_2 and NO are the gases for which relaxation rates are studied [55] due to their importance in combustion and hypersonic re-entry problems. More recently, statistical-based studies such as those involving potential energy surfaces (PESs) have focused on quantifying rovibrational dissociation and relaxation of diatomic oxygen with molecular and atomic nitrogen and oxygen. The thermalization of these molecules at lower speeds has resulted in the community looking more closely at their associated rates using zero dimensional heat bath cases.

In this section, the results of non-equilibrium relaxation rates primarily for the dissociation of diatomic oxygen are studied under a variety of conditions. The zero-dimensional heat bath numerical simulations serve to validate the flow solver in addition to studying their range of validities. The first test case is one of thermal non-equilibrium of diatomic nitrogen with activated translation and vibration modes. This test case has been used by previous researchers [56] for the purposes of code validation. The heat bath is initiated with the translational mode set at 10000 K and the vibrational mode set to 1000 K. Upon using the Landau-Teller based T-V relaxation rate equation, it was observed that the rates matched (see figure 4.1) those recorded by Boyd et al. in their study of DSMC and CFD relaxation rates. The multi-temperature modeling approach used here is the two temperature model as described in Chapter 2. The effective temperature of $\sqrt{TT_v}$ was used in these heat bath simulations, and the thermalization process included N_2-N_2 as well as N_2-N collisions. In addition, a direct time step of 1 nanosecond was used to obtain the non-equilibrium results.

Following these results, it was of interest to investigate the thermo-chemical dissociation and relaxation rates for systems of gases involving diatomic O_2. This reaction was taken from Park's 1993 air reaction thermo-chemistry model, involving the dissociation of molecular oxygen by inert diatomic nitrogen. Initial results of a bimolecular collision in an O_2-N_2 gas system revealed that there are two distinct regions of equilibration, an initial attain-

ment of thermal equilibrium followed by chemical equilibrium. Following the attainment of thermal equilibrium, the gas cools down while reactions drive the system to equilibrium. Consequently, thermo-chemical equilibrium times extend to nearly 10 times the thermal counterparts. The initial concentrations by volume for diatomic oxygen and nitrogen was 10% and 90% respectively. Most studies in literature regarding heat bath simulations focus on a dilution of about 5% of the relaxing gas, resulting in thermalization to be the dominating process leading to equilibrium in these gases. Increasing the initial concentration of diatomic oxygen in uniform steps resulted in the trends shown in figure 4.3. The increase in mole fraction of diatomic oxygen from 0.1 to 0.2 resulted in a large variation in equilibrium times and final equilibrium temperature. However, subsequent increases in mole fractions of the dissociating and relaxing gas resulted in smaller variations, with initial dilutions >= 0.5 resulting in indiscernible variations in final equilibrium temperatures and times. However, the intermediate thermalization process indeed shows variations across the entire dilution range of 0.1-0.9 considered in this study. A cyclical variation of the thermal equilibrium point is observed with increasing dilution levels. The final time to reach equilibrium does not vary much for initial O_2 mole fractions greater than 0.2.

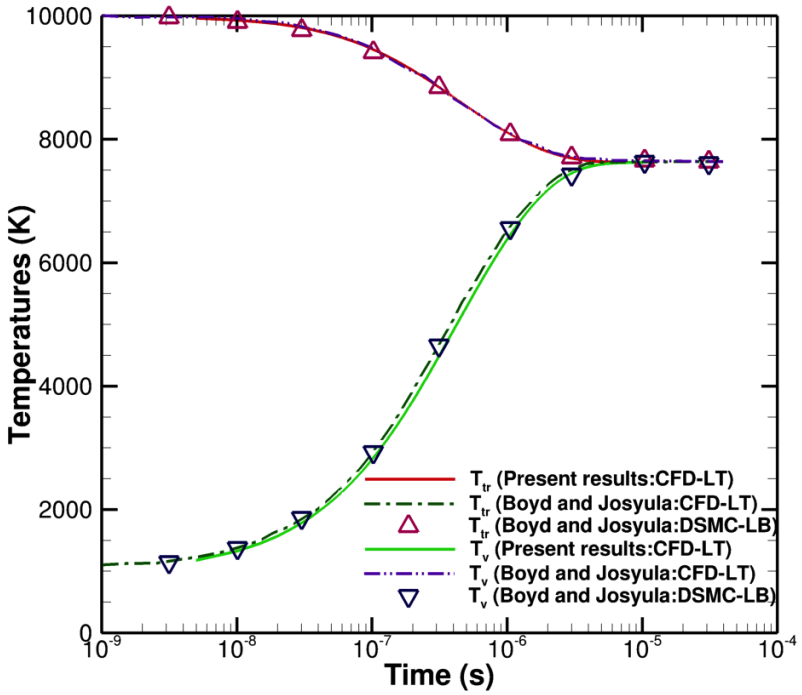

FIGURE 4.1. Validation of the present code developed, NASCART-GT, with results obtained by Boyd et al.

4.3.1 Universal transition phase

The presence of the distinct variations between 0.1 and 0.2 mole fractions of dissociating O_2 warrants further investigation of the underlying phenomena in this region. At the mole fractions of 0.1 and 0.2, it can be concluded that the gas is largely in thermal non-equilibrium only (Figure 4.7). Upon varying the concentration in steps of 0.01, it was seen that a largely linear variation in equilibrium temperature and time was obtained. Furthermore, the thermalization process also exhibited a monotonic variation in this range of mole fractions. Thus, an initial dilution level of the dissociating molecule greater than 0.2 marks the start of predominant chemical non-equilibrium effects.

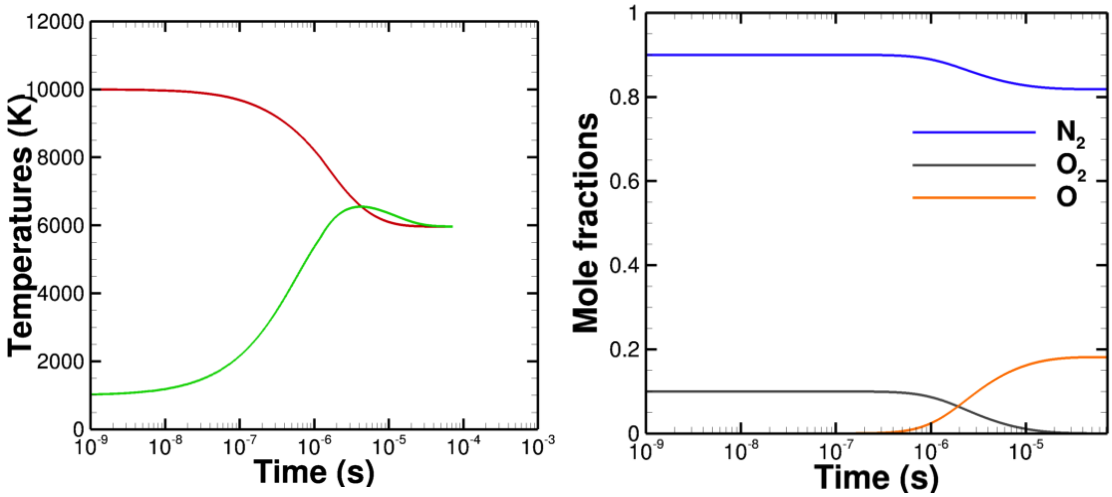

(A) Translational and vibrational temperatures obtained for a two temperature model

(B) Mole fractions of the various species in the gas mixture

FIGURE 4.2. Two temperature heat bath results for an initial mole fraction of O_2 of 0.1

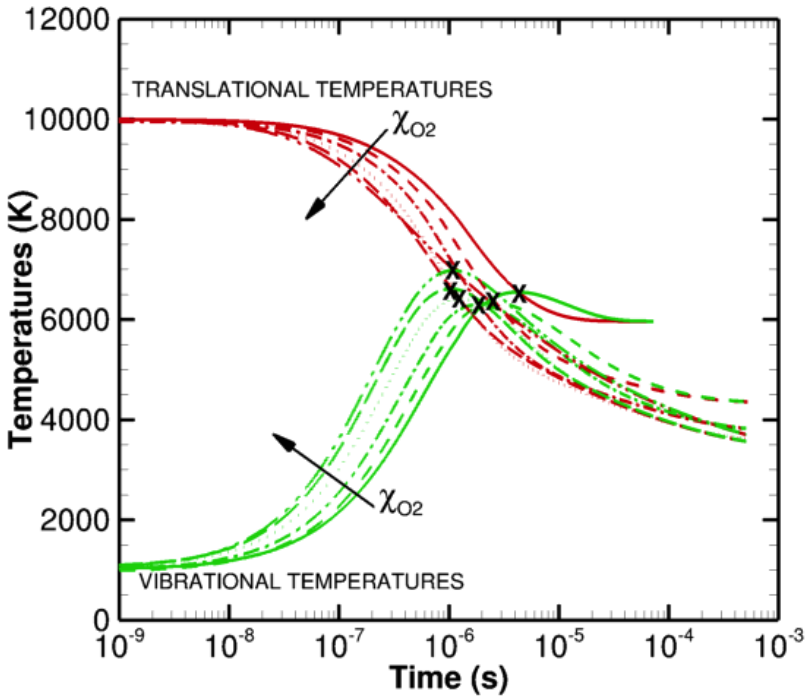

FIGURE 4.3. Two temperature model temperature results for varying initial mole fractions of an O_2-N_2 system. O_2 is the dissociating molecule while N_2 is merely involved in energy transfer.

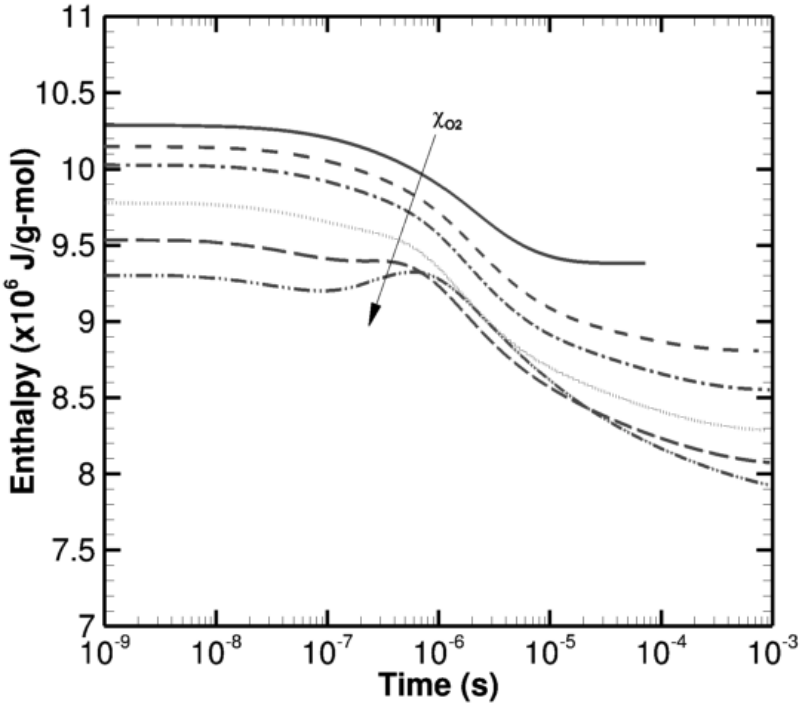

FIGURE 4.4. Two temperature model enthalpy results for varying initial mole fractions of an O_2-N_2 system

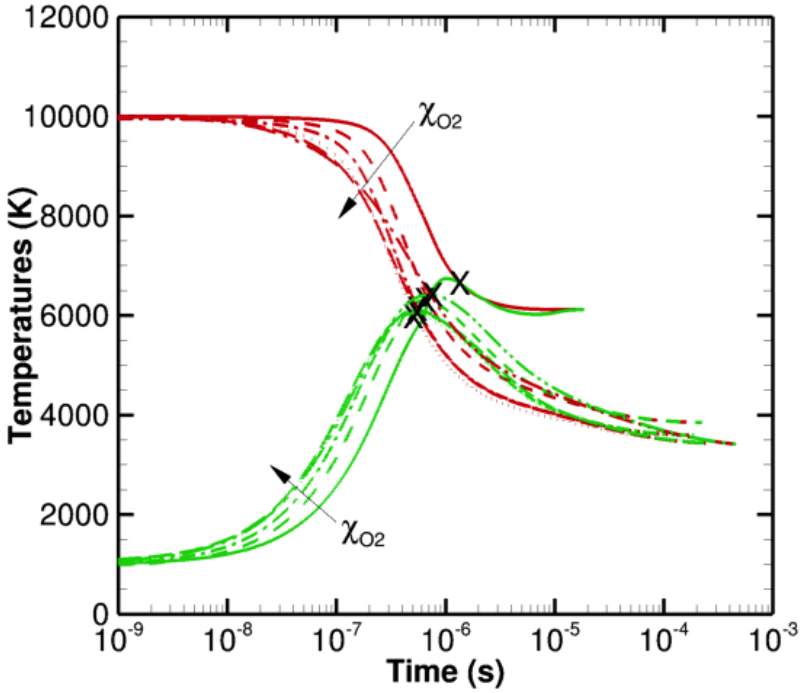

FIGURE 4.5. Two temperature model temperature results for varying initial mole fractions of an O_2-N system. O_2 is the dissociating molecule while N is merely involved in energy transfer.

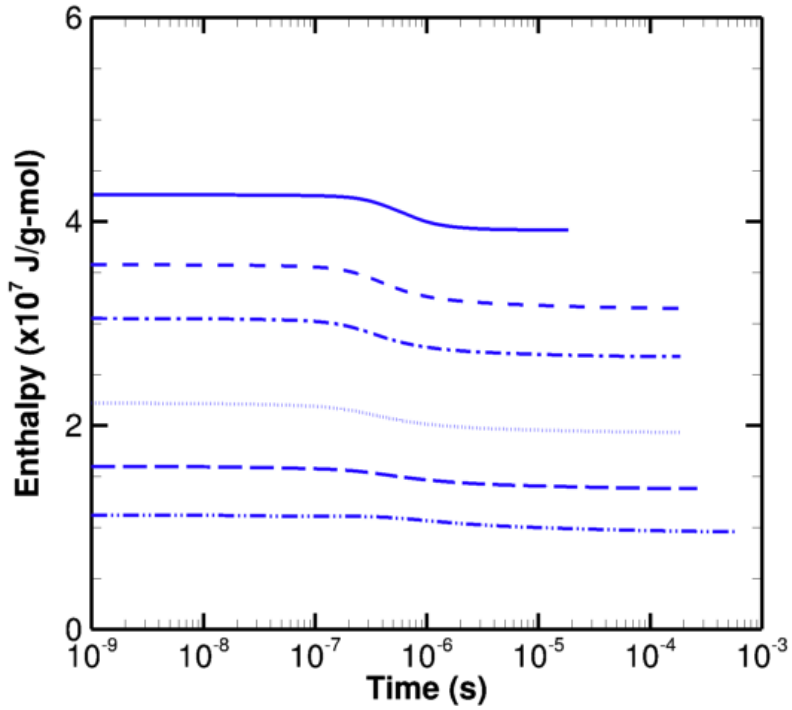

FIGURE 4.6. Two temperature model enthalpy results for varying initial mole fractions of an O_2-N system

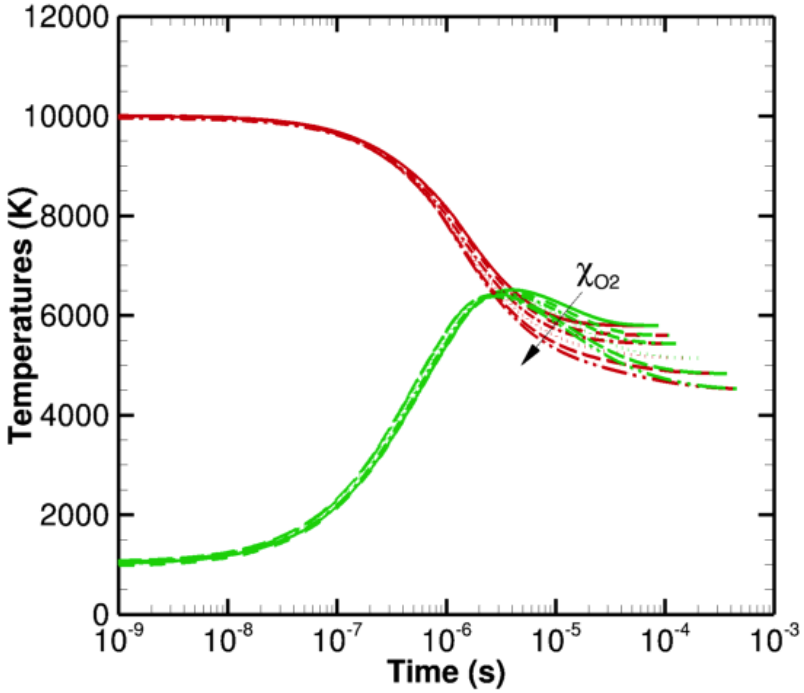

FIGURE 4.7. Two temperature model results for initial mole fractions of an O_2-N_2 system in the range of 0.1 and 0.2. O_2 is the dissociating molecule while N_2 is merely involved in energy transfer.

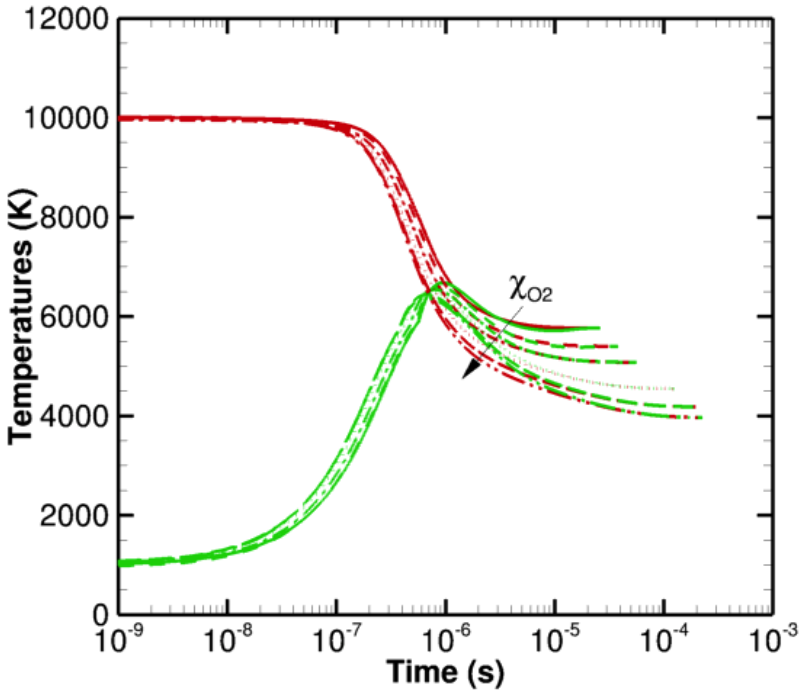

FIGURE 4.8. Two temperature model results for initial mole fractions of an O_2-N system in the range of 0.1 and 0.2. O_2 is the dissociating molecule while N is merely involved in energy transfer.

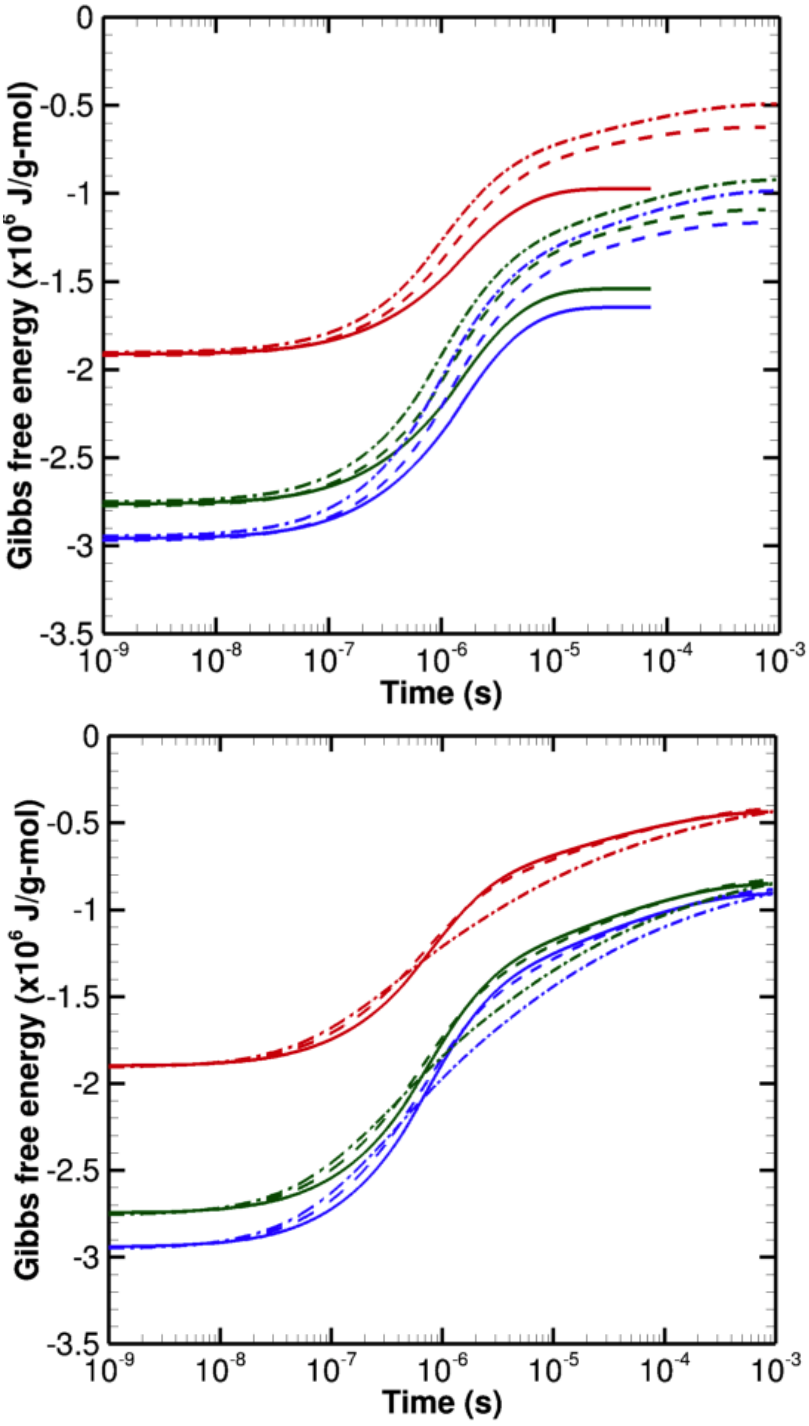

FIGURE 4.9. Time accurate Gibb's free energy results for an O_2-N_2 system at 1 atm: Initial mole fraction of O_2 of 0.1, 0.2, 0.3 (above) and 0.5, 0.7, 0.9 (below): —— 0.1 (above) and 0.5 (below); - - - - 0.2 (above) and 0.7 (below); —·—· 0.3 (above) and 0.9 (below) (■: O; ■: O_2 ; ■: N_2)

4.3.2 Modeling Effects: Non-Preferential models

In a preferential model it is assumed that molecules are created and destroyed at high energy levels while in a non-preferential model, it is assumed that these processes occur at the average vibrational energy of the molecules. Many studies in the past [58] have reported the variations in results obtained by using non-preferential as well as preferential models of Marrone-Treanor [8], Knab [59] and Macharet [60] models. In order to study the effects of using different forms of non-preferential modeling, one where the governing temperature of each reaction was based on the translational temperature alone was compared to the non-preferential $\sqrt{TT_v}$ model. It was seen that the translational temperature-based model resulted in a variation in the translational temperature at the very start of the simulation i.e. within a nanosecond. The initial rise in vibrational temperatures is similar for both the models. However, greater deviations between the two models are observed at initial O_2 mole fractions greater than 0.5. The reaction rates based on translational temperature alone therefore have a direct impact on the macroscopic translational temperatures in the transition to equilibrium for all dilutions studied. The temperature plots indicate that the final equilibrium temperature and time to equilibrium remains unaltered due to the choice between the two non-preferential models at any given initial dilution of O_2 (figure 4.10).

A study of the mole fractions indicate that the reaction rates are altered at the very start of the simulation with the transition between thermal equilibrium and chemical equilibrium being a gradual process. This transition is characterized by a marked change in the rate of reaction for the $\sqrt{TT_v}$ model. This rate of transition is consistent across the graphs depicting the transient temperatures and mole fractions. However, the mole fractions for the both non-preferential models at any given initial dilution level indicate that any variations in intermediate chemistry occur at a distinct time of less than one microsecond (figure 4.11). This key value in time is clouded by the overshoot of vibrational temperature with translation temperature while observing the temperature variations resulting from the $\sqrt{TT_v}$ model. Moreover, this section of the study proves that any such overshoot for the the translational temperature-based model is maintained a constant for all initial mole fraction levels chosen. However, the overshoot for the $\sqrt{TT_v}$ model is a variable across the chosen

dilution levels. Thereby, this could indeed be artifact of the empirical nature of the $\sqrt{TT_v}$ model as indicated in literature.

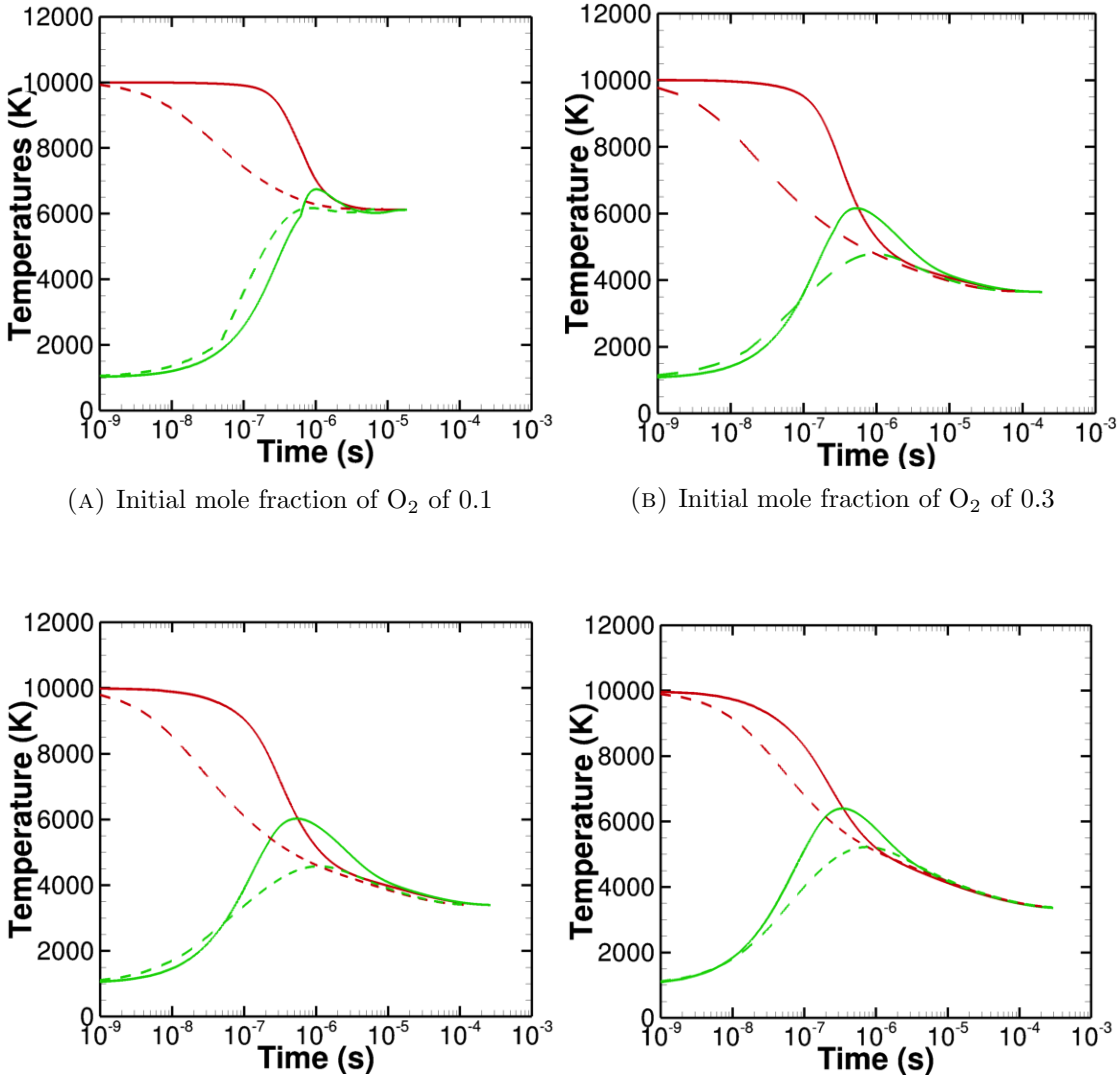

(A) Initial mole fraction of O_2 of 0.1

(B) Initial mole fraction of O_2 of 0.3

(C) Initial mole fraction of O_2 of 0.5

(D) Initial mole fraction of O_2 of 0.7

FIGURE 4.10. Variation in non-equilibrium temperatures between T-based and $\sqrt{TT_v}$ non-preferential models: —— Non-preferential $\sqrt{TT_v}$ model; - - - - Non-preferential translation temperature-based model; (■: Translational temperature; ■: Vibrational temperature)

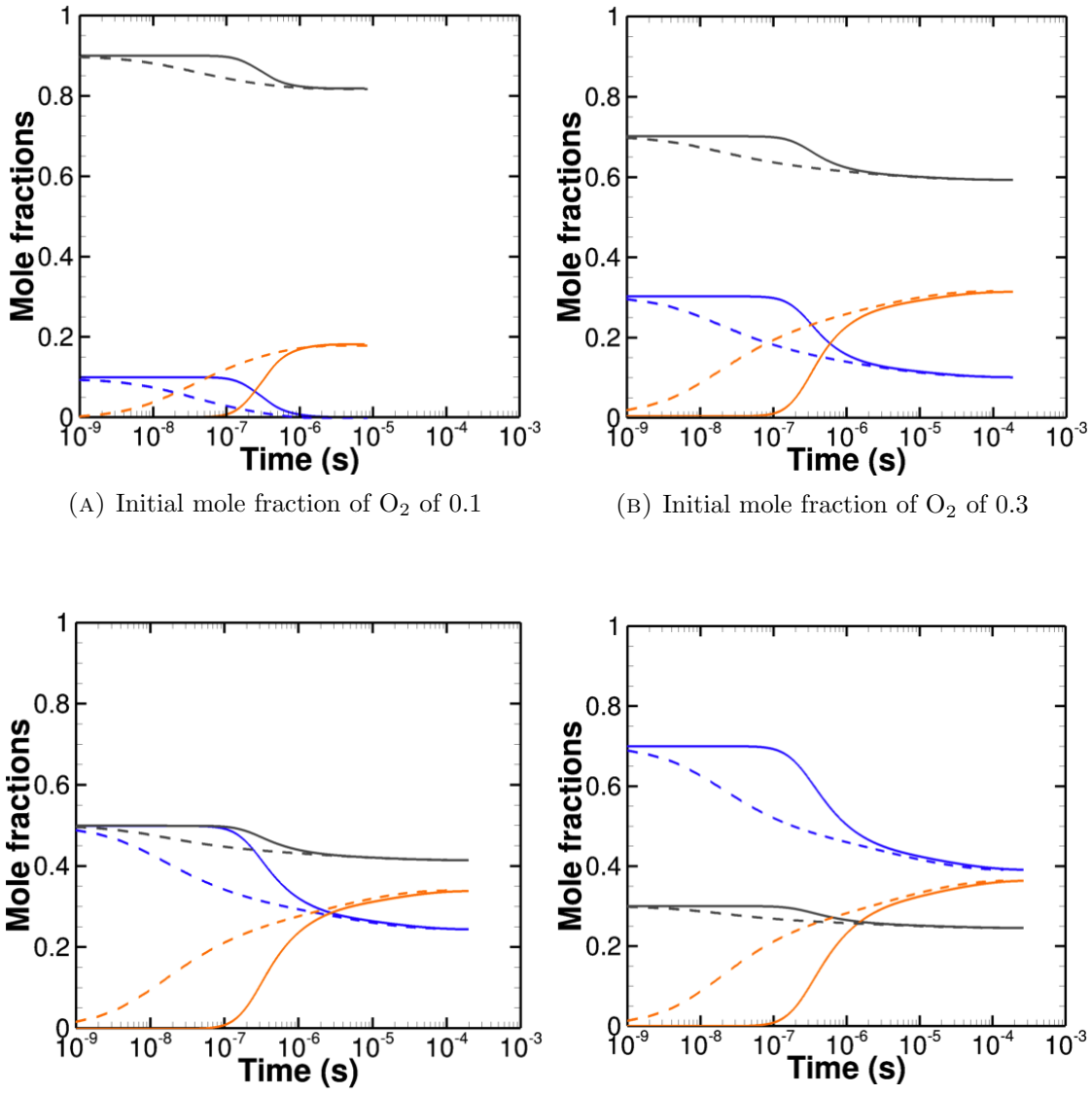

(A) Initial mole fraction of O_2 of 0.1

(B) Initial mole fraction of O_2 of 0.3

(C) Initial mole fraction of O_2 of 0.5

(D) Initial mole fraction of O_2 of 0.7

FIGURE 4.11. Variation in non-equilibrium mass fractions between two non-preferential models: —— Non-preferential $\sqrt{TT_v}$ model; -- -- Non-preferential translation temperature-based model; (■: N ;■: O_2 ; ■: O)

4.3.3 Molecular/Atomic Effects

The Millikan-White correlations account for atomic-molecular collisions in addition to bi-molecular collisions. The results shown in the previous section for the O_2-N_2 system involve a complex thermal non-equilibrium process coupled with dissociation of O_2 due to the collision of inert N_2. The non-linearity effects seen due to thermal non-equilibrium in an O_2-N_2 system are due to a complex mixing process that includes collisions between like and dislike molecules. The collisions in the mixing process further include molecule-atom and atom-atom collisions. In order to separate out the molecule-molecule collisions from ones that include the atom-molecule pair, additional sets of tests were undertaken that studied the reaction O_2+N=2O+N under thermo-chemical non-equilibrium.

The inclusion of O_2-N, as can be seen in figure 4.5, results in similar non-equilibrium characteristics for an initial mole fraction of O_2 of 0.1. The jump in final equilibrium temperature and time between initial mole fractions of 0.1 and 0.2 widen in the O_2-N system in comparison to the O_2-N_2 system. However, it is interesting to note that beyond a choice of an initial mole fraction of 0.3, the point of overshoot of vibrational temperature coalesces approximately to a similar point in time. It can be concluded from these results that thermal non-equilibrium exhibits greater non-linearity when dissimilar molecular collisions are involved. There is a reduction in time to attain thermal equilibrium by about 67% in comparision to the O_2-N_2 system. The final equilibrium times indicate an 80% reduction upon choosing an inert atom in the dissociation process. The final equilibrium energy of the system in this case remains unaltered in the mole fraction range of 0.2-0.9. The molar enthalpies show a simple linear variation throughout the initial mole fraction range of 0.1-0.9. The mixture molar enthalpy in the system is more than an order of magnitude higher than that involving inert N_2. Additionally, the variation of molar enthalpy with time is nearly constant for the O_2-N system. However, the enthalpy shows a large non-linear variation for the O_2-N_2 system with a non-monotonic variation seen for the initial mole fraction of 0.9 (figure 4.4).

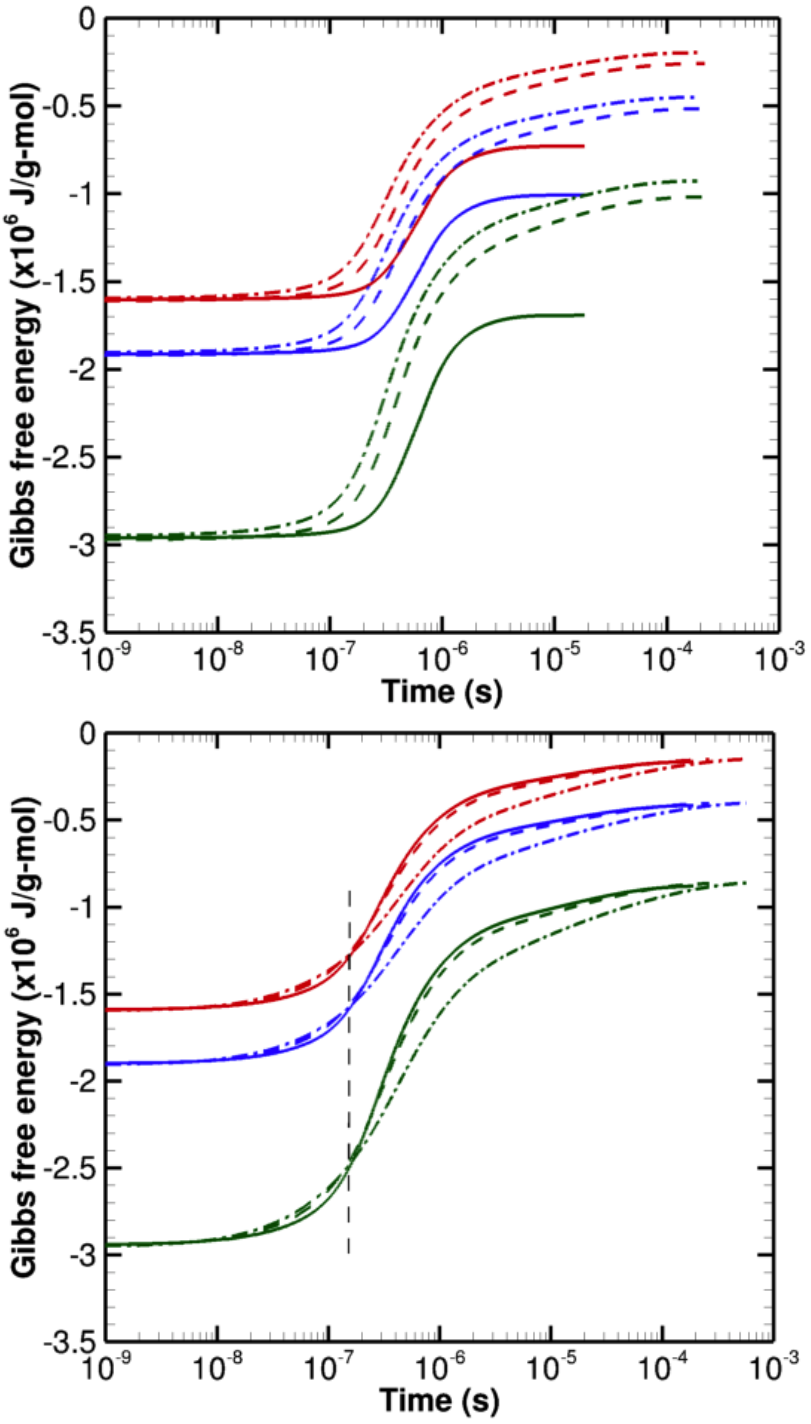

FIGURE 4.12. Time accurate Gibb's free energy results for an O_2-N system at 1 atm using a $\sqrt{TT_v}$ model: Initial mole fraction of O_2 of 0.1, 0.2, 0.3 (above) and 0.5, 0.7, 0.9 (below): —— 0.1 (above) and 0.5 (below); - - - - 0.2 (above) and 0.7 (below); —·—· 0.3 (above) and 0.9 (below) (■: O; ■: N ; ■: O_2)

4.3.4 Pressure Effects

The O_2-N system described above was initially assumed to be at atmospheric pressure. In order to investigate the impact of greater initial degree of non-equilibrium, the total pressure of the system was altered to 0.1 atmospheres at the start of the simulations. Figures 4.13, 4.14 and 4.15 show the effect of reducing the initial pressure of the system by an order of magnitude compared to the results for an O_2-N system described previously. The non-equilibrium as well as the time to attain equilibrium translates by an order of magnitude but in the opposite direction for the initial O_2 mole fraction of 0.1. However, for lower dilution values, a reduction in initial pressure delays the attainment of final equilibirum by nearly two orders of magnitude. These tabular values are represented below:

TABLE 4.1. Effects of initial pressure in an O_2-N heat bath system

Initial pressure (atm)	Time to equilibrium for initial O_2 mole fraction = 0.1 (s)	Time to equilibrium for initial O_2 mole fraction > 0.1 (s)	Time at 'cross-over' in Gibbs free energy (s)
1	10^{-5}	$\sim 10^{-4}$	10^{-7}
0.1	10^{-4}	$\sim 10^{-2}$	10^{-6}

The non-equilibrium mole fractions also represent this shift in time from the point of initiation of dissociation to final equilibrium upon reducing the system initial pressure. The longer times associated with the lower pressure result from the lower translational energy associated with the system particles. An increased probability of bi-molecular collisions (such as when initial mole fraction of O_2 > 0.1) can enhance the equilibrium times by nearly two orders of magnitude at 0.1 atm. Therefore, increased initial concentrations of the reacting (/dissociating) molecules bolsters the non-equilibirum effects induced by a reduced system pressure.

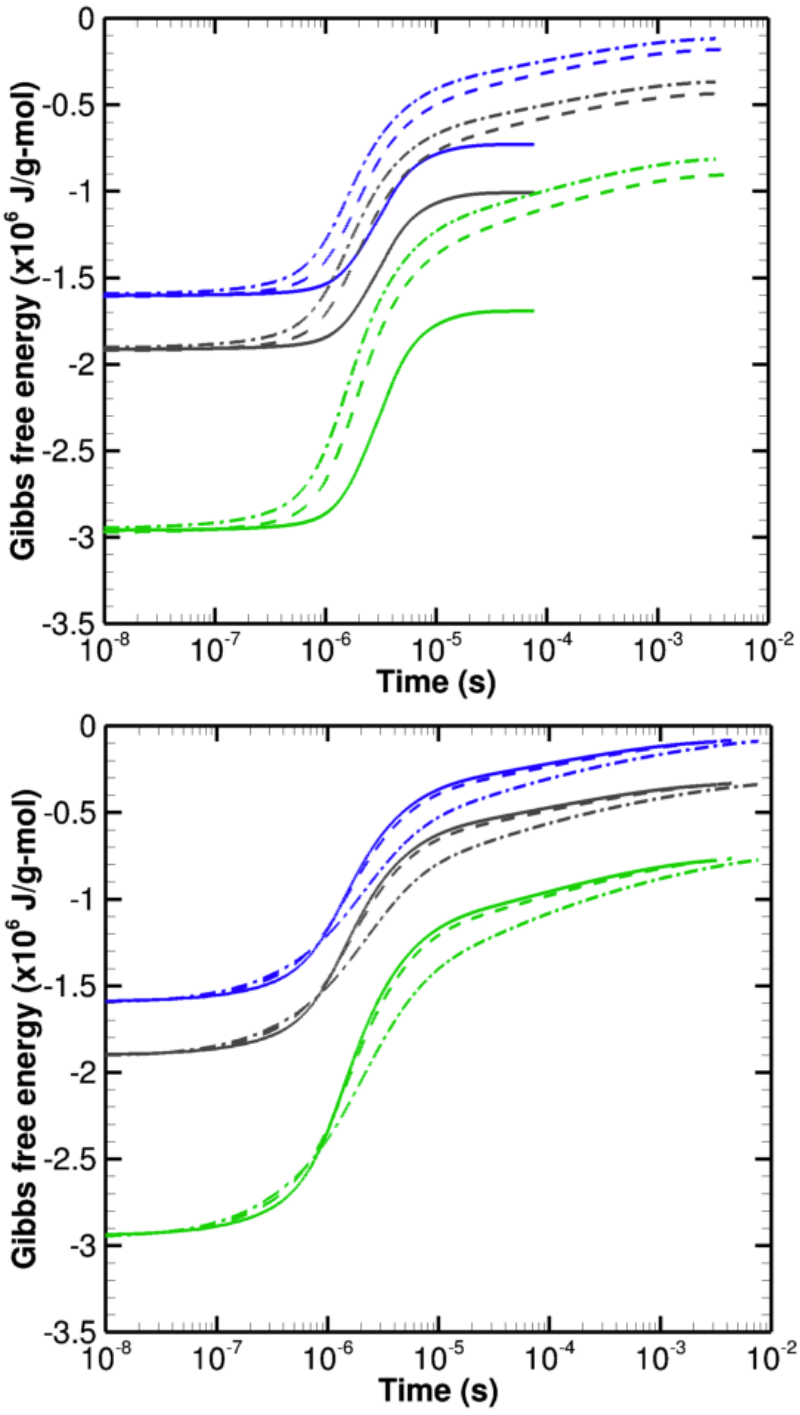

FIGURE 4.13. Time accurate Gibb's free energy results for an O_2-N system at 0.1 atm using a $\sqrt{TT_v}$ model: Initial mole fraction of O_2 of 0.1, 0.2, 0.3 (above) and 0.5, 0.7, 0.9 (below): —— 0.1 (above) and 0.5 (below); - - - - 0.2 (above) and 0.7 (below); —·—· 0.3 (above) and 0.9 (below) (■: O; ■: N ; ■: O_2)

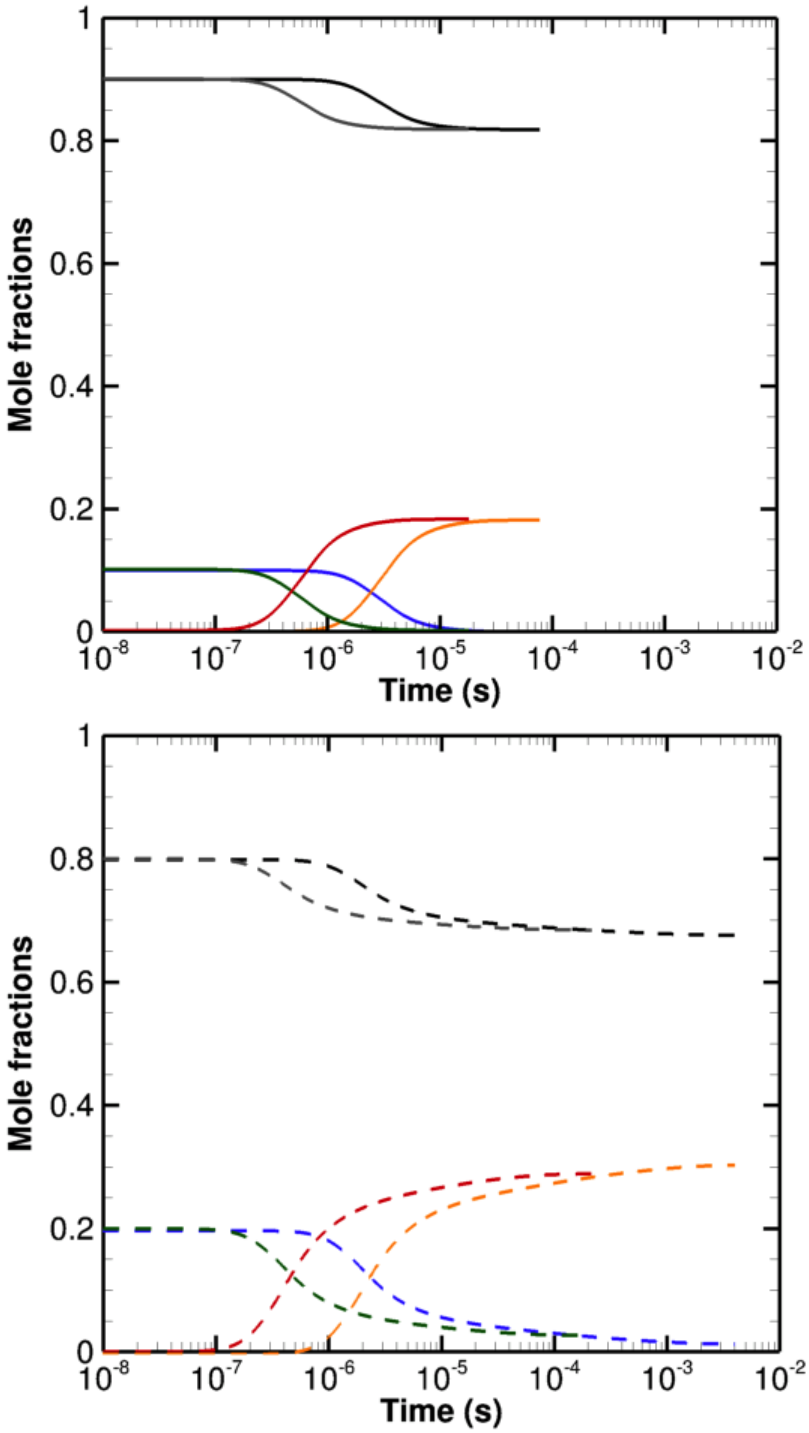

FIGURE 4.14. Time accurate mass fractions for an O_2-N system at different pressures using a $\sqrt{TT_v}$ model: Initial mole fraction of O_2 of 0.1 (above) and 0.2 (below): (■: N at 0.1 atm;■: O_2 at 0.1 atm; ■: O at 0.1 atm ; ■: N at 1 atm; ■: O_2 at 1 atm; ■: O at 1 atm)

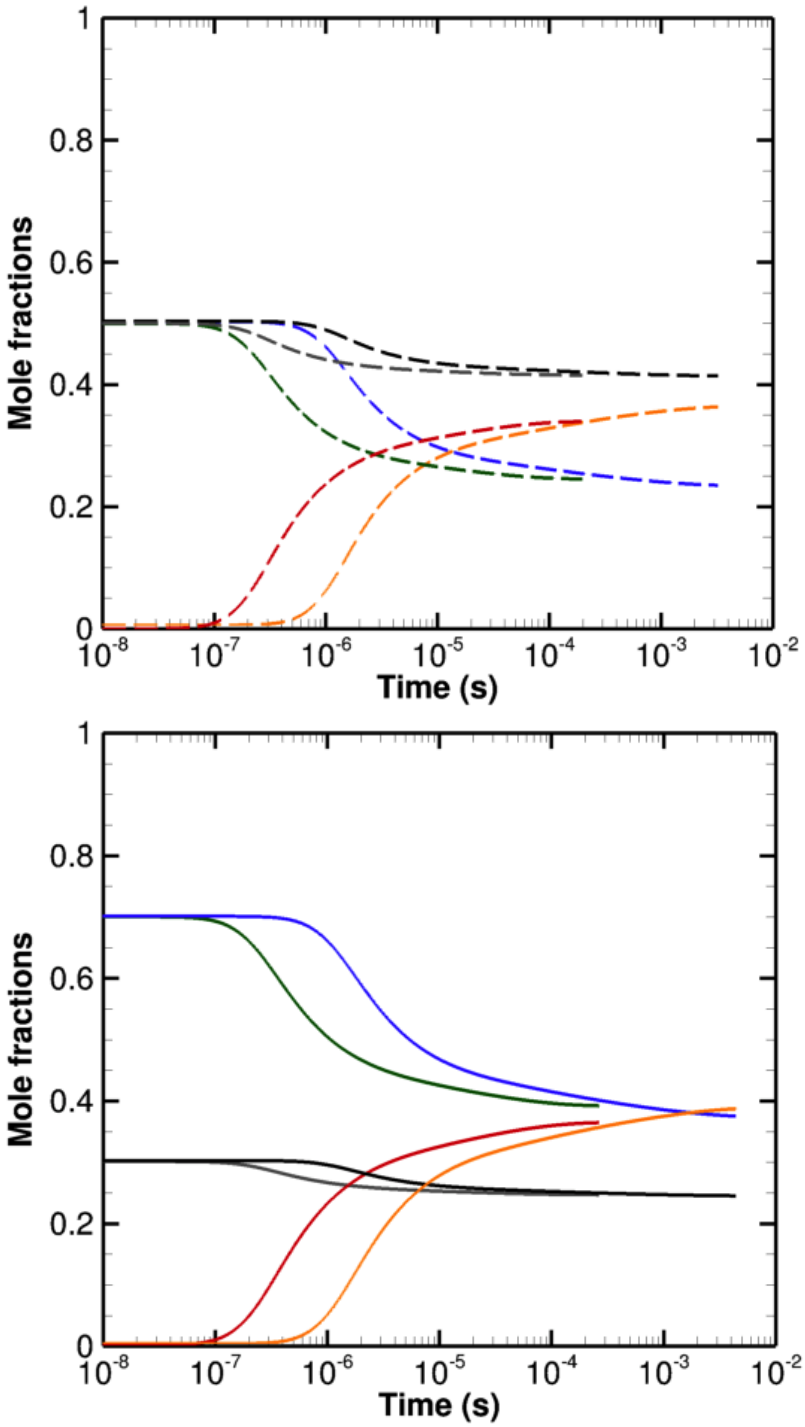

FIGURE 4.15. Time accurate mass fractions for an O_2-N system at different pressures using a $\sqrt{TT_v}$ model: Initial mole fraction of O_2 of 0.5 (above) and 0.7 (below): (■: N at 0.1 atm;■: O_2 at 0.1 atm; ■: O at 0.1 atm ; ■: N at 1 atm; ■: O_2 at 1 atm; ■: O at 1 atm)

4.4 Thermo-Chemical Relaxation Rates: Multi-Vibrational, Single Translational Temperature Model

The thermo-chemical model results depicted thus far were for a two temperature model where all the diatomic molecules in the system were represented by a single vibrational temperature. The vibrational temperature response for a heating bath system is a function of the average vibrational energy of the system. The translational-vibrational relaxation time for the two temperature model system was considered to be a function of the molar average relaxation time based on the Millikan-White model. If the gas system undergoing thermo-chemical non-equilibrium is considered to be represented by multiple vibrational temperatures, one for each polyatomic molecule in the system, the resulting non-equilibrium results are as shown in figure 4.16-4.17. At an initial O_2 mole fraction of 0.1, there are minor differences in the translational temperatures up until ~0.5μs. The variation of mean vibrational temperature for a 2T model and the vibrational temperature of N_2 are in close agreement up until ~0.5μs. However, beyond this time, the inclusion of an additional vibrational temperature for the dilute gas, O_2, results in a nearly 500 K lower temperature before reaching equilibrium. This is due to the additional energy required for the equilibration of the vibrational temperature of the dilute gas with the translational mode of the particles in the system.

At lower initial O_2 dilution levels, such as for a mole fraction of 0.5, the translational temperatures yet again are similar to each other until the attainment of equilibrium for the 2T and multi-vibrational temperature models. The vibrational temperature of O_2 also remains unaltered for the increased initial mole fraction. However, the variations between the mixture mean vibrational temperature and the vibrational temperature of N_2 begins to vary greatly, with the mean temperature skewed towards the vibrational temperature of O_2 for these systems. At this dilution level and likewise for higher levels, the final temperatures and equilibrium times do not exhibit any noticeable variation between the choice of a two-temperature and multi-vibrational temperature model.

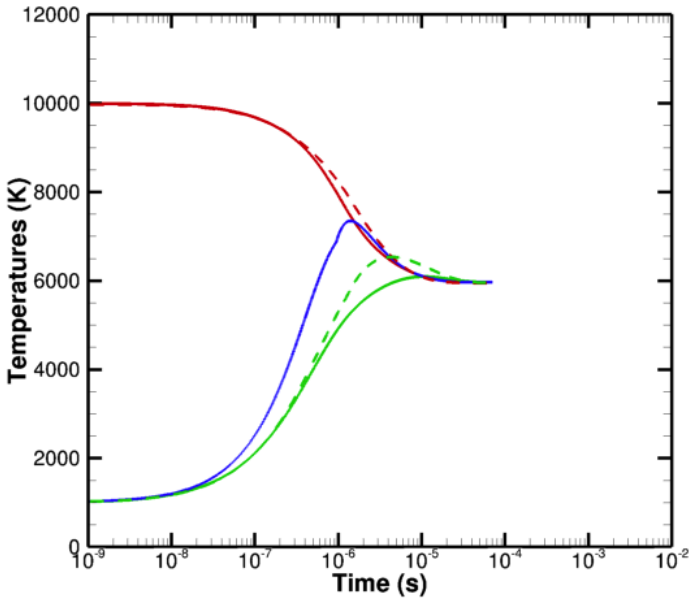

FIGURE 4.16. Comparisons between select multi-vibrational and two-temperature heat bath results for initial mole fraction of O_2 of 0.1 in an O_2-N_2 system: —— Multi-vibrational temperature model; -- -- Two temperature model; (■: Translational temperature ;■: Vibrational temperature of O_2 ; ■:Vibrational temperature of N_2)

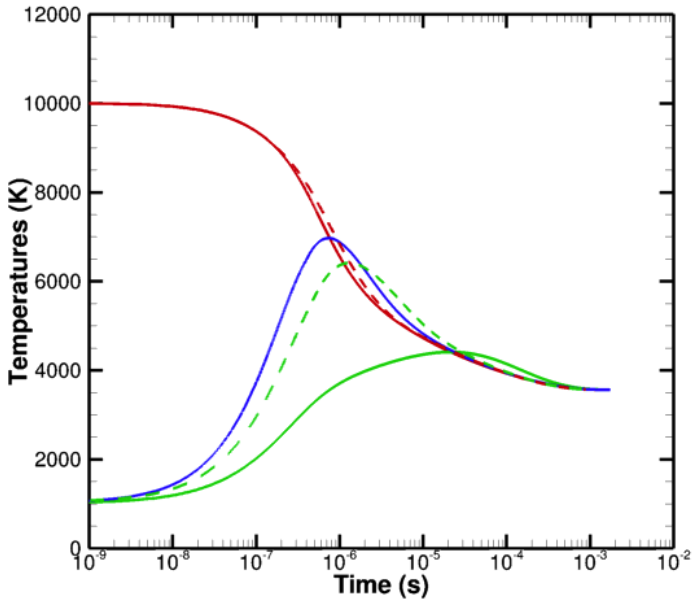

FIGURE 4.17. Comparisons between select multi-vibrational and two-temperature heat bath results for initial mole fraction of O_2 of 0.5 in an O_2-N_2 system: —— Multi-vibrational temperature model; -- -- Two temperature model; (■: Translational temperature ;■: Vibrational temperature of O_2 ; ■:Vibrational temperature of N_2)

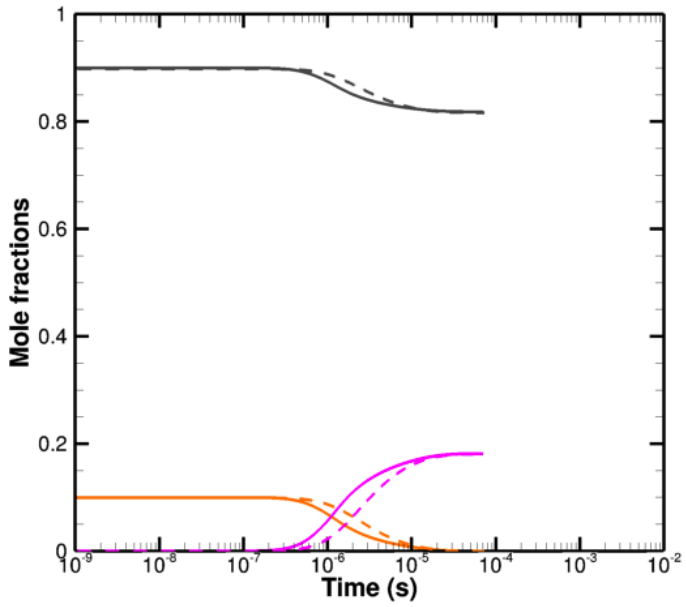

FIGURE 4.18. Comparisons between select multi-vibrational and two-temperature model mass fraction results for initial mole fraction of O_2 of 0.1 in an O_2-N_2 system:—— Multi-vibrational temperature model; - - - - Two temperature model; (■: N_2 ;■: O_2 ; ■: O)

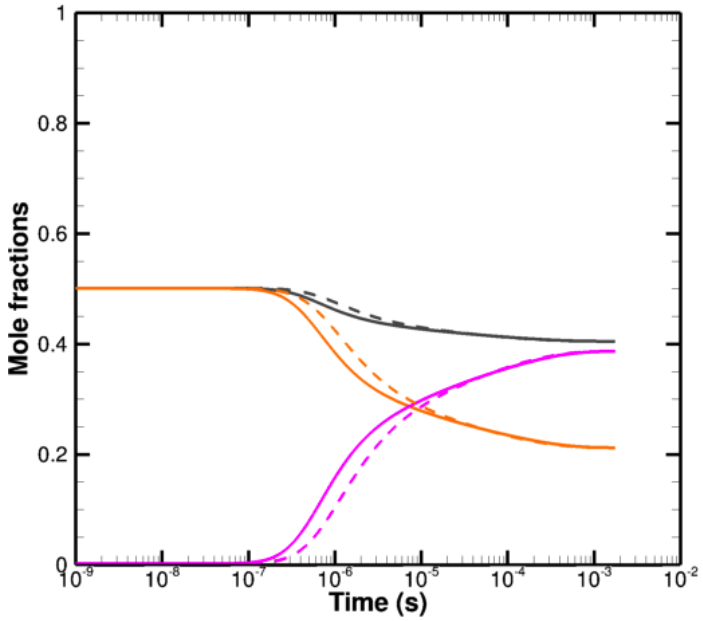

FIGURE 4.19. Comparisons between select multi-vibrational and two-temperature model mass fraction results for initial mole fraction of O_2 of 0.5 in an O_2-N_2 system: —— Multi-vibrational temperature model; - - - - Two temperature model; (■: N_2 ;■: O_2 ; ■: O)

The non-equilibrium mole fractions also conform to the physics that can be inferred from the temperature-time plots, wherein, the reactions get activated at approximately the

same time for the 2T and multi-vibrational temperature models. Interestingly, the transient differences between the models does not exceed ~ 10^{-5}s for both of the representative dilution levels depicted. Therefore, a multi-vibrational, single translational temperature model causes changes to the transient chemistry behavior of a heating system relative to the representation of the system with a single vibrational, single translational temperature model. This alteration in chemistry, due to the corresponding change in the effective temperature of the governing chemical reaction, is more significant for a system with higher concentration of dissociating molecules.

4.4.1 Numerical definition of equilbrium characteristics

It is to be noted that in all the results described in this section, the convergence criterion for the numerical simulations is when a root-mean-square residual of 10^{-12} is attained. If the data at convergence is treated as 'equilibrium', the equilibrium time variation with respect to the initial O_2 mole fraction assumes a non-monotonic variation, which is particularly enhanced for the multi-vibrational, single translational model simulations. However, if the equilibrium temperature at convergence is traced back in time to 99% of its value and is defined as the new equilibrium time for the simulations executed, the non-monotonic variations get corrected to monotonic trends with initial dilution levels. The equilibrium temperatures at these revised equilibrium times clearly asymptote to ~3500 K beyond an initial O_2 mole fraction of 0.5. The minimal differences between the two choices of thermo-chemical non-equilibrium models, as described in the previous sections, can also be seen here.

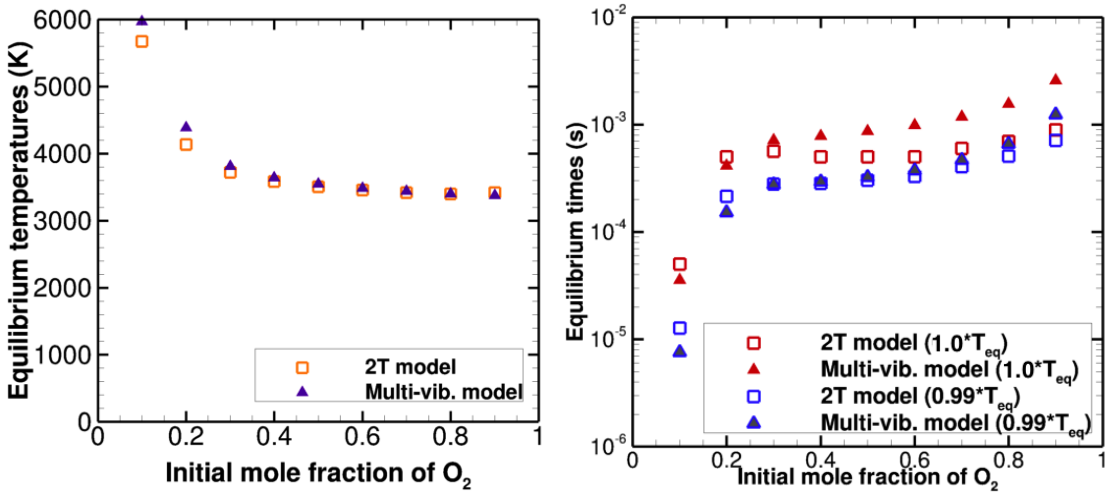

FIGURE 4.20. Comparison of equilibrium characteristics between two temperature and multi-vibrational temperature model results

4.4.2 Variation of Initial Temperature Difference

The initial temperature difference between the vibration and translational modes signifies the degree of thermal non-equilibrium. In order to understand the effects of initial temperature difference on the non-linear effects exhibited due to variations in system dilution, the following temperatures were set for the translational and vibrational modes and for the dilution range of 0.1-0.9 for an O_2-N_2 system: The simultaneous effects of initial mole fractions

TABLE 4.2. Effects of initial thermal non-equilibrium

T_{tr} (K)	T_v (K)
10000	1000
10000	2000
10000	5000
10000	8000

and initial thermal non-equilibrium on the equilibrium characteristics can be demonstrated by a response surface. This surface response for the equilibrium temperature and inter-species relaxation times are shown in figures 4.21 and 4.22. It can be seen that these two features nearly complement each other. In particular, for low initial mole fractions of O_2 in the reacting mixture and low initial thermal non-equilibrium, the final equilibrium temperature is largely dictated by the temperature of the translating particles in the mixture. At these conditions, the inter-species relaxation time takes on the least value on the response surface. This behavior is reversed at higher initial mole fractions of O_2 and larger initial degree of thermal non-equilibrium. This increase in inter-species relaxation time is 75% within the extremes of the response surface. The depiction of pressure variation on the resulting inter-species relaxation results in a slightly skewed surface relative to the response of equilibrium temperatures to the provided initial conditions. The reduction of inter-species relaxation at the extremes of initial mole fraction and thermal non-equilibrium correspond to a ~ 50% reduction in pressure of the system.

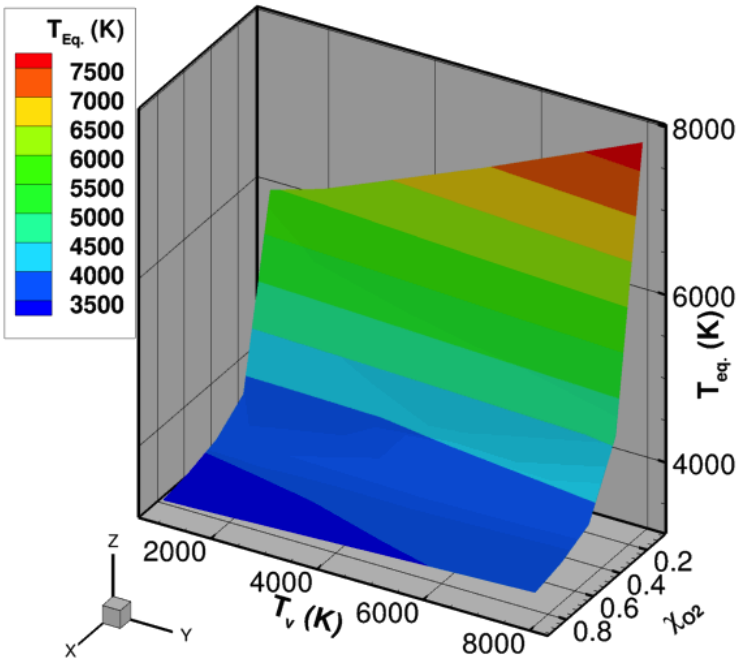

FIGURE 4.21. Equilibrium temperature surface response to variations in initial mole fraction of O_2 and initial temperature difference between the translational and vibrational modes: $T_{tr} = 10000$ K

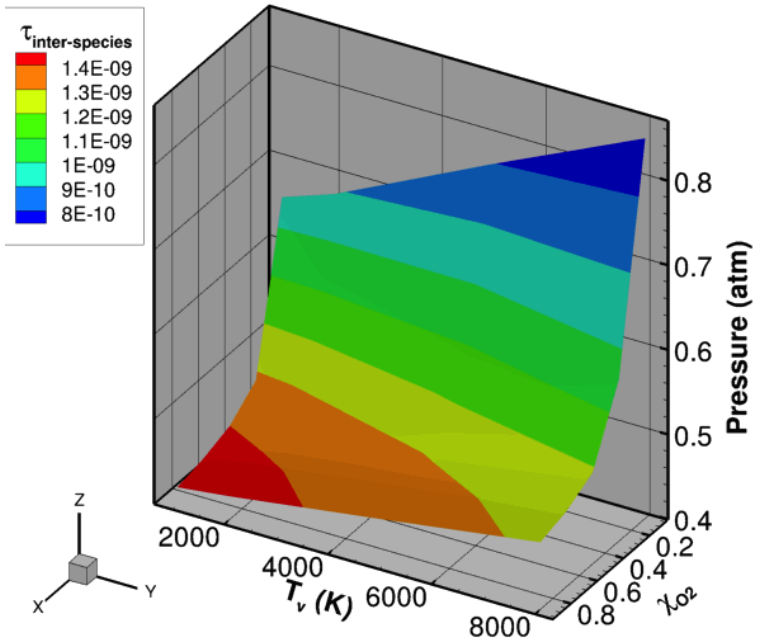

FIGURE 4.22. Equilibrium inter-species relaxation time (between O_2-O_2, O_2-N_2 and N_2-N_2) surface response to variations in initial mole fraction of O_2 and initial temperature difference between the translational and vibrational modes: $T_{tr} = 10000$ K

CHAPTER 5
HYPERSONIC FLOW RESULTS FOR MULTI-TEMPERATURE MODELS

5.1 Introduction

In order to validate the non-equilibrium flow solver developed, several two dimensional flows around bodies of varying shapes were simulated. In the results presented in this chapter, the variations resulting from using different internal energy modeling approaches are demonstrated. These modeling approaches which include chemical and thermal non-equilibrium have been identified by Candler [61] to have first order effects on the flow field. The validations carried out in this chapter to other numerical as well as experimental data seek to demonstrate these effects.

5.2 Conical flows

For initial validations of the flow solver, a 45^0 half-cone was considered, and comparisons made of different models. The freestream density is 0.0148 N/m^2 and the freestream velocity is 6350 m/s. This test case was used by Spurk [62] to present numerical and experimental results when different relaxation times were considered to be dominant. Oxygen was chosen as its reaction kinetics were widely studied at the time of conducting those experiments.

The main experimental tool used was a Mach-Zehnder optical interferometer to observe the stationary flow around the model and the freestream flow. The hypersonic oxygen flow was generated in an expansion tube to attain a freestream compressibility factor of 1. The experimental shock shape and fringe width were used to compare to numerical results obtained by using a shock-fitting method. His computations used the Treanor and Marrone [7] model to account for the effect of vibrational relaxation on dissociation. Ionization was neglected and anharmonicity of oscillators was taken in to account while computing the vibrational energy.

This case was set up in NASCART-GT and primarily three overlapping energy exchange processes were considered here:

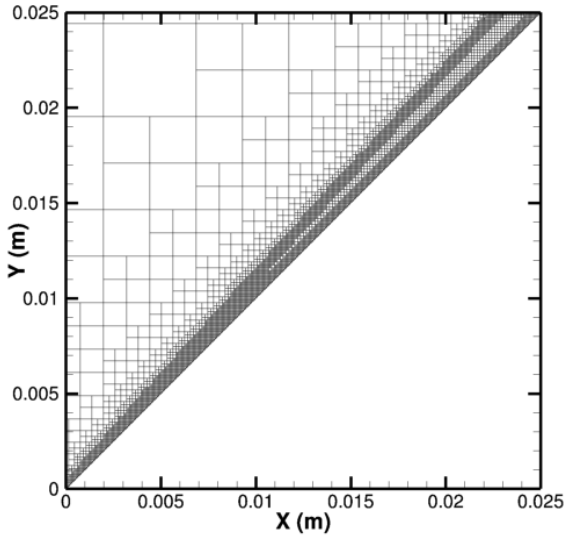

FIGURE 5.1. Computational grid used for a 45^0 1/2 cone angle geometry thermo-chemical non-equilibrium simulation in NASCART-GT

(i) Thermally perfect and chemically frozen flow

(ii) Thermal equilibrium and chemically frozen flow

(iii) Thermal non-equilibrium and chemical non-equilibrium

The computational grid used for this case is shown in figure 5.1, and the contour plots in figures 5.2-5.4 depict the general nature of the flowfield. As seen in figures 5.2, 5.3 and 5.4, the greatest shock detachment distance was noticed corresponding to the results for calorically perfect gas assumptions, with greatest peak temperatures noticed under the same conditions. The considerations of thermal equilibrium and therm-chemical non-equilibrium results in smaller detachment distances.

From figure 5.5, it can be seen that the thermo-chemical non-equilibrium results which were computed using a temperature dependent form of the reaction rate equations involving O_2-O_2 and O_2-O collisions, showed the closest agreement with Spurk's experimental data. The measurements of the shock location using an interferogram had a large amount of scatter with a combined error of 20% reported for the freestream density measurement. Spurk's non-equilibrium results, which included a temperature dependent relative efficiency, yielded the closest agreement to his experimental results. The relative efficiency, P^*, was defined by the following ratio of rate constants where A is any colliding partner:

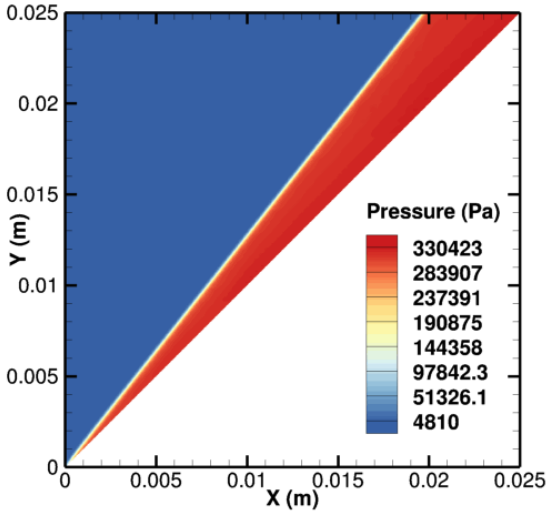

(A) $\tau_{VIB} = \infty$, $\tau_{DISS} = \infty$

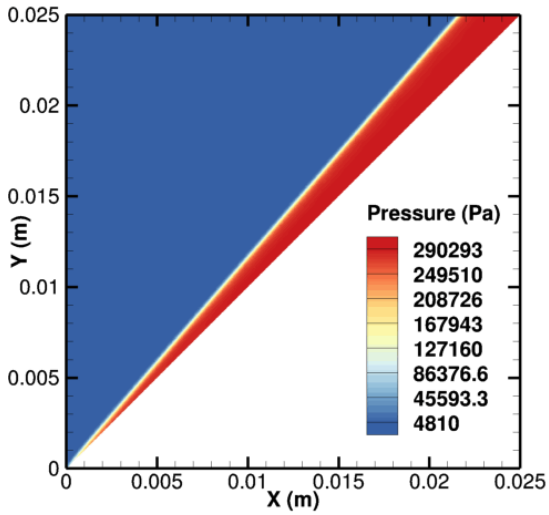

(B) $\tau_{VIB} = 0$, $\tau_{DISS} = \infty$

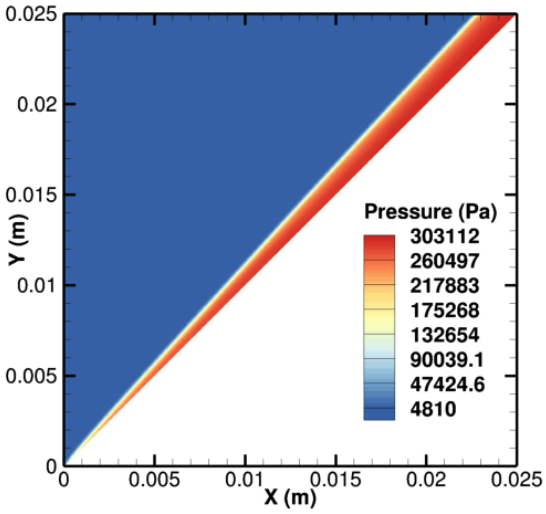

(C) $0 < \tau_{VIB}, \tau_{DISS} < \infty$

FIGURE 5.2. Pressure contours for a 45^0 1/2 cone angle geometry simulations

$$P^* = \left[\frac{k_d(O_2 - O, O_2)}{k_d(O_2 - A)}\right]\left[\left\langle\frac{\sigma_{O,O_2}}{\sigma_A}\right\rangle\left\langle\frac{\mu_{O,O_2}}{\mu_A}\right\rangle\right] \tag{5.1}$$

The result obtained using the two temperature thermo-chemical model in NASCART-GT was in close agreement with Spurk's numerical and experimental data near the leading edge. The largest deviation observed between the numerical results obtained in the present work and those reported by Spurk was 14.8%. The uncertainty reported for the thermo-

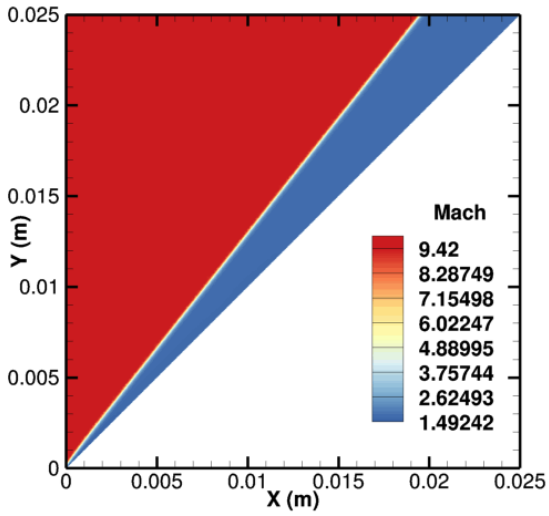

(A) $\tau_{VIB} = \infty$, $\tau_{DISS} = \infty$

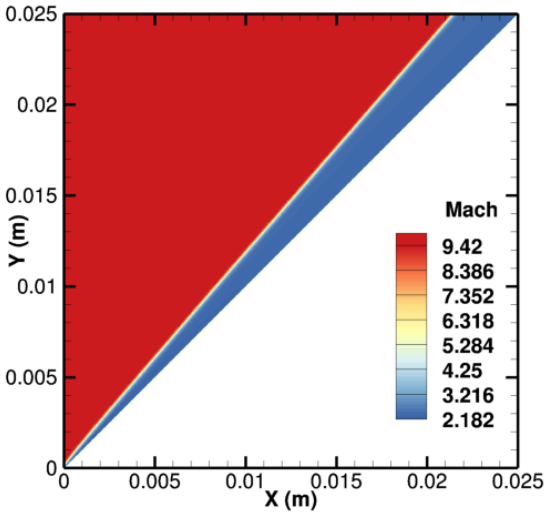

(B) $\tau_{VIB} = 0$, $\tau_{DISS} = \infty$

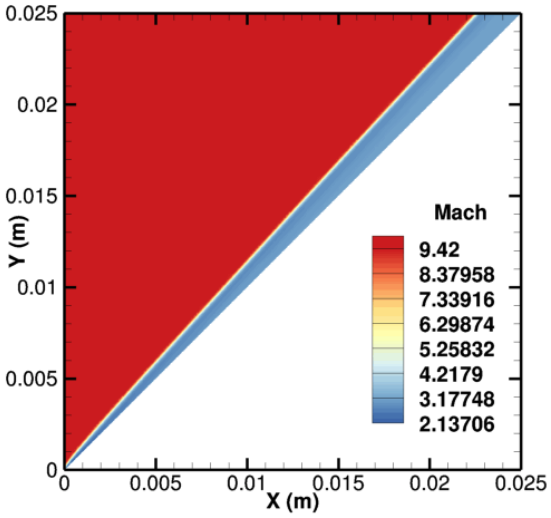

(C) $0 < \tau_{VIB}, \tau_{DISS} < \infty$

FIGURE 5.3. Mach contours for a 45^0 1/2 cone angle geometry simulations

chemical results obtained by Spurk assuming constant relative efficiency was stated to be "20-30%" smaller than experimental findings. It is to be noted that his computations predicted freestream vibrational energy based on the equilibrium temperature in the shock reflected region. On the contrary, NASCART-GT uses thermal non-equilibrium in the freestream too, resulting in non-equilibrium considerations throughout the computational flow-field. Furthermore, the present work assumes an empirical coupling (Park's $\sqrt{TT_v}$ model) between vibrational and dissociation energies and harmonic oscillators in the gas

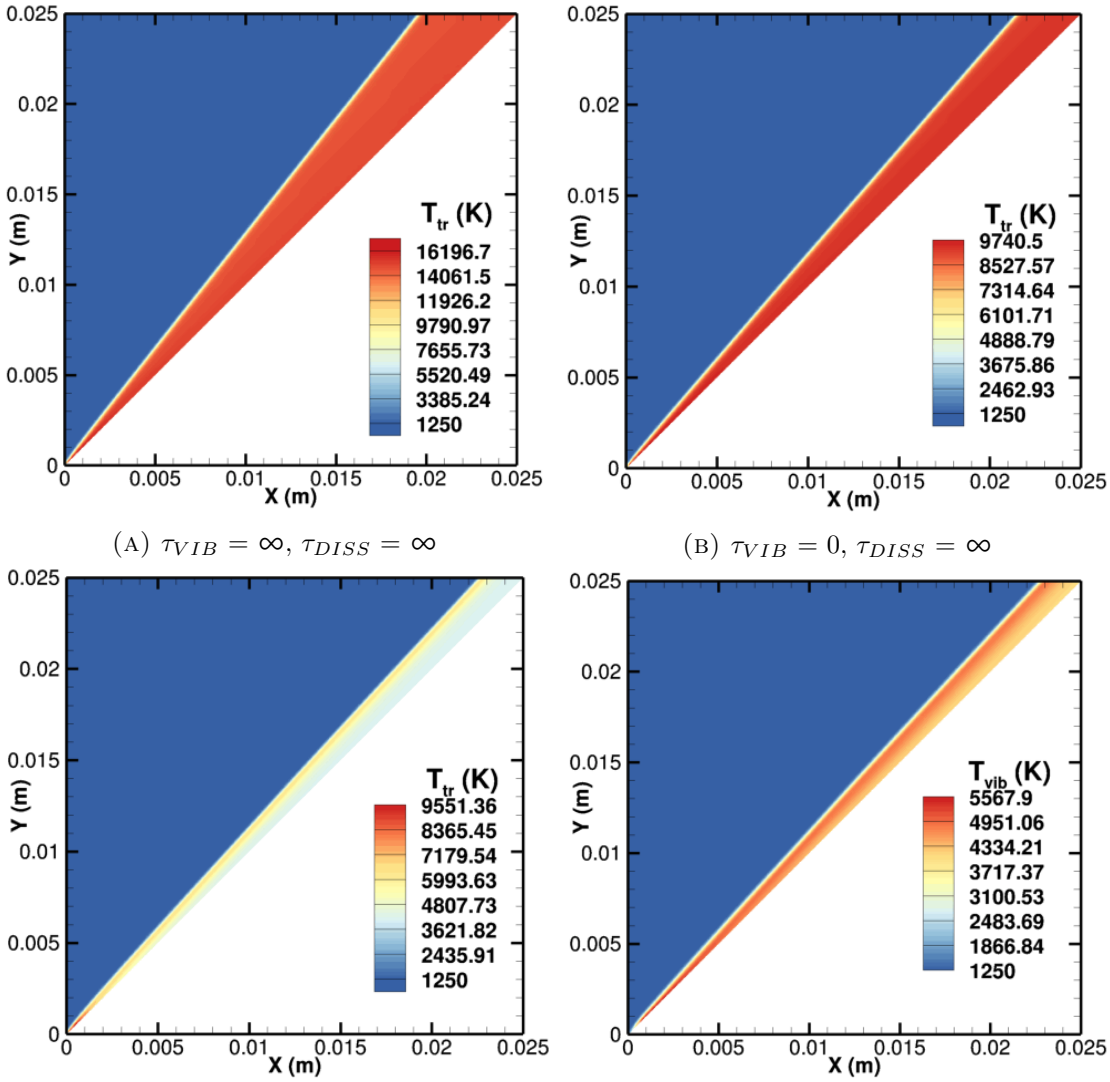

(A) $\tau_{VIB} = \infty$, $\tau_{DISS} = \infty$

(B) $\tau_{VIB} = 0$, $\tau_{DISS} = \infty$

(C) $0 < \tau_{VIB}, \tau_{DISS} < \infty$

(D) $0 < \tau_{VIB}, \tau_{DISS} < \infty$

FIGURE 5.4. Temperature contours for a 45^0 1/2 cone angle geometry simulations

mixture. However, significantly different underlying energy exchange models were used by Spurk in his numerical computations. The dissociate rate constants used by Spurk were based on Camac and Vaughan's [63] shock tube measurements involving O_2-Ar mixtures and extrapolated to the temperatures measured in experiments. On the contrary, the numerical results obtained using NASCART-GT were based on the O_2 dissociation reactions in Park's model [64]. The vibrational temperatures obtained in the present work are in the "low-temperature regime", i.e., $\sim < 5000^o$ K. In this regime, as reported by Stupochenko et al. [65] and reiterated by Spurk [62], the O_2-O_2 energy transfer is more effective than

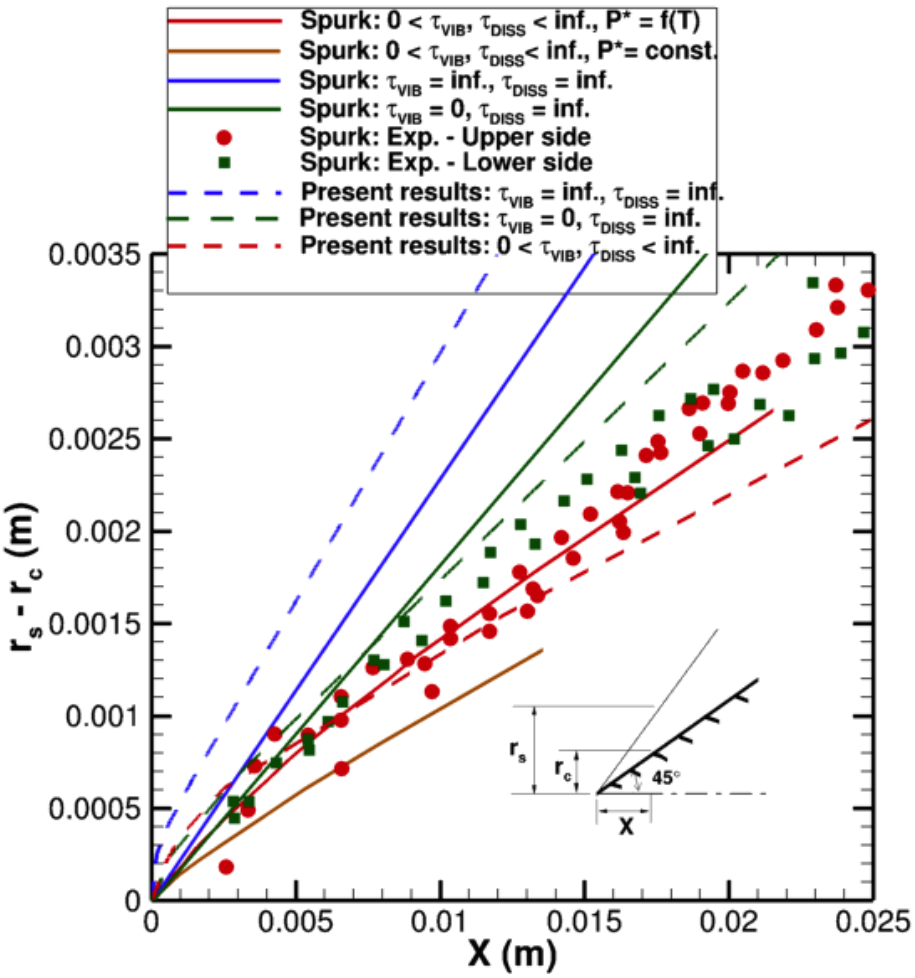

FIGURE 5.5. Comparison between NASCART-GT results and Spurk's data for a 45^0 1/2 angle cone in a Mach 9.42 flow of O_2. P* is the efficiency factor as defined by Spurk [62]. $r_S - r_C$ refers to the shock detachment distance.

that observed between O_2 and Ar. The extrapolation of O_2-Ar reaction rate constants in this temperature regime may therefore cause significant differences compared to the direct measurements of O_2-O_2 reaction rates.

The chemically frozen numerical results predicted by Spurk indicate a larger shock detachment distance. The larger differences between the numerical results in the present work and those by Spurk can be attributed to the shock curvature which is captured in the 2D axisymmetric result of NASCART-GT. This curvature was captured by Spurk only while using the constant and variable efficiency models for thermo-chemical non-equilibrium. The differences in shock curvature at the leading edge of the cone can be attributed to the use of shock fitting methods by Spurk as against a shock capturing method used in the present

work. Nonetheless, large variations can be seen between the choice of a calorically perfect gas and the experimental results. This error for the calorically perfect gas case exceeds 100% and is in agreement with the results obtained numerically by Spurk and others [61, 62]. This test case which contains experimental and numerical data to compare with, serves to validate and demonstrate that thermo-chemical non-equilibrium considerations leads to the closest agreement with experimental data.

5.3 Double wedge flows

One of the more challenging cases for validation of flow solvers is the double wedge problem. This problem consists of complex shock-shock interactions and lends itself well for testing of implemented schemes and resulting physics. Historically, the appearance of large variations in heat transfer rate and surface pressure, and the inability to understand the underlying complex phenomena led Oleniczak et al. [66] to embark on a study on a double wedge configuration in inviscid flow. By removing the component of viscosity from the governing equations, the interplay between finite rate chemical reactions and hypersonic flow was studied. Their study included a M_∞ = 9.0 air flow over a double wedge configuration of θ_1 = 15^0 and θ_2 = 45^0 respectively for the first and second wedge. The flow physics was studied using the Data Parallel Lower-Upper Relaxation implicit method and perfect gas assumptions. The experiments performed by Bertin and Hinkle [67] had indicated a steep transition from a Type VI – Type V transition within 2^0 of the maximum deflection angle. However, their numerical simulations showed a gradual transition in the Edney [68] Type VI - Type V interaction process over a series of second wedge angles in the range of 39.5^0 - 42.5^0. The largest second wedge angle that produced a Type V interaction was 45.25^0. Their study involved studying such interactions over a range of Mach numbers and second wedge angles. Such transitions can not be studied analytically and numerical simulations of this type are useful in understanding the underlying physics.

Coratekin et al. [69] used this test case to study the performance of Upwind schemes such as the advection upstream splitting method (AUSM), and its modified form, AUSMDV scheme incorporated in to an explicit finite volume flow solver. The AUSM scheme, proposed by Liou and Steffen [70] splits the inviscid flux vector in to an advective and pressure term. The AUSMDV scheme, produced from a combination of the AUSMD and AUSMV scheme [71], allows for a switching between the two schemes based on the local pressure gradient. Both, the AUSM and AUSMDV schemes resulted in pressure oscillations behind the shock waves. Furthermore, a utilization of the van Leer limiter resulted in the break up of the shear layer in to vortical structures. Their results qualitatively agreed well with those of Olejniczak et al. [66]. However, their study was unable to distinguish between the physical

accuracy of the appearance of vortical structures and the numerical effects of switching between flux limiters (minmod and Van Leer).

More recently, Li et al. [72] studied the type VI – V transition in hypersonic double wedge flows using thermo-chemical non-equilibrium effects. This study deviated from the previous studies [66, 73, 74] in that the real gas effects were emphasized. Much of their work was based on introducing a non-equilibrium relaxation length by analyzing the relaxation characteristics. The thermo-chemical non-equilibrium model used was the two-temperature model and Park's five species chemical kinetics model [64]. It was found that the non-equilibrium gas effects lead to larger second wedge angle for the shock transition from type VI – V, with greater effects seen with increasing the Mach number of the inflow. The unstructured grid used in Li et al.'s [72] work was adapted based on the maximum error of density and two components of velocity.

Xiong et al. [75] also studied the involved wave patterns over a double wedge using an inviscid two-temperature model and Park's two temperature model. Their vectorized two dimensional adaptive finite volume solver was used at a freestream Mach number of 9, freestream temperature and pressure of 500 K and 0.1 atm respectively. They observed a hysteresis phenomenon during the transition from a regular reflection to an overall Mach reflection, and also found that non-equilibrium effects lead to a larger critical angle.

All the above studies have well established that real gas effects play a significant role in the study of complex inviscid phenomena occurring in shock-shock interactions. Some of the case studies undertaken by Li et al. [72] will be studied in order to validate the non-equilibrium framework implemented in this work. As an increase in complexity from the conical flows tested, coupled thermo-chemical non-equilibrium capabilities are tested in addition to chemical non-equilibrium and frozen flow computations.

5.3.1 Effect of freestream Mach number

The first set of cases computed were targeted at seeking an understanding of the effect of Mach number on the shock-shock interactions at a double wedge with $\theta_1 = 15^0$ and $\theta_2 = 45^0$. The three freestream Mach numbers tested were 9, 11 and 15. The computational grids resulting from solution adaptation based on velocity divergence and Mach number are shown

in figures 5.7 - 5.10. The grids for a calorically perfect gas depict the shock interaction pattern that is typical of an Edney type V interaction, and agree well with literature results (see figure 5.14). The seven shock structure is captured by NASCART-GT, with the triple shock structure formed by the impinging shock at the first wedge, and the shock emanating at the compression corner, clearly formed by highly resolved Cartesian cells. The remaining shocks, including the reflected waves, are resolved in accordance with the gradients present. With the increase in Mach number, and in accordance with the nomenclature depicted in figure 5.6(b), point P gets displaced closer to the surface resulting in a greater curvature of shock PS. The adaptation of Cartesian cells along the expansion fans are seen in the grids too, although they are not as discernible as the shock structures.

The computational grids for chemical and thermo-chemical non-equilibrium modeling

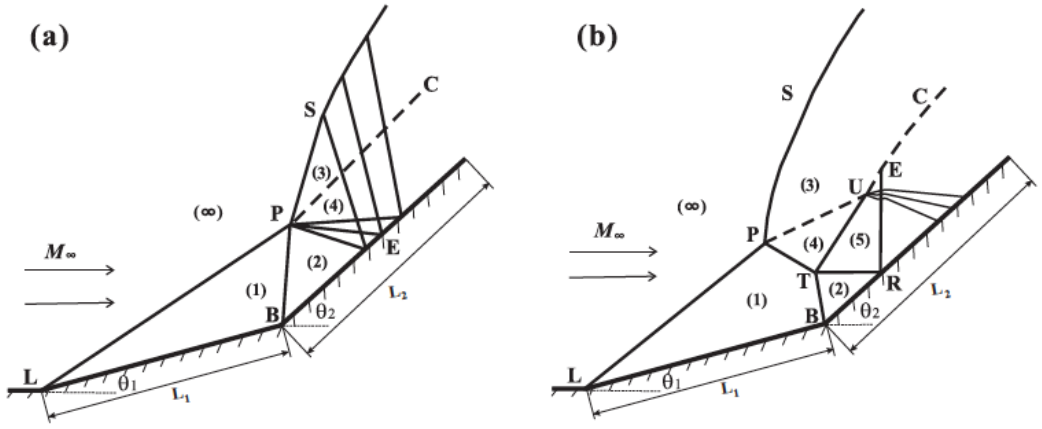

FIGURE 5.6. Schematic diagrams of Type VI (a) and Type V (b) interactions [72]

result in the Type VI interaction. At any given freestream Mach number, thermal non-equilibrium effects reduce the deflection of impinging shock BP at the second wedge. The contour plots for a calorically perfect gas model at M_∞ = 9 (figure 5.11) reveal the existence of a subsonic pocket past the triple shock. The peak temperature seen in this region is about 5000 K. Corresponding results for chemical non-equilibrium (figure 5.12) reveal that the peak temperature in the post shock region of a type VI interaction does not exceed 3600 K. The contours of chemical species (figure 5.13) in the region of peak temperatures indicate that there is a mild dissociation of N_2 and correspondingly low concentrations of NO and N in these regions. Peak atomic oxygen values exist to the extent of 1.5% by vol-

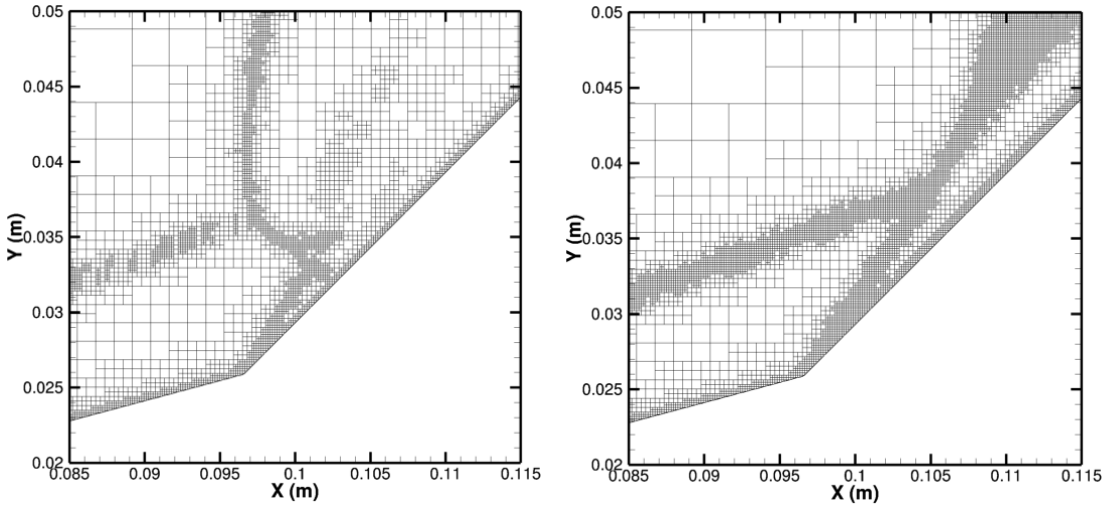

(A) Calorically perfect gas

(B) Chemical non-equilibrium

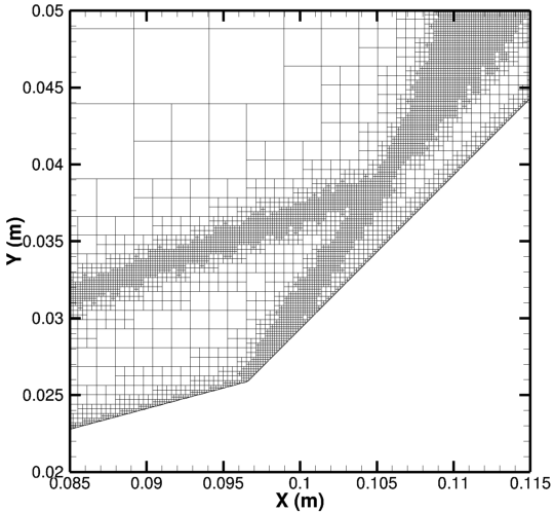

(C) Thermo-chemical non-equilibrium

FIGURE 5.7. Computational grids in NASCART-GT for a Double Wedge using a calorically perfect gas, chemical non-equilibrium and thermo-chemical non-equilibrium assumptions: θ_1 = 15 and θ_2 = 45 in Mach 9 air flow

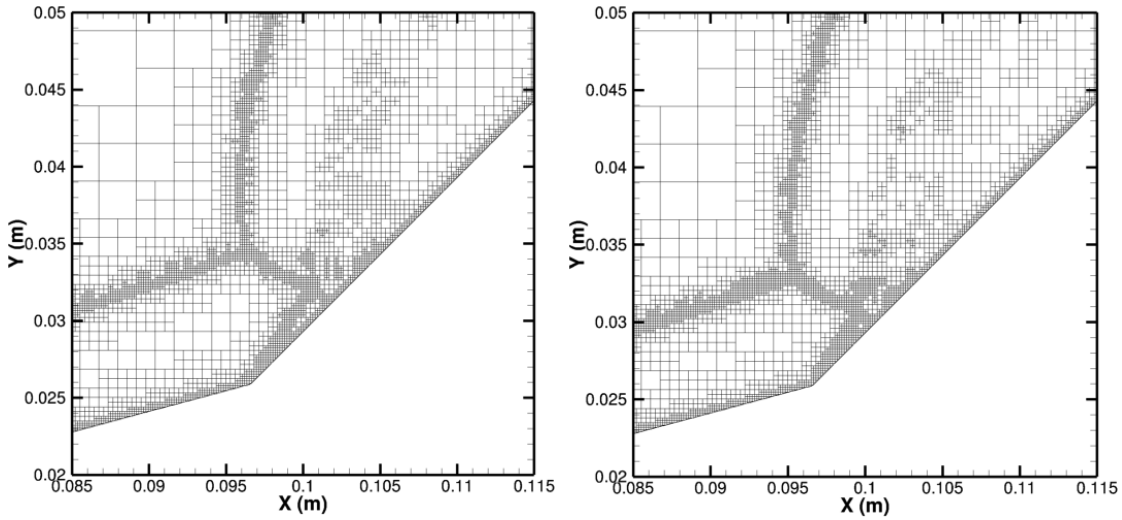

FIGURE 5.8. Comparison of computational grids in NASCART-GT for a Double Wedge using calorically perfect gas air assumptions at M_∞ = 11 (left) and at M_∞ = 15 (right): θ_1 = 15 and θ_2 = 45

ume. At M_∞ = 11 and for calorically perfect gas assumptions, a similar subsonic pocket is seen with a higher peak temperature of about 7000 K. The one temperature model results at this Mach number have a marginal increase in peak translational temperature compared to the corresponding results at M_∞ = 9. Calorically perfect gas assumptions thus indicate a greater sensitivity to the freestream Mach number than chemical non-equilibrium considerations.

Thermo-chemical considerations, as can be seen from the M_∞ = 11 contour plots (figure 5.18), show that the translational and vibrational temperatures are nearly identical in the shock interaction region, with the peak vibrational temperature ~ 200 K lesser than the peak translational temperature. These similar profiles indicate near-thermal equilibrium conditions thereby rendering thermo-chemical modeling to exhibit second order effects when $\theta_2 = 45^0$. The mass fractions in the interaction region possess higher values corresponding to the higher freestream Mach number, the most significant increase indicated in atomic nitrogen which increases by an order of magnitude at M_∞ = 11.

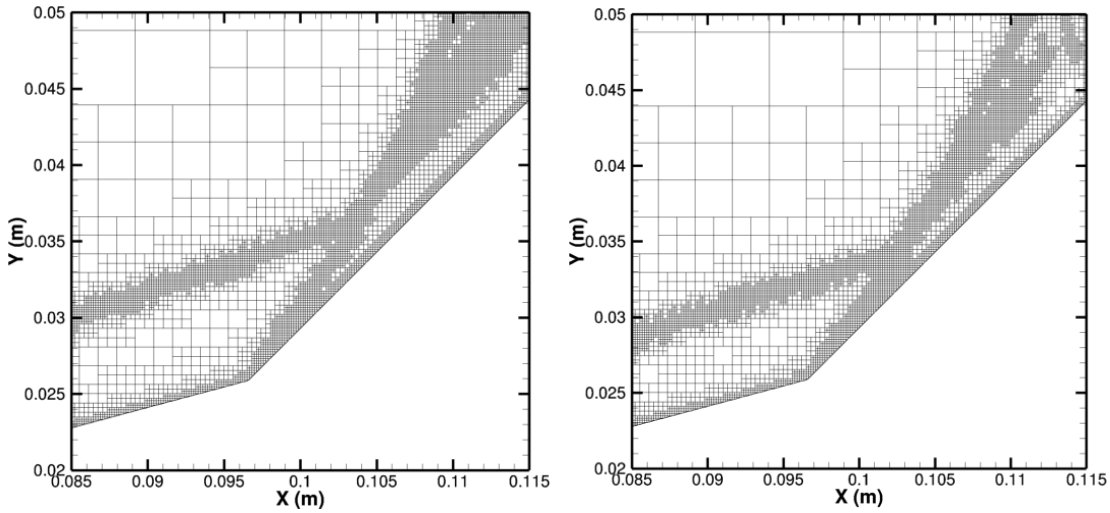

FIGURE 5.9. Comparison of computational grids in NASCART-GT for a Double Wedge using chemical non-equilibrium (1-temperature model) at M_∞ = 11 (left) and at M_∞ = 15 (right): θ_1 = 15 and θ_2 = 45

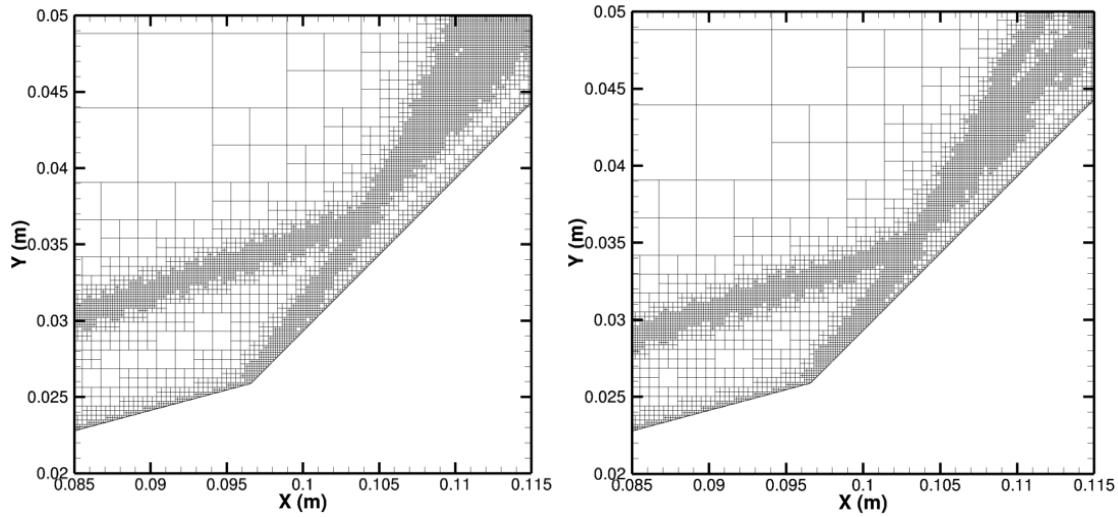

FIGURE 5.10. Comparison of computational grids in NASCART-GT for a Double Wedge using thermo-chemical non-equilibrium (2-temperature model) at M_∞ = 11 (left) and at M_∞ = 15 (right): θ_1 = 15 and θ_2 = 45

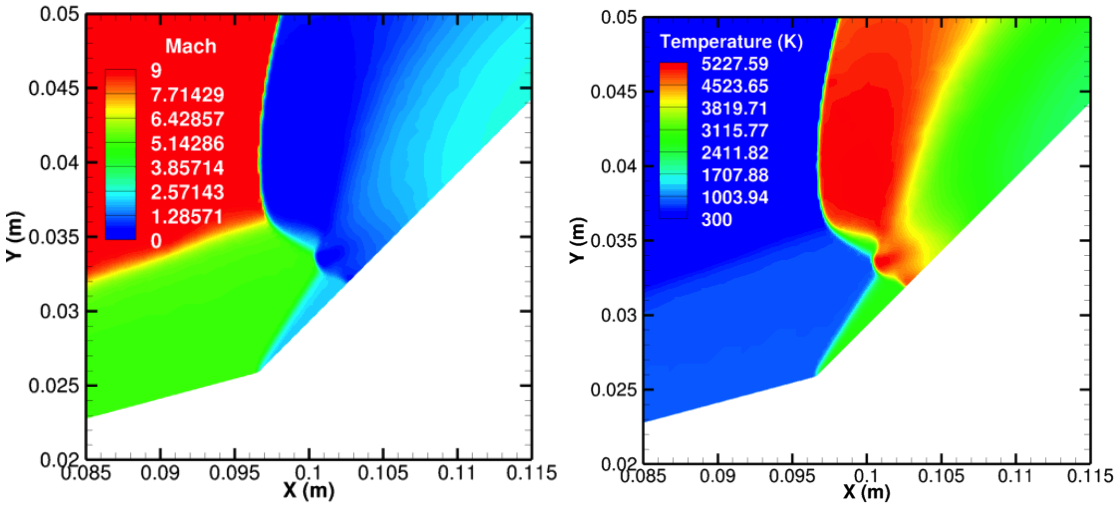

FIGURE 5.11. Mach and Temperature contours using a calorically perfect gas model for a Double Wedge: θ_1 = 15 and θ_2 = 45 in Mach 9 air flow

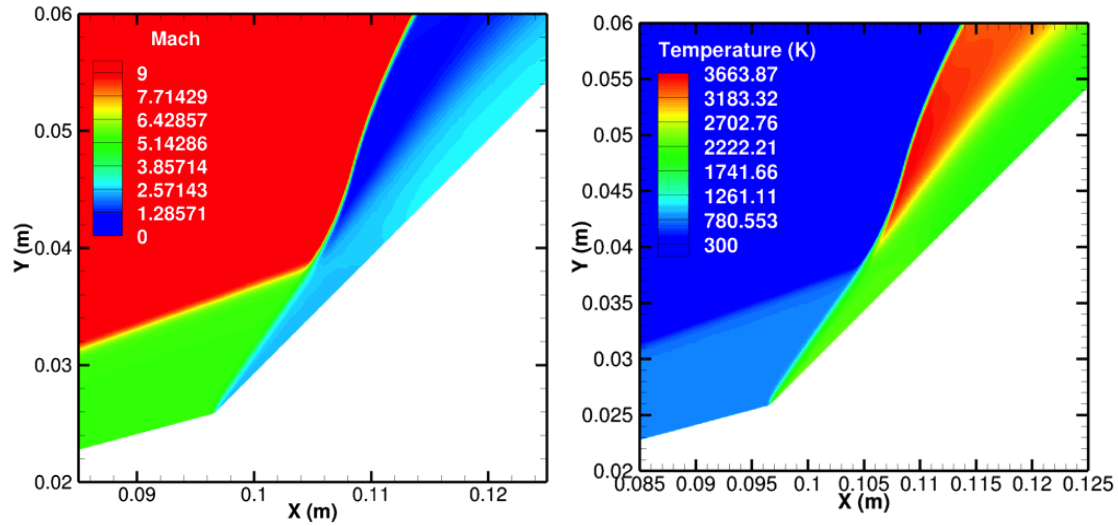

FIGURE 5.12. Mach and temperature contours using a one temperature model for a Double Wedge: θ_1 = 15 and θ_2 = 45 in Mach 9 air flow

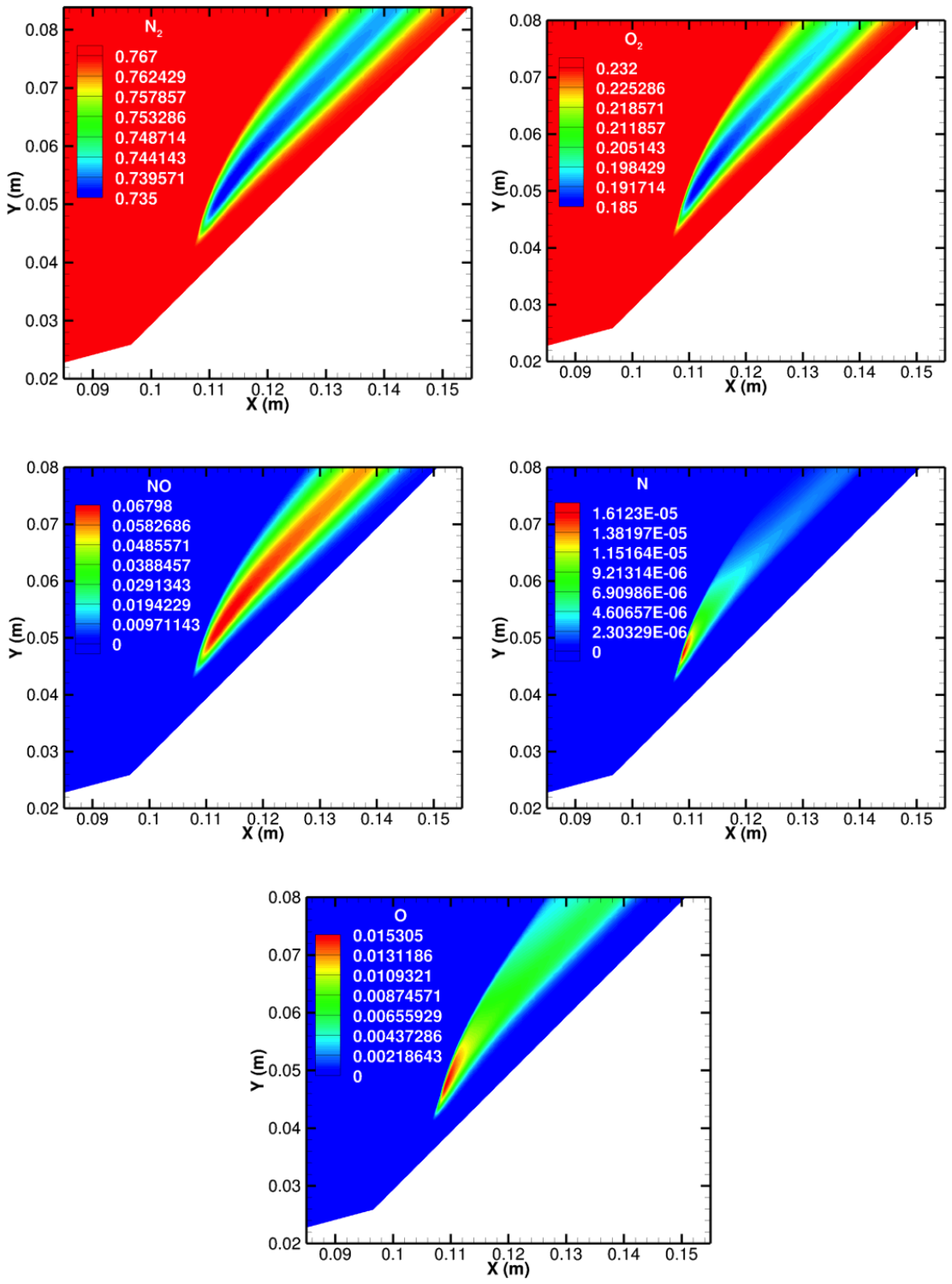

FIGURE 5.13. Mass fraction contours using a one temperature gas model for a Double Wedge: θ_1 = 15 and θ_2 = 45 in Mach 9 air flow

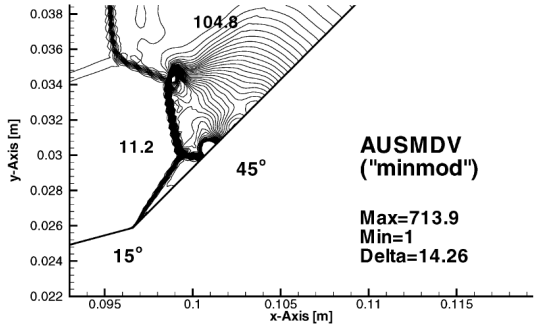

FIGURE 5.14. Double wedge results obtained by Coratekin et al. [69]: $\theta_1 = 15^0$, $\theta_2 = 45^0$, $M_\infty = 11$ with calorically perfect gas assumptions

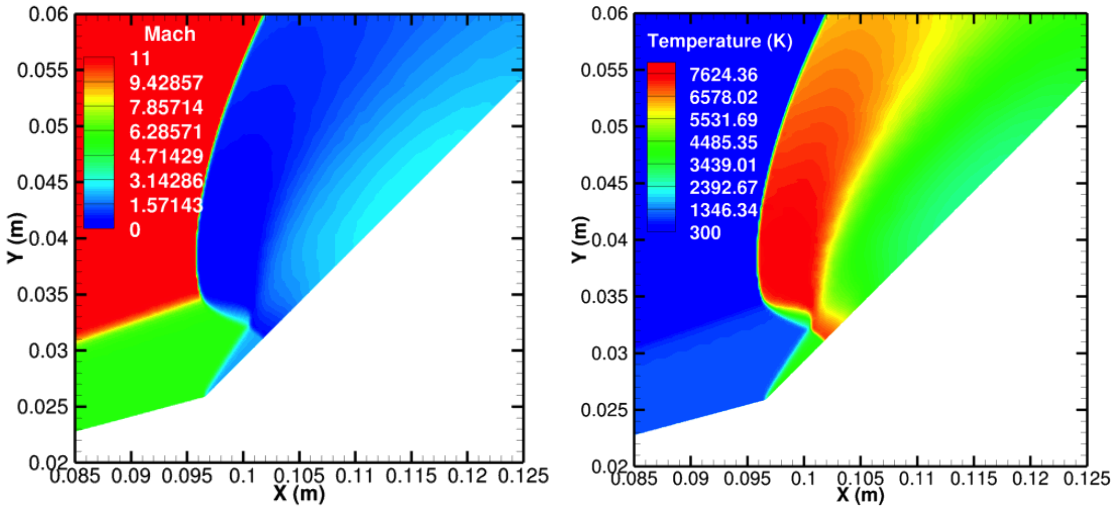

FIGURE 5.15. Mach and Temperature contours using a calorically perfect gas model for a Double Wedge: $\theta_1 = 15$ and $\theta_2 = 45$ in Mach 11 air flow

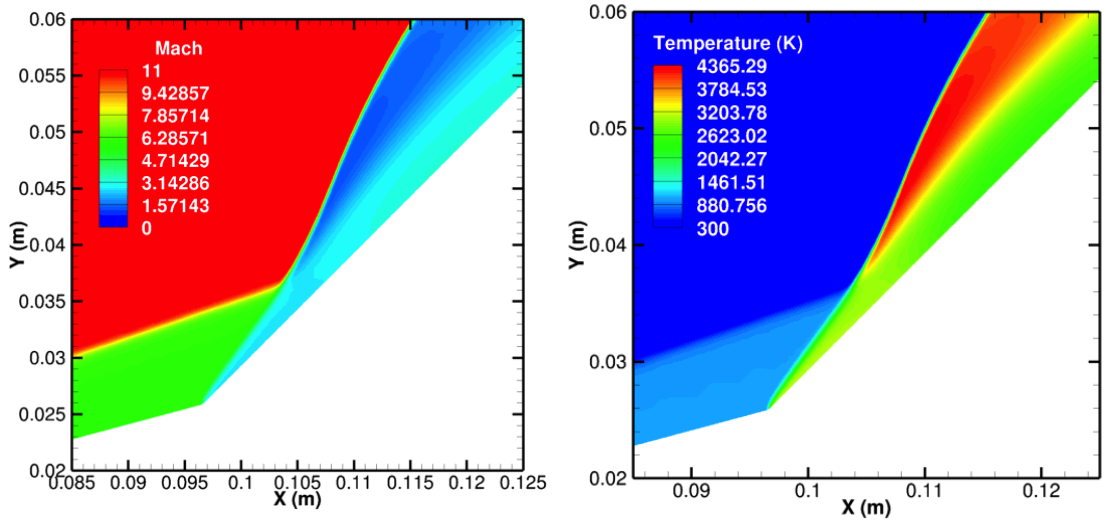

FIGURE 5.16. Mach and Temperature contours using a one-temperature gas model for a Double Wedge: $\theta_1 = 15$ and $\theta_2 = 45$ in Mach 11 air flow

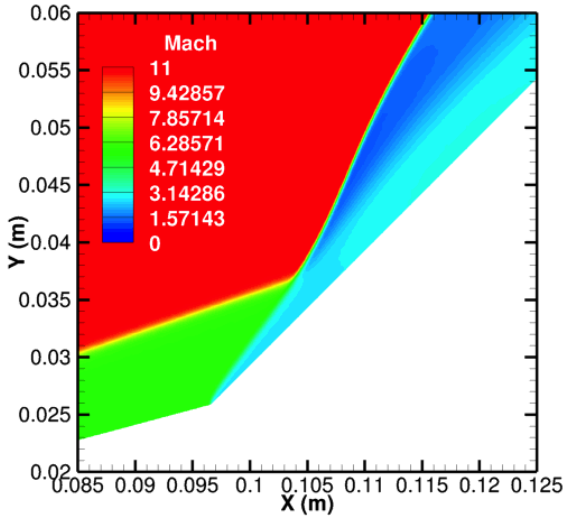

FIGURE 5.17. Mach contours using a two-temperature gas model for a Double Wedge: θ_1 = 15 and θ_2 = 45 in Mach 11 air flow

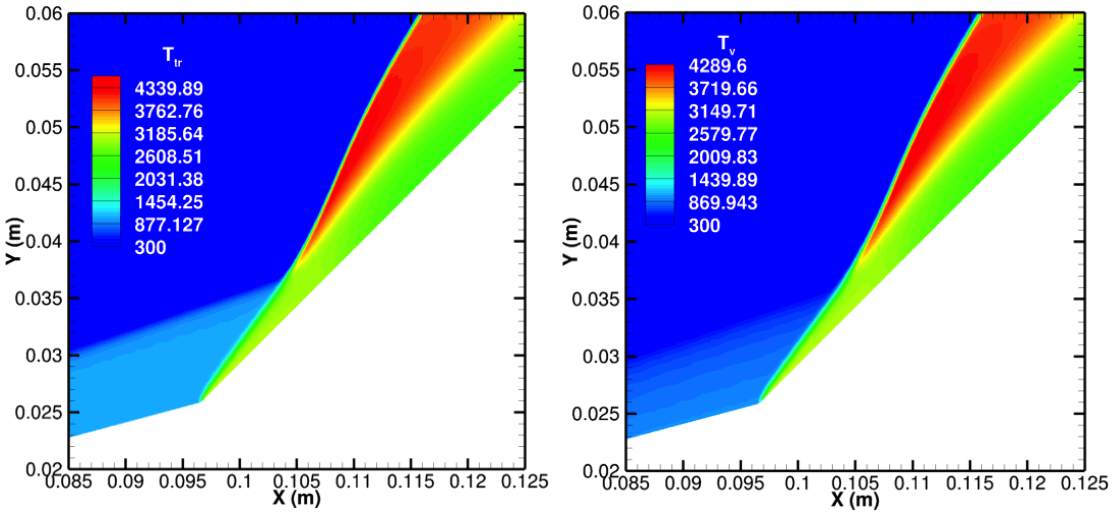

FIGURE 5.18. Translational and Vibrational Temperature contours using a two-temperature gas model for a Double Wedge: θ_1 = 15 and θ_2 = 45 in Mach 11 air flow

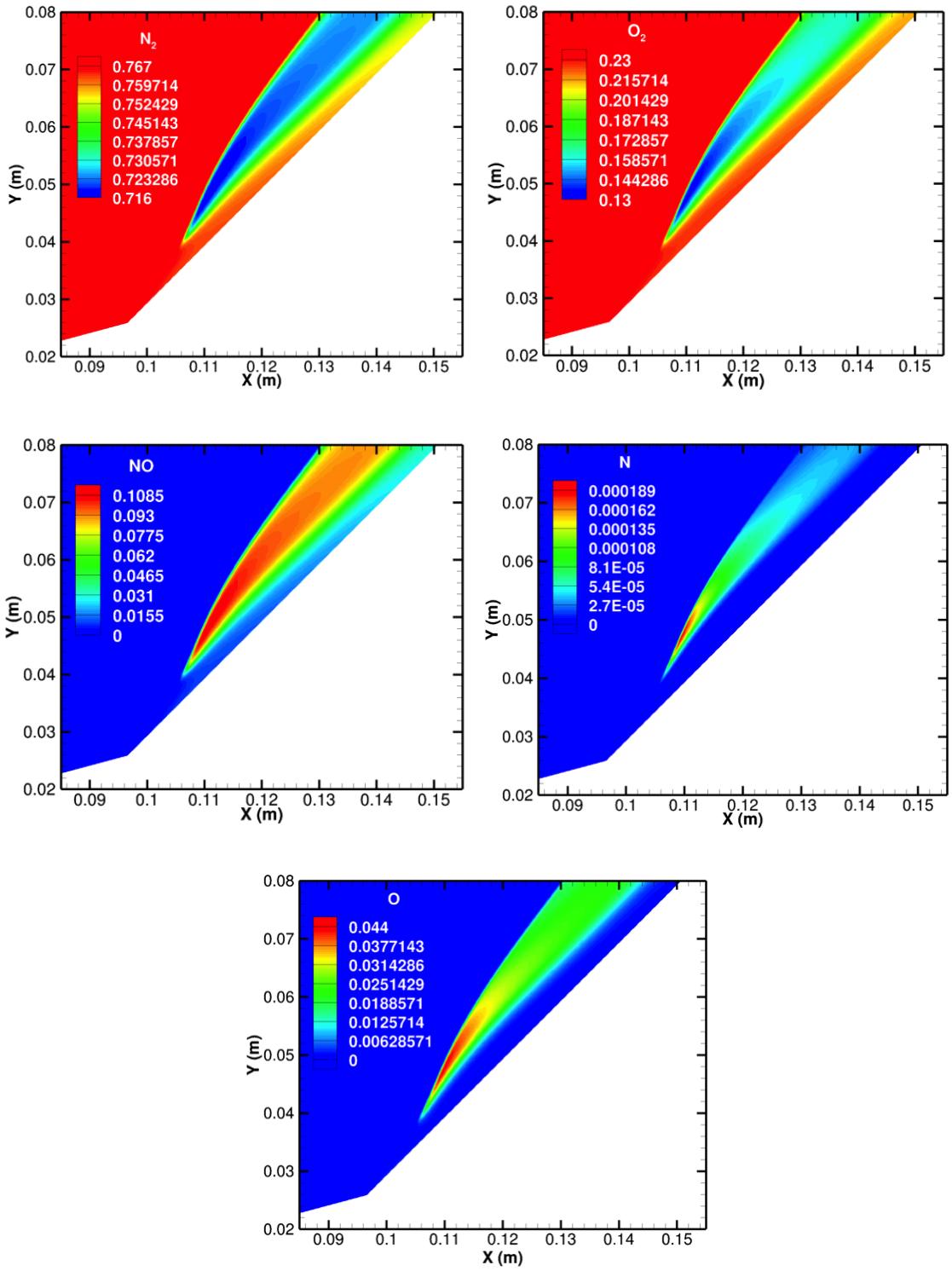

FIGURE 5.19. Mass fraction contours using a two temperature gas model for a Double Wedge: θ_1 = 15 and θ_2 = 45 in Mach 11 air flow

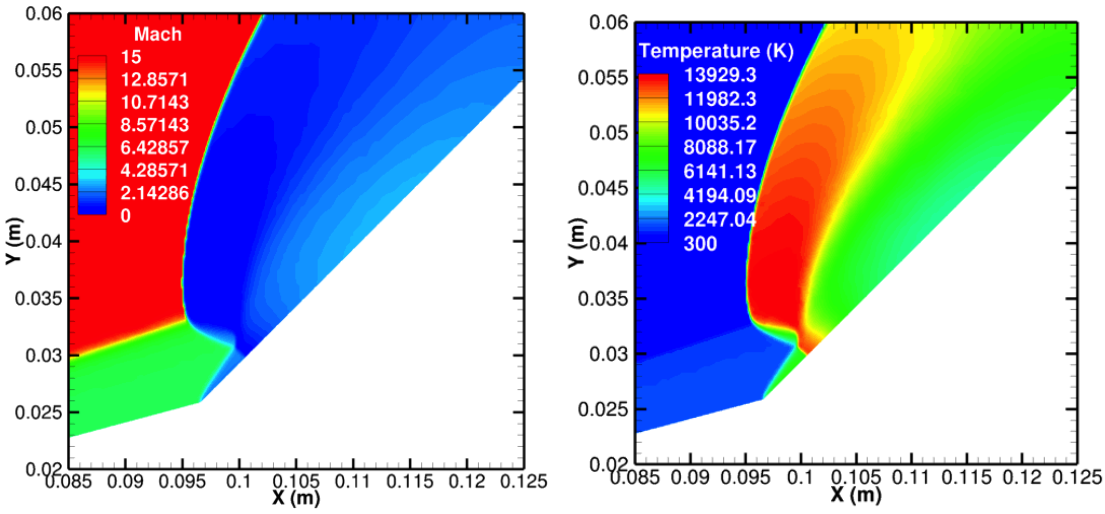

FIGURE 5.20. Mach and temperature contours using a calorically perfect gas model for a Double Wedge: θ_1 = 15 and θ_2 = 45 in Mach 15 air flow

An increase in Mach number to M_∞ = 15 results in similar flow features as in M_∞ = 9 and M_∞ = 11 cases. The detachment distance of the shock structure is expectedly lower, and peak translational temperatures reach 13000 K with calorically perfect gas (CPG) assumptions. It is interesting to note that while the peak translational temperature increases by > 100% between Mach 9 and 15 CPG cases, the one-temperature model results show a 10% increase in translational temperature. Consequently, type V interactions are more sensitive to the freestream Mach number. The dissociation at M_∞ = 15 using chemical non-equilibrium results in a 410% increase in atomic nitrogen. While peak atomic oxygen contours remain unaltered across the Mach numbers tested for chemical non-equilibrium, the greater dissociation seen at M_∞ = 15 over large regions in the post-shock interaction region indicates a weakening of the contact discontinuity.

5.3.2 Effect of second wedge angle

The second set of studies with the double wedge configuration examined the variation of the second wedge angle on the shock interaction patterns. At a freestream Mach number of 11, in addition to the $\theta_2 = 45^0$ case undertaken, two additional sets of computations with $\theta_2 = 46.3^0$ and $\theta_2 = 48^0$ were made for all the three internal energy modeling cases. It is interesting to note that calorically perfect gas simulations show significantly different shock

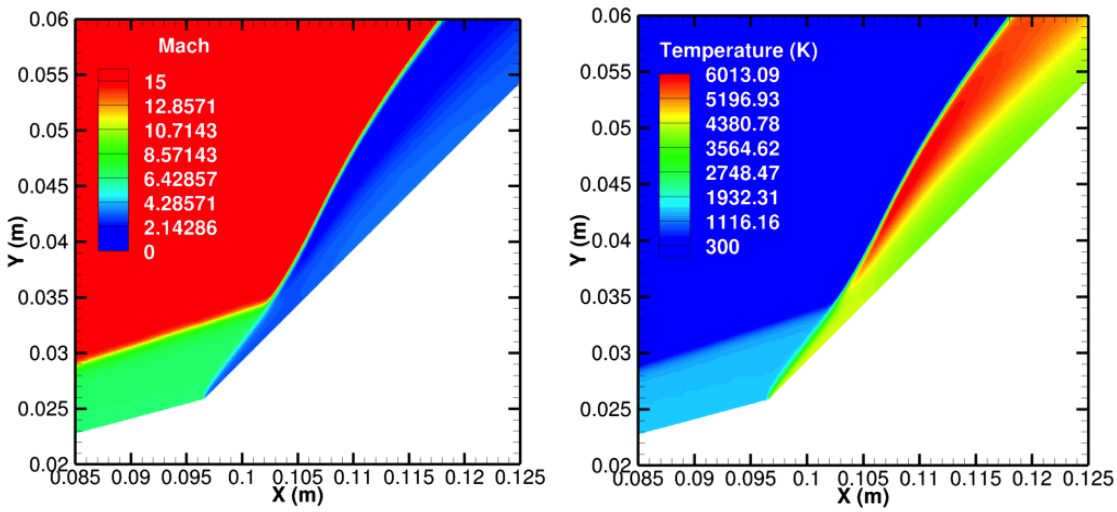

FIGURE 5.21. Mach and temperature contours using a one temperature gas model for a Double Wedge: θ_1 = 15 and θ_2 = 45 in Mach 15 air flow

interaction patterns when θ_2 is varied. The shock TR in the seven shock pattern, becomes a stronger one with increasing θ_2, and the impinging shock at the second wedge, BT, intersects PT at greater deflections. At the higher θ_2 angles, TR is almost a normal shock, resulting in yet another shock intersecting shock PS at the outer edge. The normalized surface pressure distributions for CPG simulations (figure 5.27) indicate these differences when the second wedge angle is increased to 48^0 from 46.3^0. The second pressure jump or pressure spike that is exhibited at 45^0 is displaced by a marginal degree closer to the compression corner. However, this continued displacement towards the compression corner with the increase in second wedge angle coalesces the two pressure jumps in to a singular spike of much lower intensity. The reduction in peak pressure is in excess of 33% when $\theta_2 = 48^0$.

The non-equilibrium results continue to demonstrate the second-order effect of including thermal non-equilibrium. However, for chemical and thermo-chemical non-equilibrium, a greater curvature of shock PS is seen at $\theta_2 = 48^0$. The peak surface pressure distributions for chemical non-equilibrium (figure 5.28) indicate a slight displacement in normalized pressures towards the impinging shock at the second wedge with increasing wedge (second) angle. The absence of a second pressure spike indicates a type VI interaction to be present and the peak pressures demonstrate an inverse trend (with θ_2) compared to those exhibited during a type V interaction. The surface distributions with thermo-chemical modeling

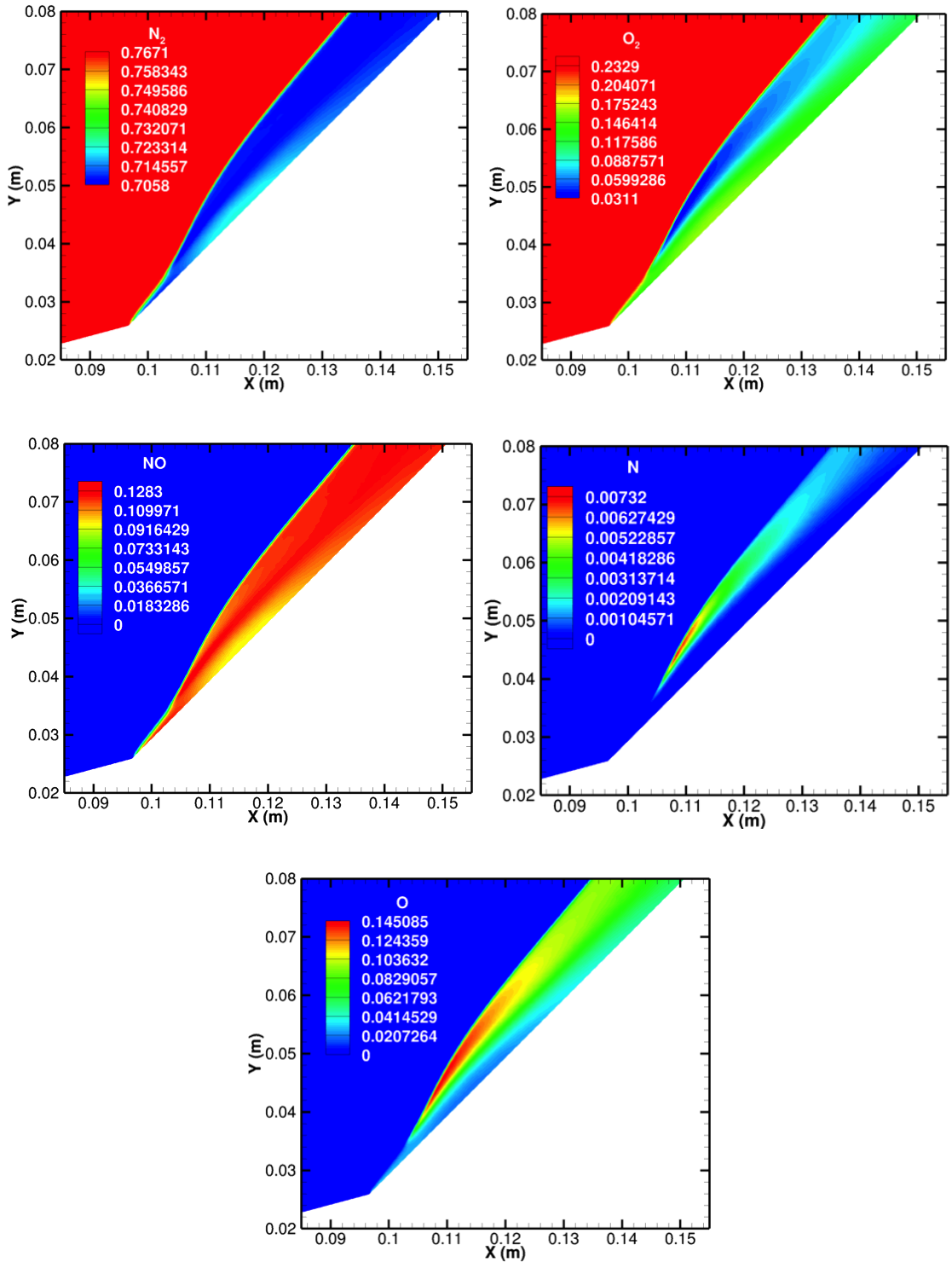

FIGURE 5.22. Mass fraction contours using a one temperature gas model for a Double Wedge: θ_1 = 15 and θ_2 = 45 in Mach 15 air flow

(figure 5.29) also closely follow the trends exhibited with chemical non-equilibrium. The non-equilibrium results do not display any transition between type VI - V upon varying

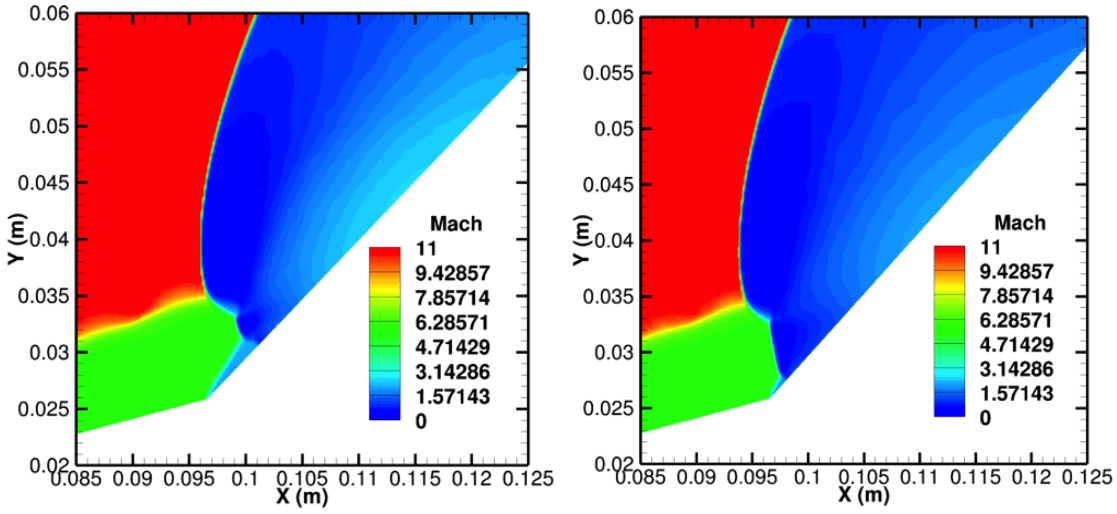

FIGURE 5.23. Mach Contours in NASCART-GT for a Double Wedge using a calorically perfect gas assumptions for θ_2 = 46.3 (left) and θ_2 = 48 (right): θ_1 = 15 and M_∞ = 11

the second wedge angle. Li et al. [72] had found a transition between these second wedge angles and were claimed to be thermo-chemical non-equilibrium results. However, as stated in their work, chemical and vibrational non-equilibirum was frozen across the shock in their computations and the non-equilibrium relaxation length used in integrating the governing equations was close to the equilibrium value. These key differences between their work and the present work could have led to different surface pressure distributions. The present work demonstrates that using full-scale thermo-chemical non-equilibrium leads to type VI interactions for the entire θ_2 parameter sweep range described above.

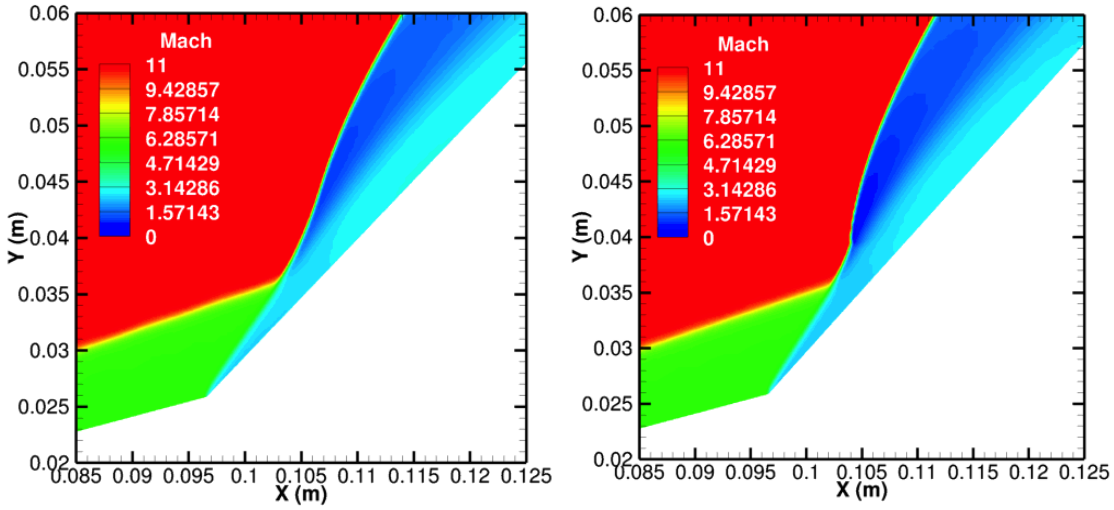

FIGURE 5.24. Mach Contours in NASCART-GT for a Double Wedge using chemical non-equilibrium for θ_2 = 46.3 (left) and θ_2 = 48 (right) : θ_1 = 15 and M_∞ = 11

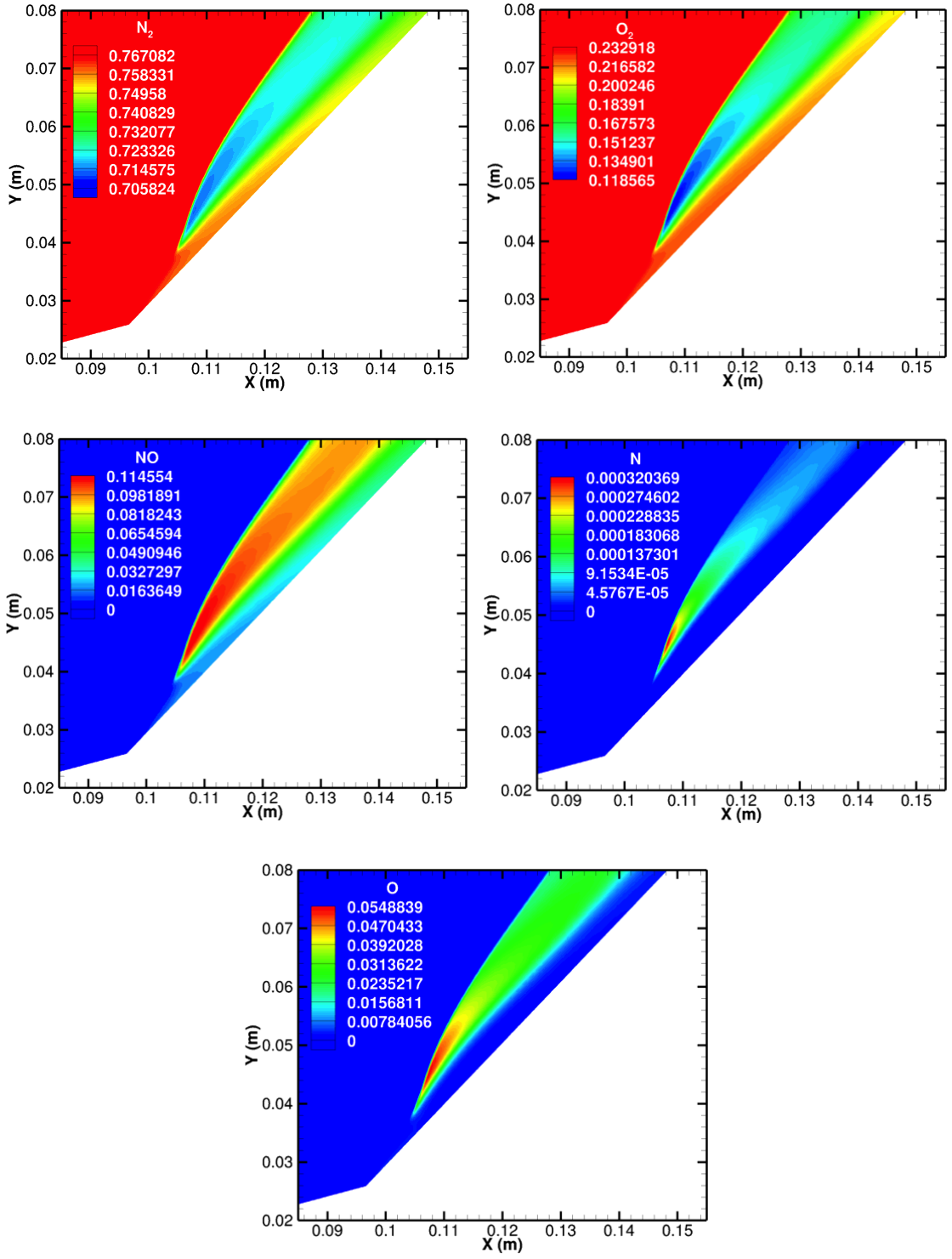

FIGURE 5.25. Mass fraction contours using a one temperature gas model for a Double Wedge: θ_1 = 15 and θ_2 = 46.3 in Mach 11 air flow

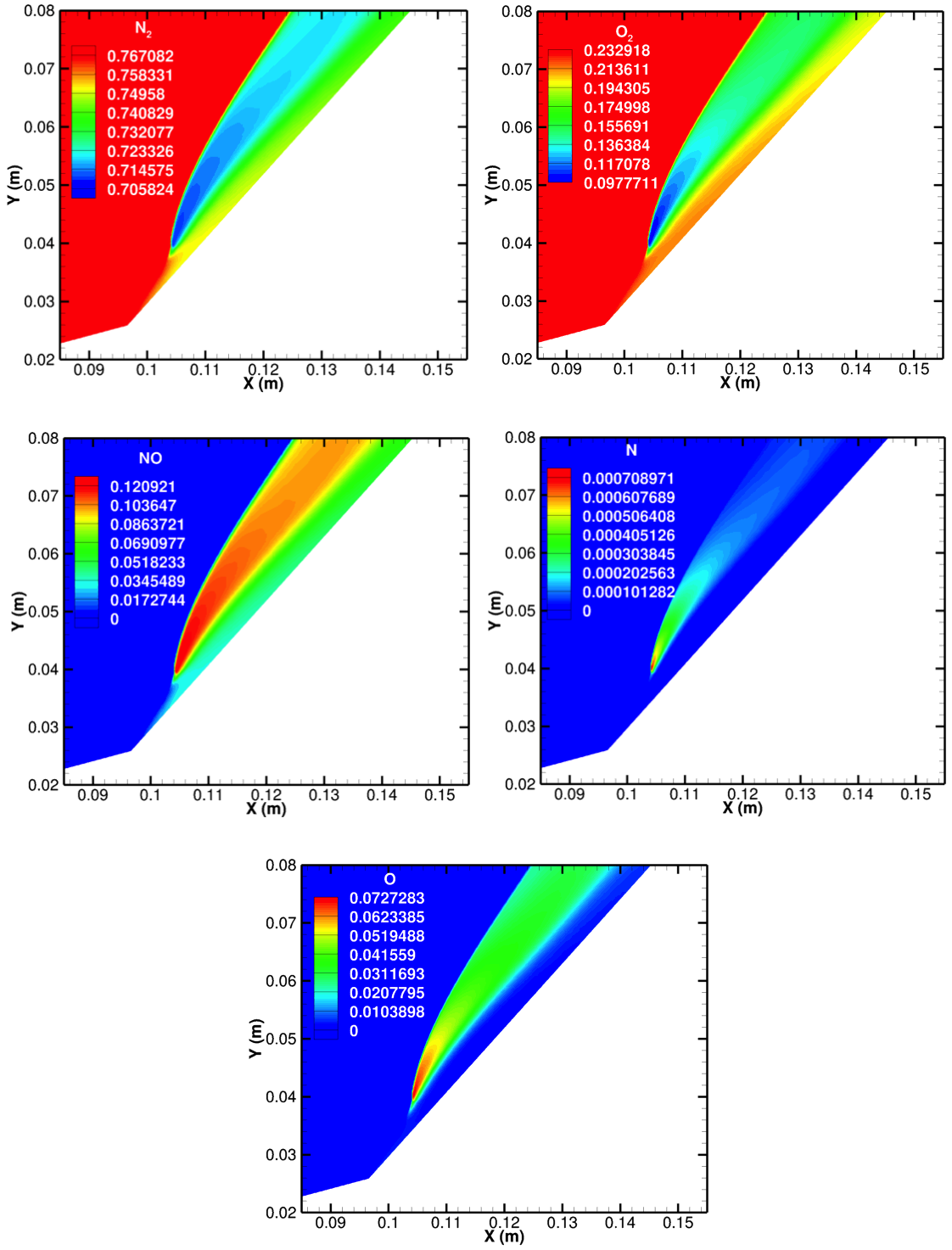

FIGURE 5.26. Mass fraction contours using a one temperature gas model for a Double Wedge: θ_1 = 15 and θ_2 = 48 in Mach 11 air flow

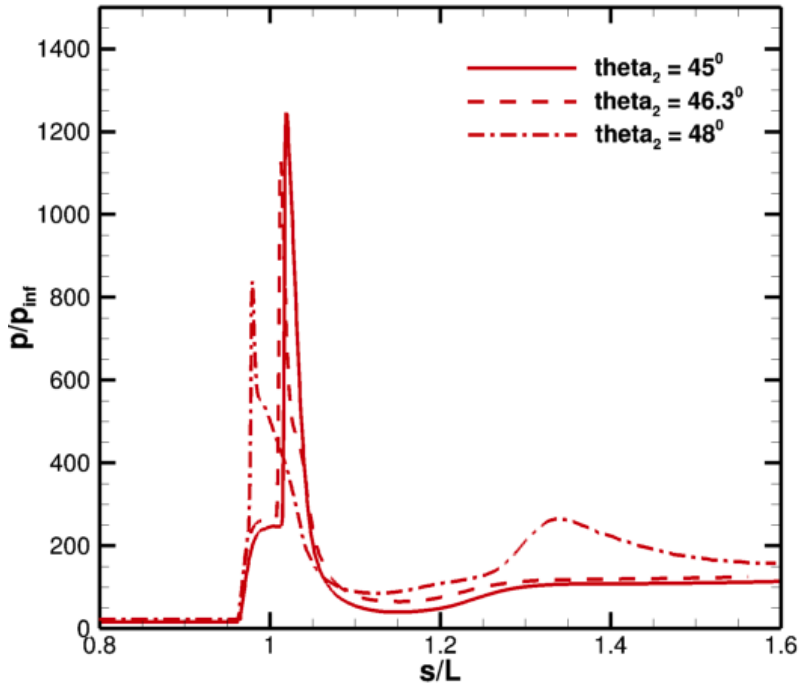

FIGURE 5.27. Surface pressure distributions along the double wedge using calorically perfect gas assumptions: θ_1 = 15 and Mach 11 air flow

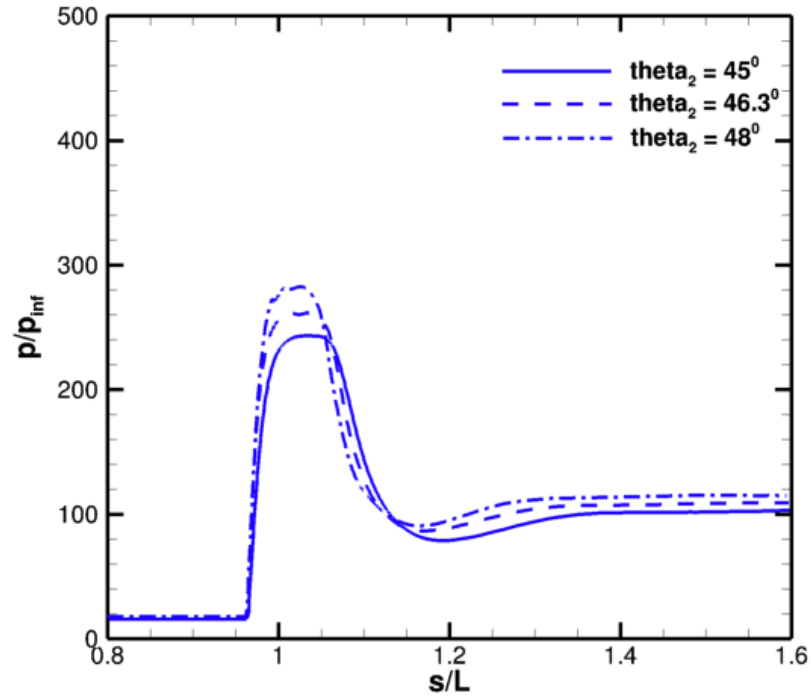

FIGURE 5.28. Surface pressure distributions along the double wedge using chemical nonequilibrium: θ_1 = 15 and Mach 11 air flow

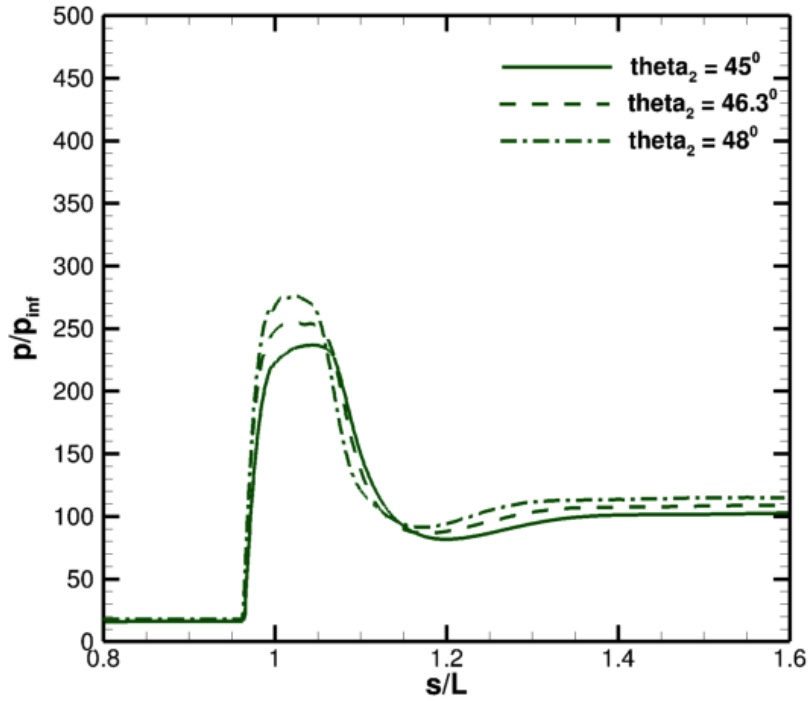

FIGURE 5.29. Surface pressure distributions along the double wedge using thermo-chemical non-equilibrium: θ_1 = 15 and Mach 11 air flow

5.4 Cylinder flow

The inviscid thermochemical nonequilibrium capabilities of the flow solver were validated for a blunt body by using a cylinder of radius 0.05 m. This validation test case, used originally by Tu [46], and later by Lee [49], served to verify other numerical data [76]. Tu's work used this case to validate chemical and thermo-chemical non-equilibrium (two temperature) results. The freestream conditions used for this case are shown in the Table below.

The AUSMPW+ scheme was used to compute the results presented here. In order

TABLE 5.1. Freestream conditions used for the cylinder test case

Parameter	**Freestream value**
Mach number	12.7
Pressure	90 Pa
Density	0.0016 kg/m^3
Temperature	195.96 K

to capture the sharp gradients, solution adaptation was carried out every 100 iterations. The adaptation was based on gradients of velocity divergence and species concentrations. The CFL number was maintained at 0.4 throughout the flow simulation. The air chemistry model used was the 5-species, 17-reaction model developed by Park [64]. The surface was set to an adiabatic wall condition.

5.4.1 Two temperature model

The primary goal with this cylinder test case was to validate the two-temperature thermochemical model implemented in NASCART-GT. As can be seen in figures 5.31 - 5.32, and using 256 cells along the length of the body, a spatial first order solution was adequate to capture the gradients that agree well with those obtained using DPLR and verified by Lee. The stagnation line results (figures 5.31 - 5.32) indicate that the shock layer thickness is similar (within 6.25%) for the present results relative to DPLR. The adaptive mesh refinement used in the present work helps obtain a sharp shock front, while perhaps insufficient grid tailoring iterations for the body fitted mesh used to generate the DPLR data results in a coarser shock front. The shock stand-off distance and shock wave shape

agree well with those of literature data [49], [46], [76]. The chemical non-equilibrium results obtained by Tu were within 3.7% of the loosely-coupled implicit solutions obtained by Yahia [76]. Similar agreement was obtained for thermo-chemical non-equilibrium results using a two-temperature model. Lee's verification of these results and validation using DPLR had resulted in similar shock stand-off distances and values of thermodynamic quantities. In addition, comparisons made of shock stand-off distance to classical experimental data reported by Liepmann and Roshko [77], and the analytical estimates made by Billing [78], provide the expected agreement on the asymptotic trend at higher Mach numbers (see figure 5.33). Billig's analytical estimate was made by assuming the detached shock wave to be "a hyperbola that is asymptotic to the freestream Mach angle" [78], and the shock stand-off was mathematically defined in the following form for cylinders:

$$\frac{\delta}{D} = 0.193 * exp\left(\frac{4.67}{M^2}\right) \tag{5.2}$$

Despite the consideration of equilibrium between translational and rotational modes, and the vibrational and electronic modes in the present work, as against an equilibrium assumption between the translational, rotational and electronic modes in DPLR, it was seen that the variations in the contour (figures 5.34 - 5.42) and stagnation line plots were minimal. There were some variations observed in stagnation line temperatures in literature. Higher surface temperatures were observed in Tu's [46] work with the vibrational temperature overshooting the translational temperature at approximately 0.01 m from the surface. Lee's verification of the results showed different surface temperatures and overshoot characteristics. Through the process of obtaining grid independent results in the present work, it was seen that the variations in the detachment region were due to insufficient spatial resolution of gradients. With the spatial resolution chosen here, the vibrational temperature overshoot point and surface temperature agree well with those of DPLR documented in Lee's work [49].

The contour plots (figures 5.34 - 5.42) indicate close agreement with DPLR results. The vibrational temperature contours show some variations above the body and near the exit plane where the mixture averaged vibrational temperature is not considered to be in equi-

librium with the rotational temperature in the present work. In addition to the differences in non-equilibrium modeling, differences in grid resolution between DPLR and NASCART-GT may also be a contributing factor. The shock front is rather coarse in the DPLR results and solution adaptation based on species gradients is absent in them. The vibrational temperatures are very sensitive to the species gradients, and these differences are manifested in the corresponding contour plots. Following the validation of these results, as described in the following sections, other thermo-chemical models implemented in the present work were also tested for this blunt body case.

5.4.2 Multi-vibrational, single translational temperature model

The multi-vibrational temperature contour results (see figures 5.43 - 5.46) show the variations for each diatomic species using the full 7-species air model proposed by Park. The vibrational temperature contours for O_2 qualitatively agree with those obtained using a two-temperature model in DPLR . The peak vibrational temperatures for N_2 remain close to the surface, while those for O_2 and NO are displaced from the surface. Furthermore, it is seen that the shock stand-off distance for the multi-vibrational, single translational temperature model is withing 7% of the corresponding results obtained using a two-temperature model (figure 5.47). The two temperature, 7-species air model over-predicts the surface translational and vibrational temperatures by ~400 K compared to a multi-vibrational temperature formulation. As can be seen in figure 5.48, thermal equilibration occurs in accordance to the species with the most efficient transfer of energy, with NO and NO^+ achieving the highest rate to thermal equilibration. This finding is in agreement with spectroscopic vibrational temperatures reported in literature [79].

5.4.3 Multi-vibrational, two translational temperature model

While the studies thus far indicate the variations in results for thermo-chemical models using a single translational model, it was of interest to investigate the effects of using multi-temperature models with environments involving an electron temperature indicative of any weakly ionized plasma present. For such purposes, a 7 species air model was used again with the electron energy conservation equation coupled to the remaining gas dynamic, chemical

and vibrational energy conservation equations. In addition to the usual trends observed with the 5 species multi-vibrational temperature air model, a 7 species air model with the electron energy balance equation provided a rapidly equilibrating NO+ vibrational temperature and an electron temperature that equilibrates at a relatively slow rate. The absence of boundary layer considerations leads to a larger rise in electron temperature near the surface than would otherwise be observed.

Furthermore, the NO^+ mole fraction contours (figure 5.49) indicate the confinement of higher mass fractions to a smaller region near the stagnation region than would otherwise be obtained in the absence of an electron energy conservation equation. The plasma pressure contours (figure 5.50) show peak values in regions of high electron concentrations and total pressure of the flow field. The low plasma pressure seen is in congruence with the weak ionization that can be expected at these conditions. The shock stand-off distance showed a $< 2\%$ difference in comparison with the results not utilizing the electron energy balance equation. These results indicate that for the degree of nonequilibrium present for the case under consideration, while multi-temperature models provide for additional useful data, such as equilibrium temperatures for the various modes computed, constituent variations in species mass fractions, etc, they do not cause significant variations in overall gas dynamic characteristics, such as peak translational temperature, pressure, and shock stand-off distances. They, however, do result in non-negligible variations in chemistry in the detachment region compared to the widely used two-temperature or $\sqrt{TT_v}$ model. Nonetheless, this case captures the complex flow fields typically studied for hypersonic flows and demonstrates the ability of the various implemented multi-temperature models to adequately capture the underlying flow physics.

5.4.4 Sensitivity to chemical kinetics

Of all the thermo-chemical models tested for the cylinder in hypersonic flow, the largest variation in flow field characteristics was seen in considering 7 species air kinetics instead of a 5 species air model. The inclusion of charged species, NO^+ and e^-, result in $\sim 7\%$ increase in shock stand-off distance (figure 5.51-5.52). The resulting surface temperatures using a 7-species air model increases by $\sim$ 200 K at the surface relative to that obtained

by a 5-species air model (see figure 5.52). Figure 5.53 shows the far-reaching effects of dissociation in the detachment region when multi-temperature models are considered. The additional kinetics associated with a 7 species model enhances the dissociation close to the surface (figure 5.54), and can therefore be deemed to possess a greater impact for such hypersonic flow computations.

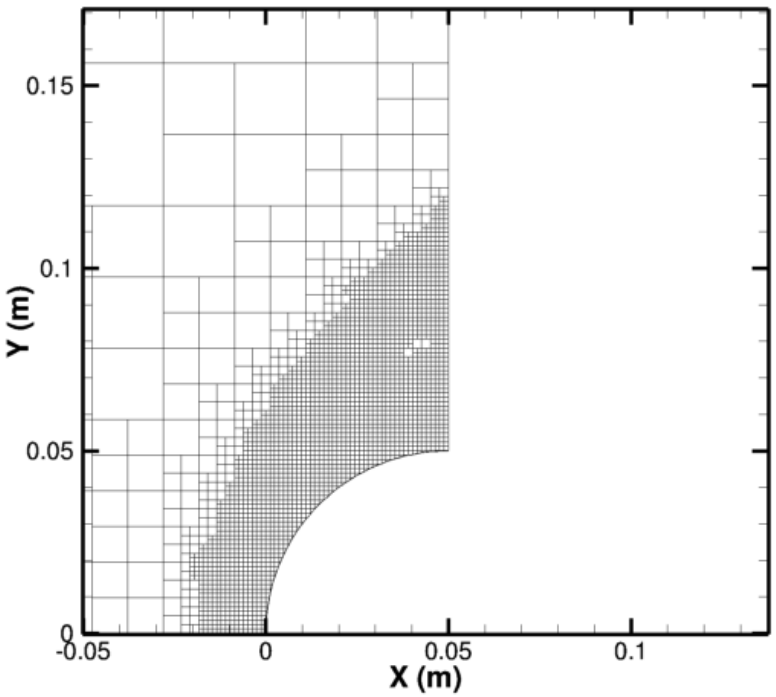

(A) Computational grid for a cylinder in Mach 12.7 air

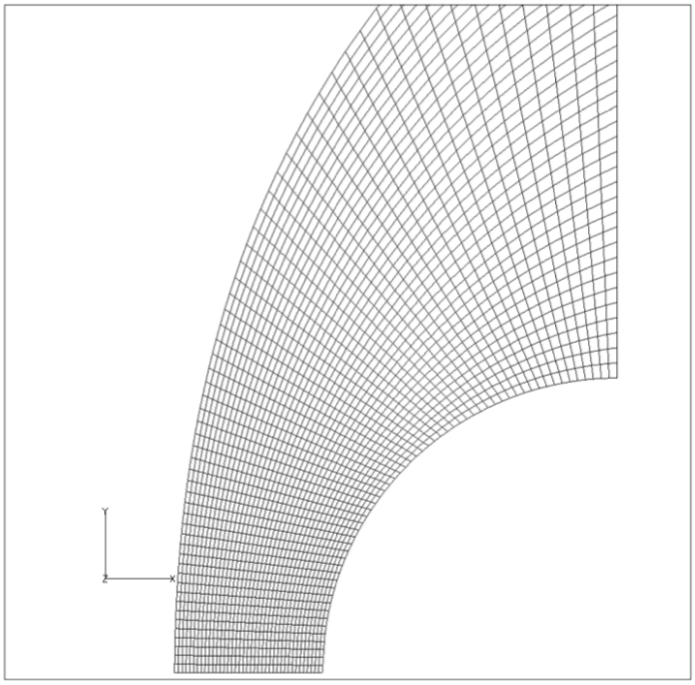

(B) DPLR Computational grid for a cylinder in Mach 12.7 air

FIGURE 5.30. NASCART-GT and DPLR Computational grid for a cylinder in Mach 12.7 air

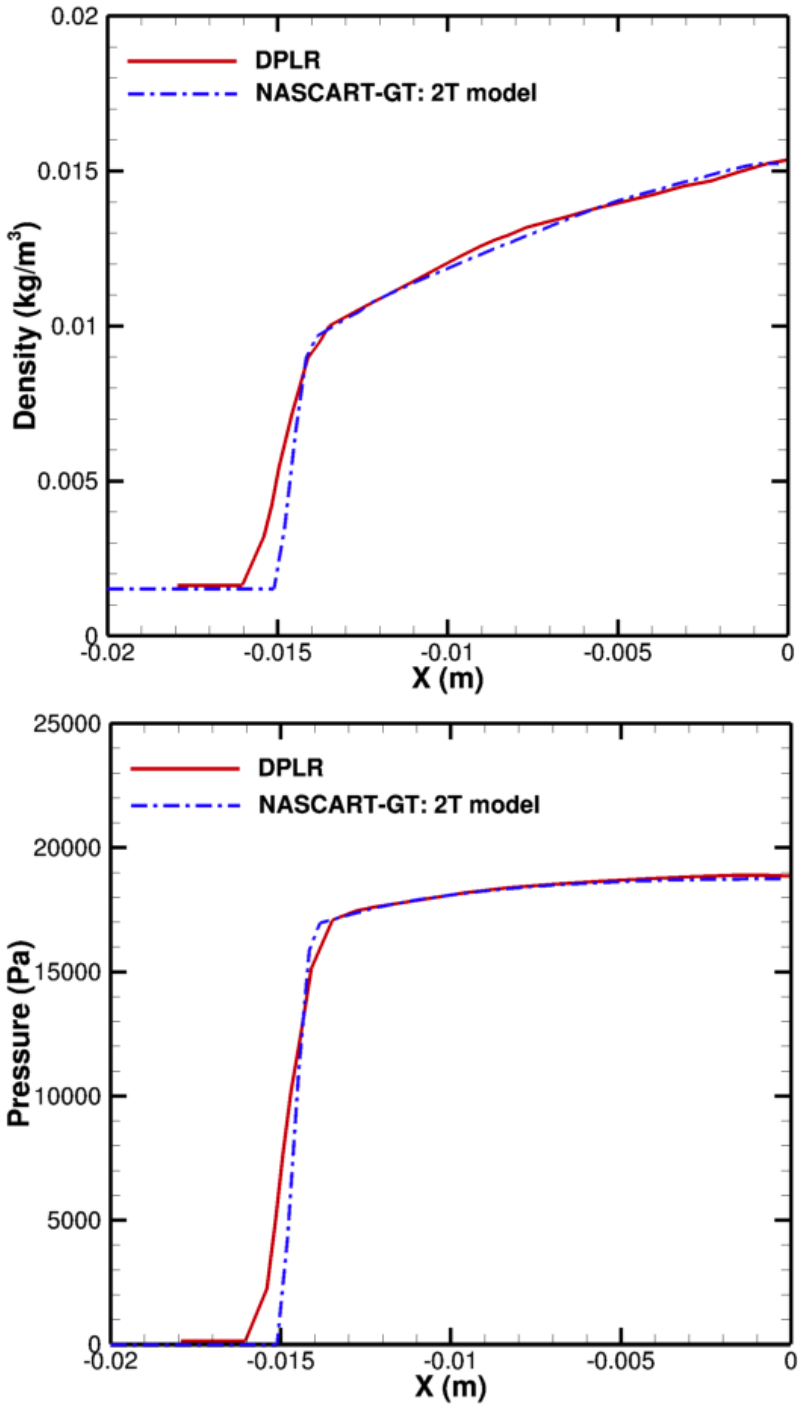

FIGURE 5.31. Comparative stagnation line density and pressure for a cylinder in a 5-species Mach 12.7 air flow between NASCART-GT and DPLR

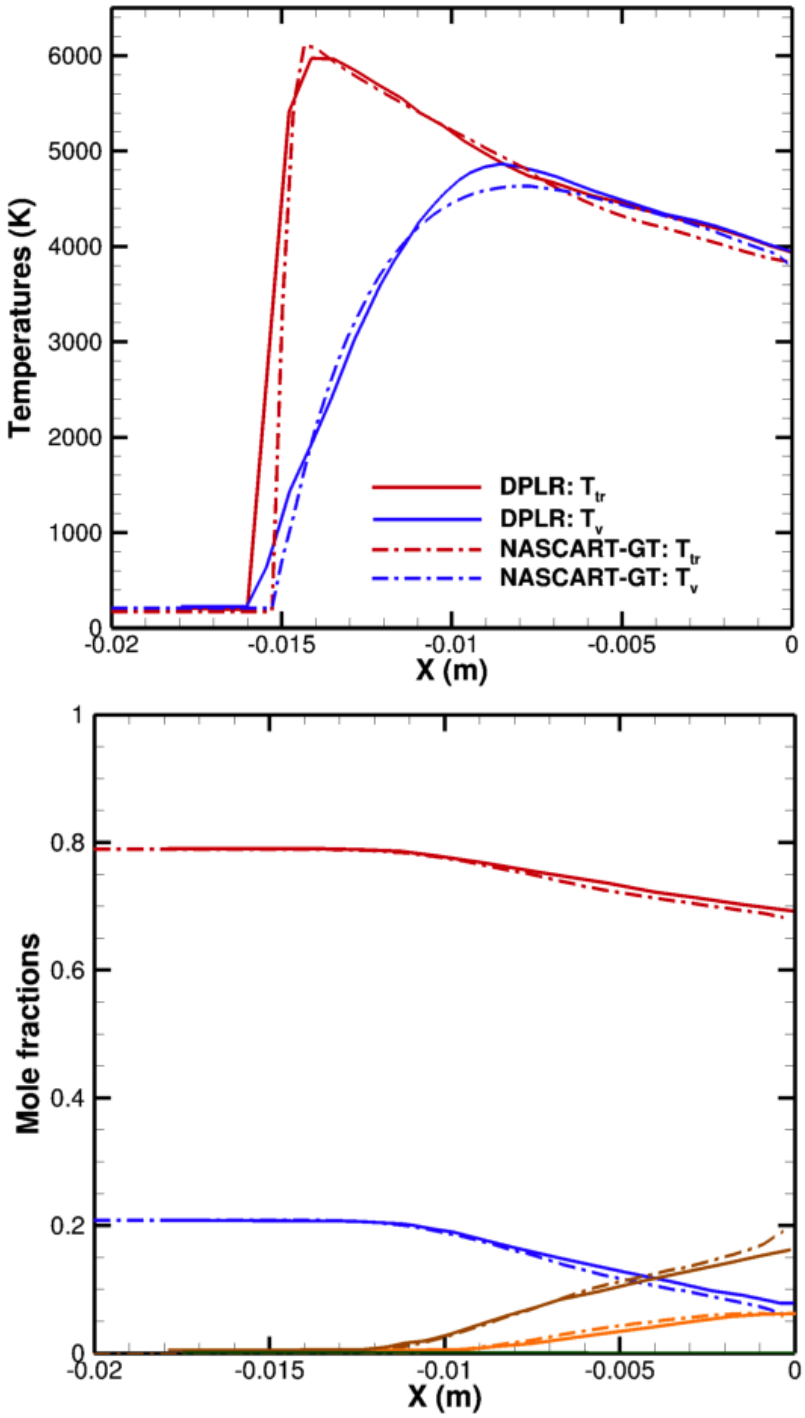

FIGURE 5.32. Comparative stagnation line temperatures and mole fractions for a cylinder in a 5-species Mach 12.7 air flow between NASCART-GT and DPLR: —— DPLR; - - - - NASCART-GT; (■: N_2 ; ■: O_2 ; ■: NO ; ■: N ; ■: O)

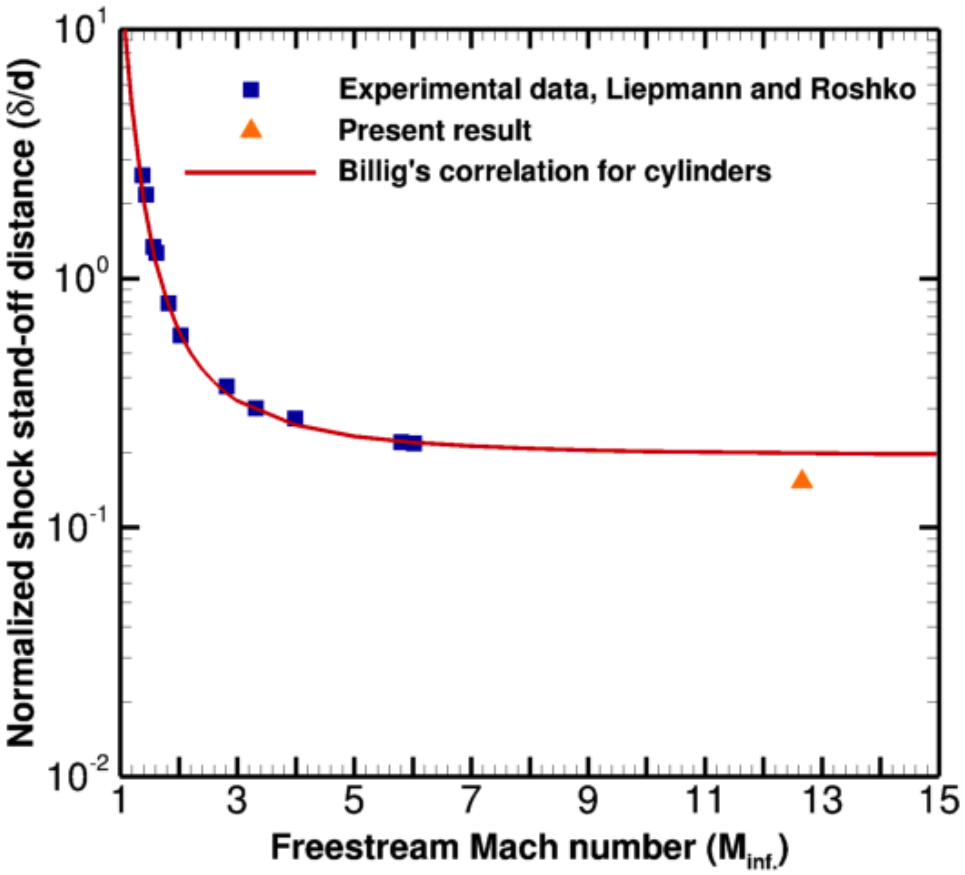

FIGURE 5.33. Comparative shock stand-off distances between experimental cold hypersonic wind tunnel data (γ = 1.4) [77], Billig's analytical estimate [78] (γ = 1.4), and present result using a two-temperature thermo-chemical model for cylinder flows

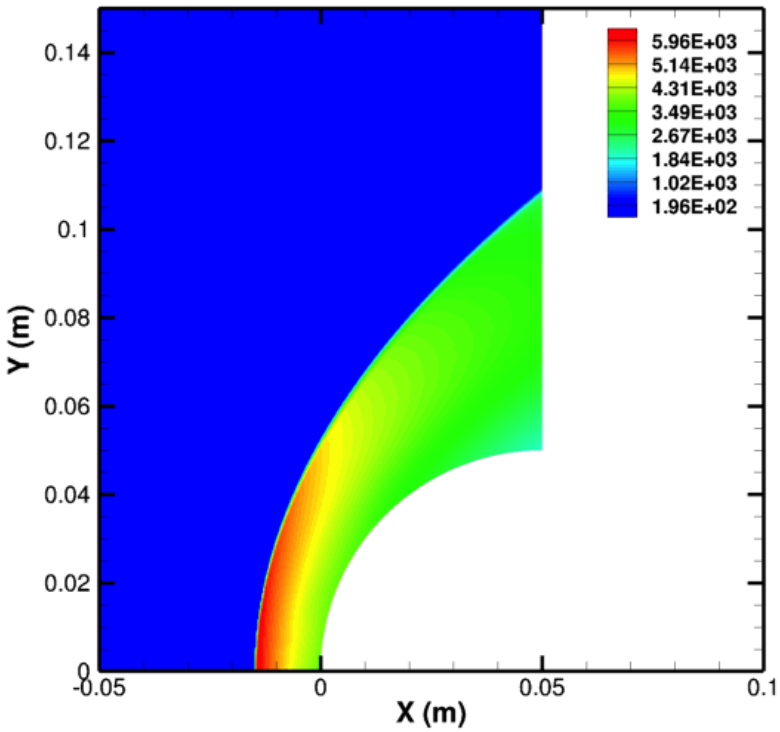

(A) Translational temperature contours for a cylinder in Mach 12.7 air

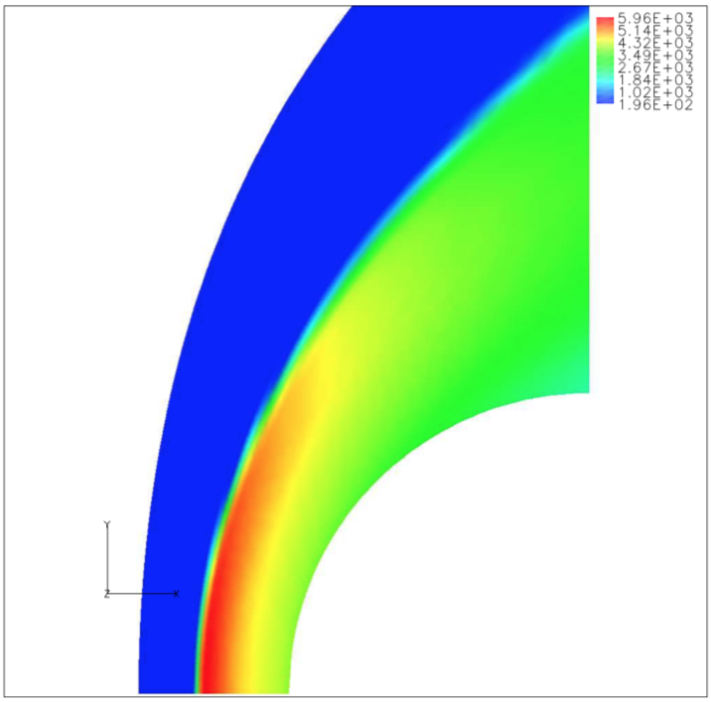

(B) DPLR Translational temperature contours for a cylinder in Mach 12.7 air

FIGURE 5.34. NASCART-GT and DPLR Translational temperature contours for a cylinder in Mach 12.7 air

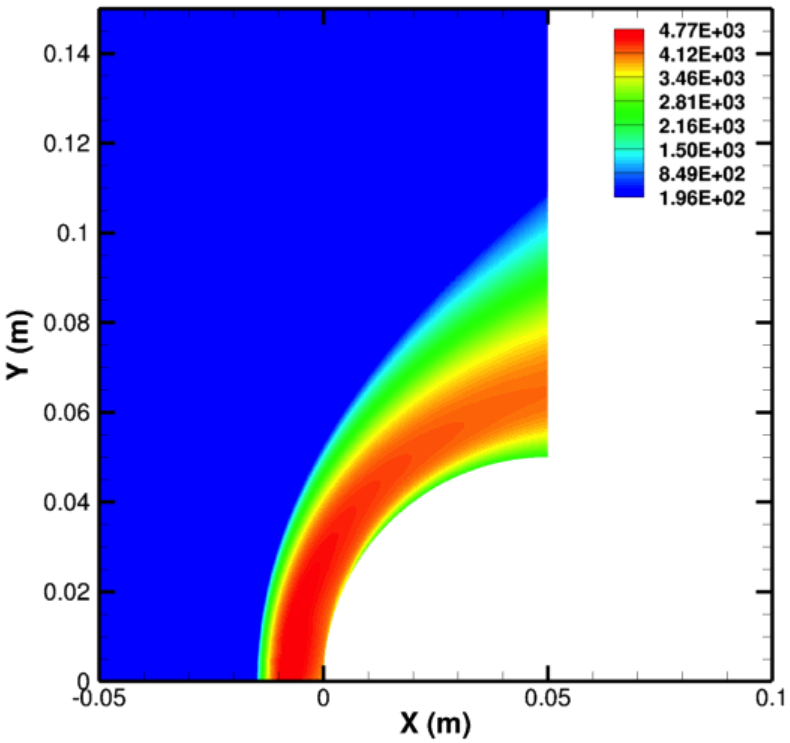

(A) Vibrational temperature contours for a cylinder in Mach 12.7 air

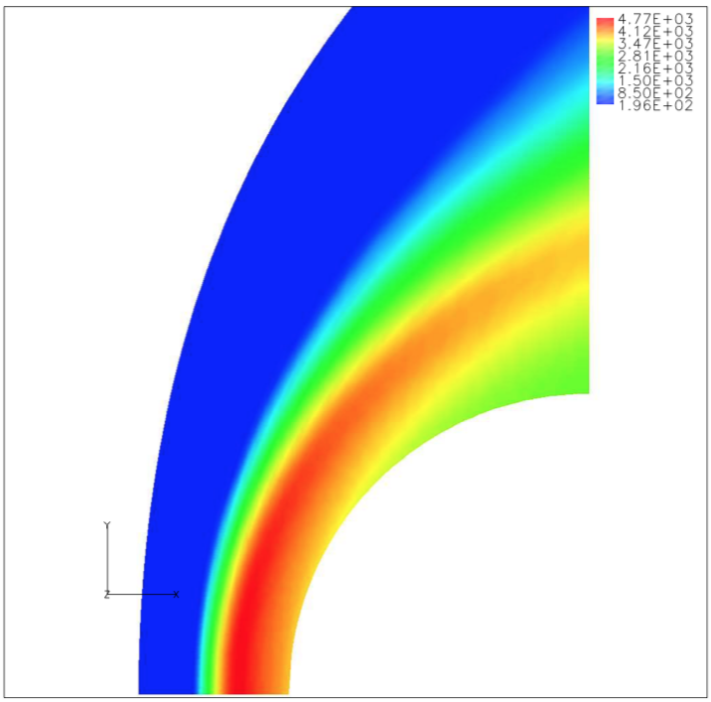

(B) DPLR Vibrational temperature contours for a cylinder in Mach 12.7 air

FIGURE 5.35. NASCART-GT and DPLR Vibrational temperature contours for a cylinder in Mach 12.7 air

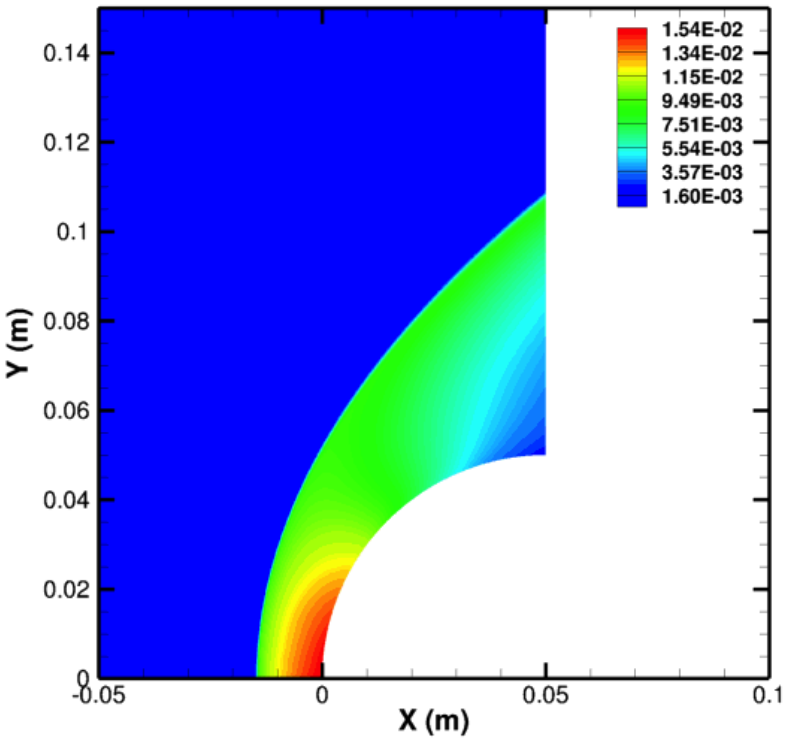

(A) Density contours for a cylinder in Mach 12.7 air

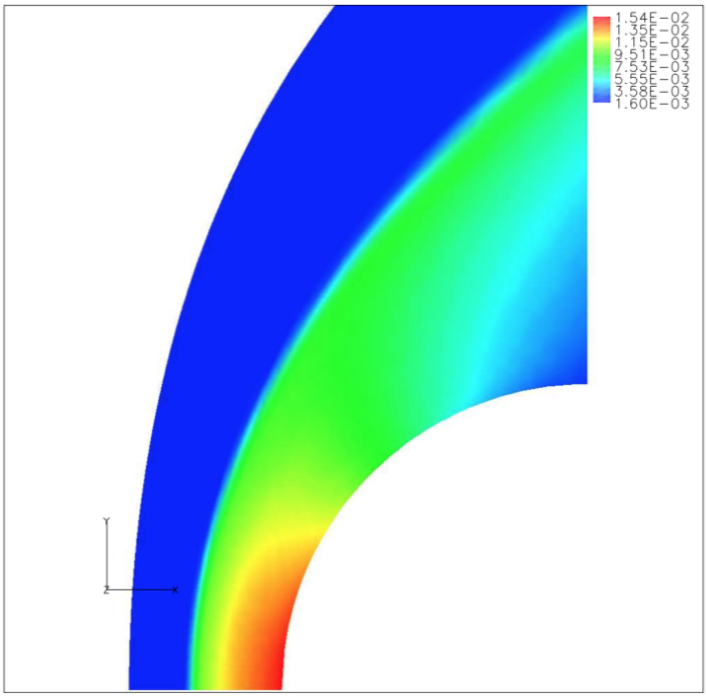

(B) DPLR Density contours for a cylinder in Mach 12.7 air

FIGURE 5.36. NASCART-GT and DPLR Density contours for a cylinder in Mach 12.7 air

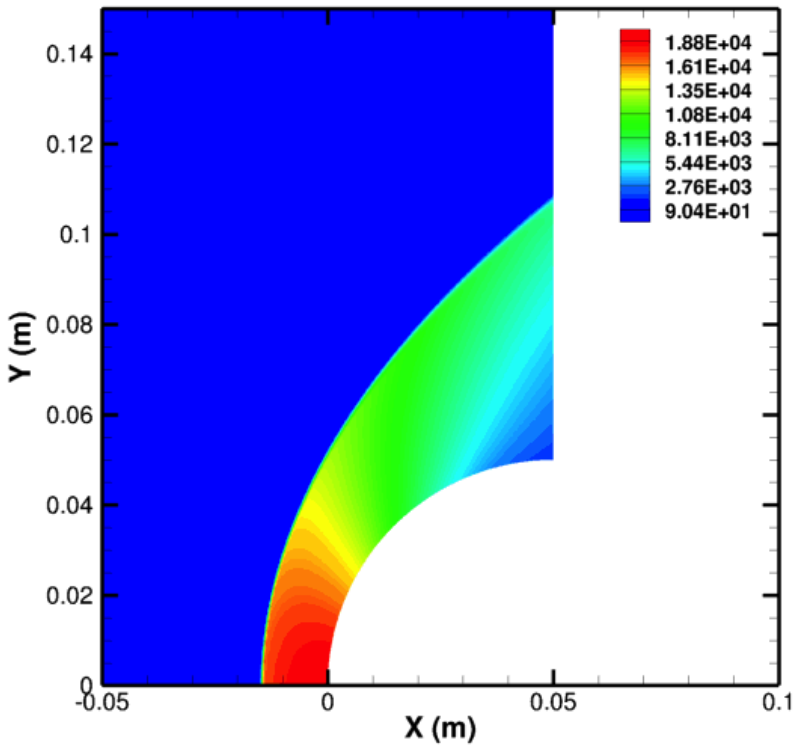

(A) Pressure contours for a cylinder in Mach 12.7 air

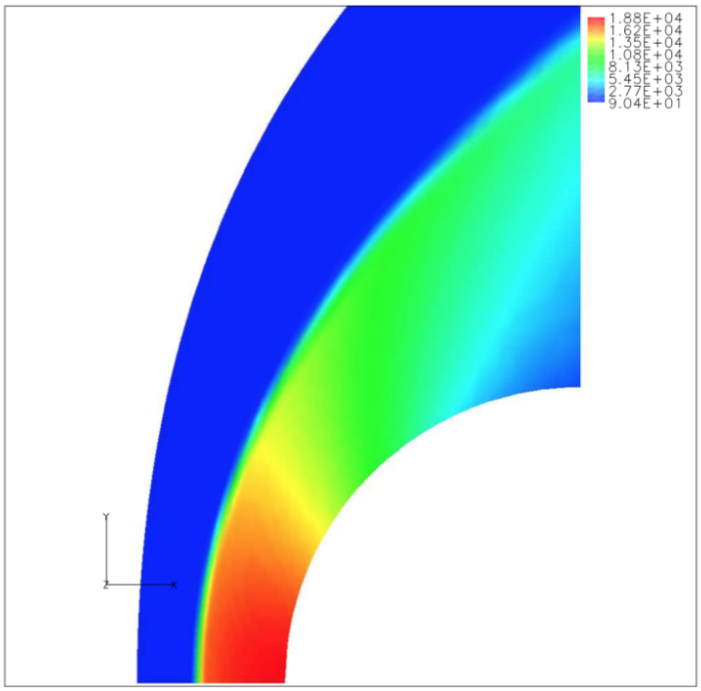

(B) DPLR Pressure contours for a cylinder in Mach 12.7 air

FIGURE 5.37. NASCART-GT and DPLR Pressure contours for a cylinder in Mach 12.7 air

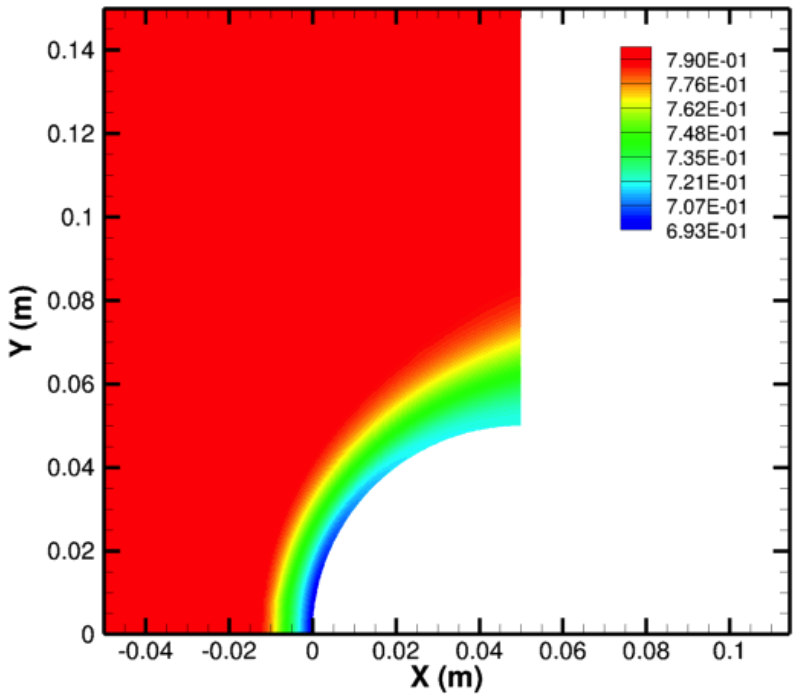

(A) N_2 mole fraction contours

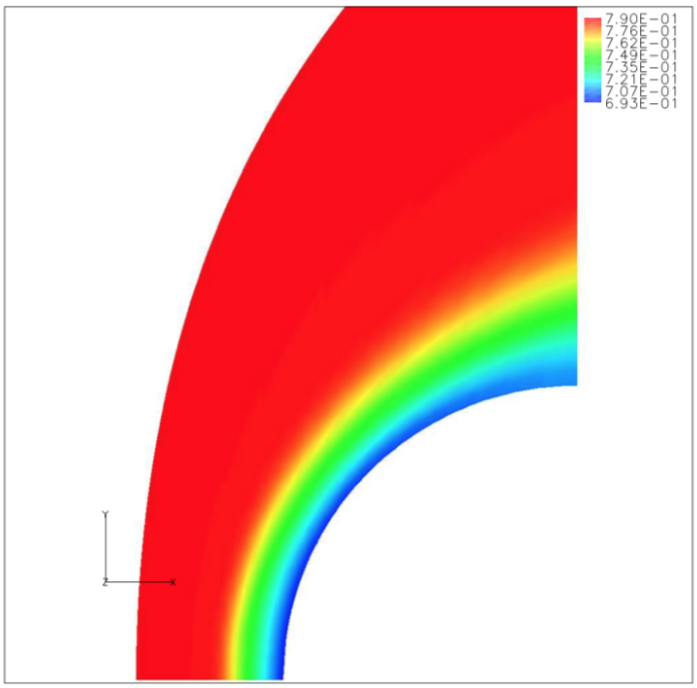

(B) DPLR N_2 mole fraction contours

FIGURE 5.38. NASCART-GT and DPLR N_2 mole fraction contours

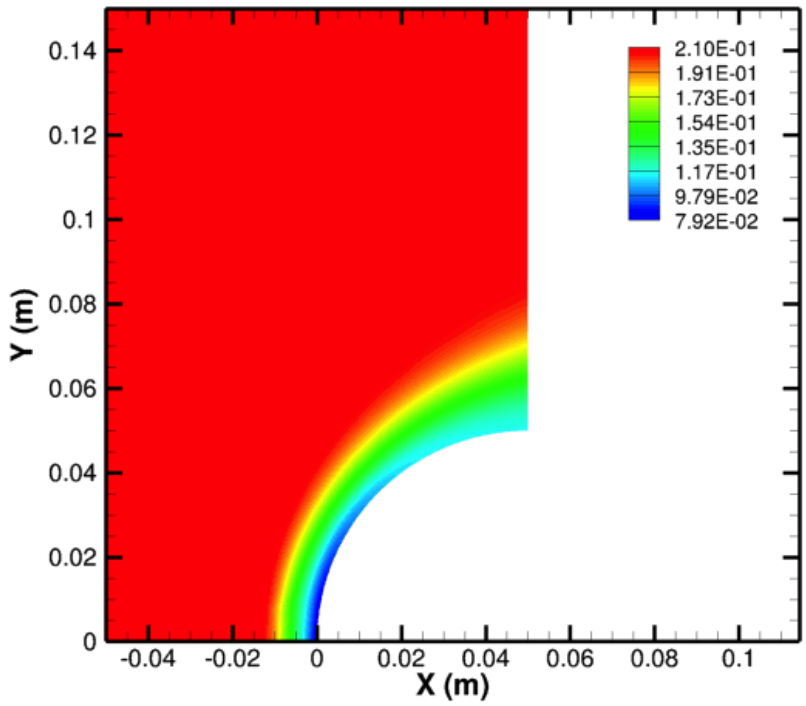

(A) O_2 mole fraction contours

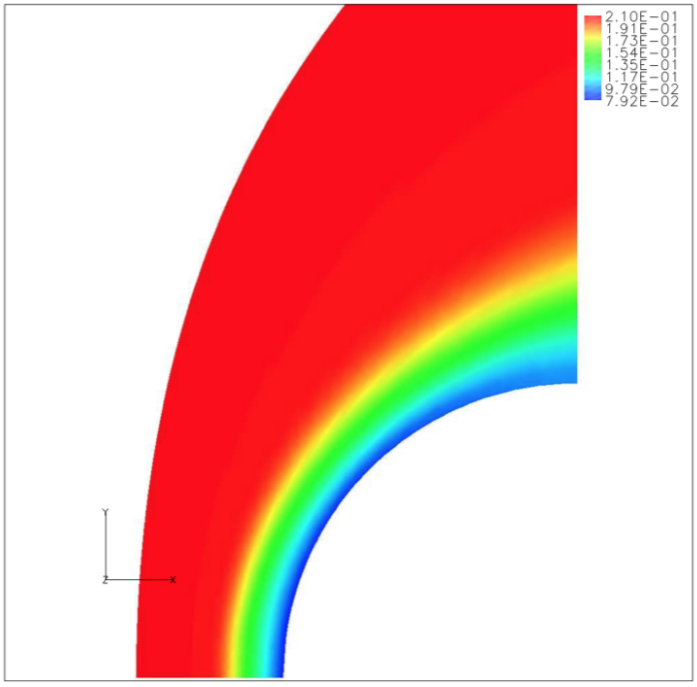

(B) DPLR O_2 mole fraction contours

FIGURE 5.39. NASCART-GT and DPLR O_2 mole fraction contours

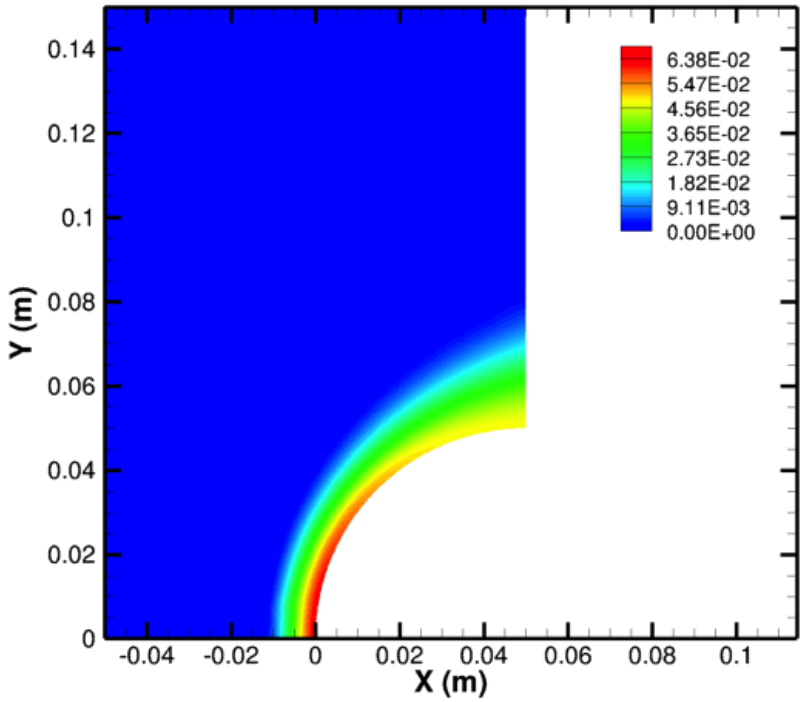

(A) NO mole fraction contours

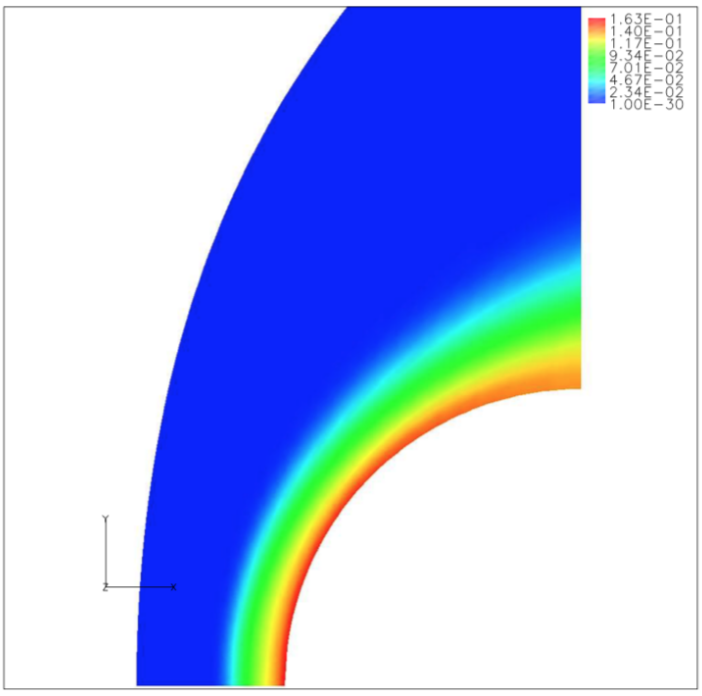

(B) DPLR NO mole fraction contours

FIGURE 5.40. NASCART-GT and DPLR NO mole fraction contours

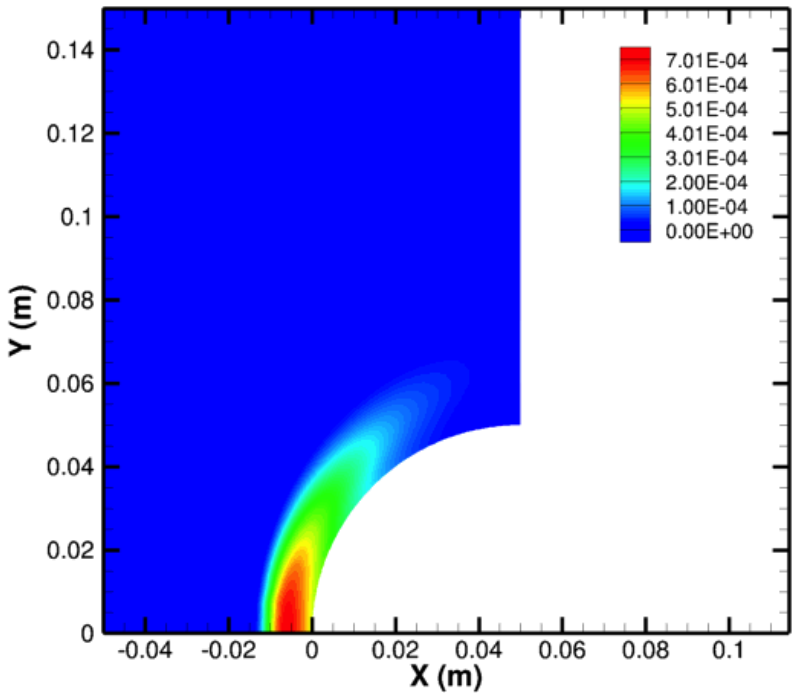

(A) N mole fraction contours

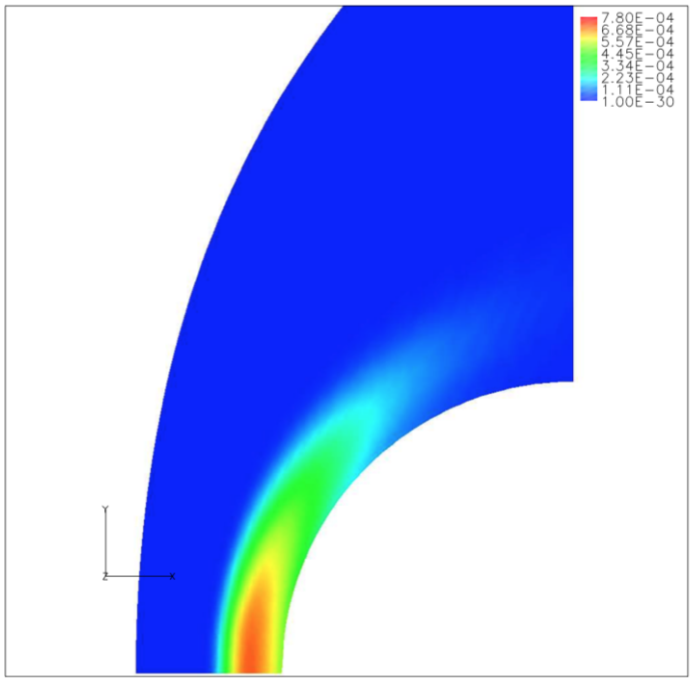

(B) DPLR N mole fraction contours

FIGURE 5.41. NASCART-GT and DPLR N mole fraction contours

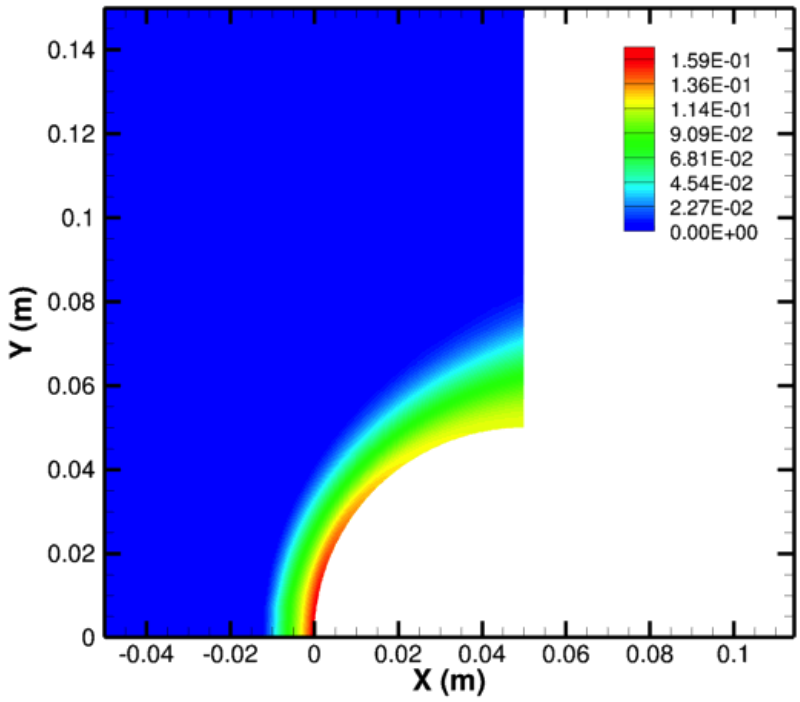

(A) O mole fraction contours

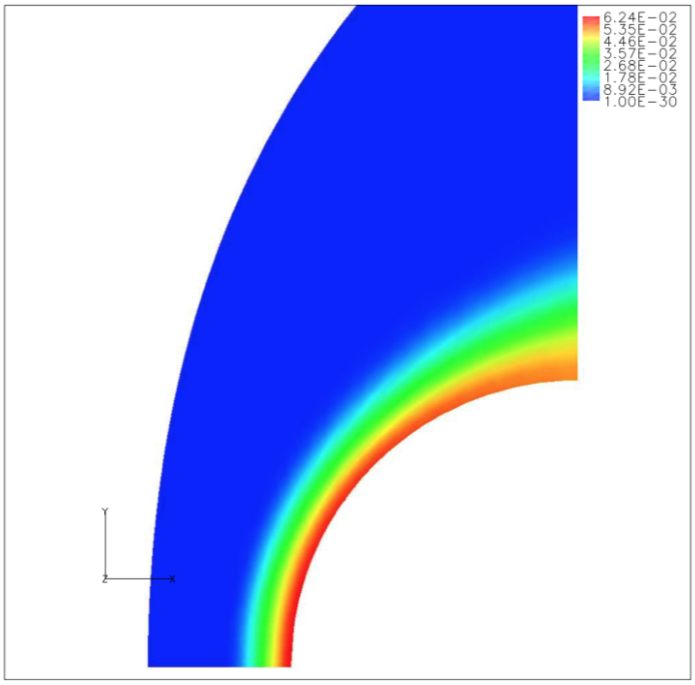

(B) DPLR O mole fraction contours

FIGURE 5.42. NASCART-GT and DPLR O mole fraction contours

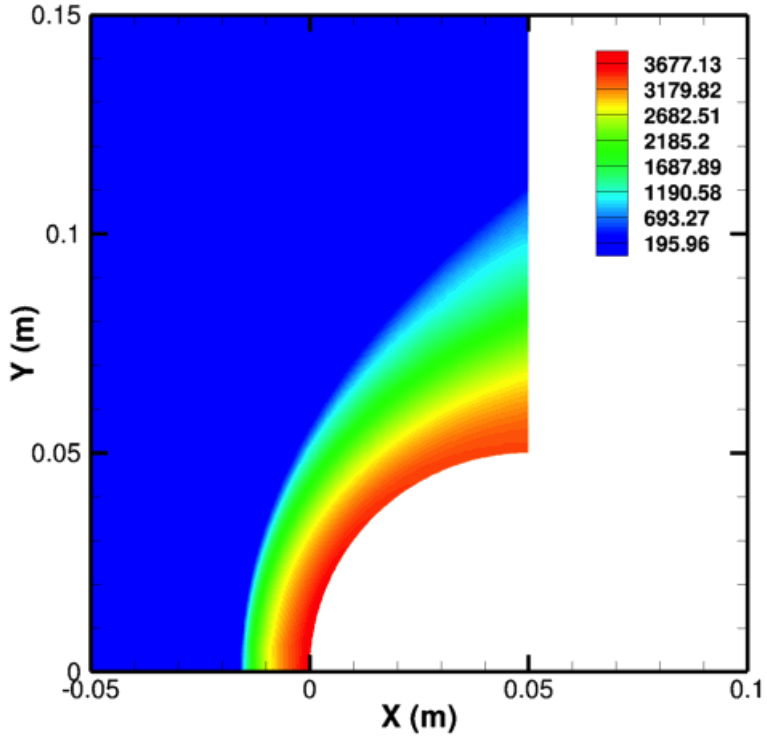

FIGURE 5.43. N_2 vibrational temperature contours using a multi-vibrational temperature formalism: A cylinder in a Mach 12.7 5-species air

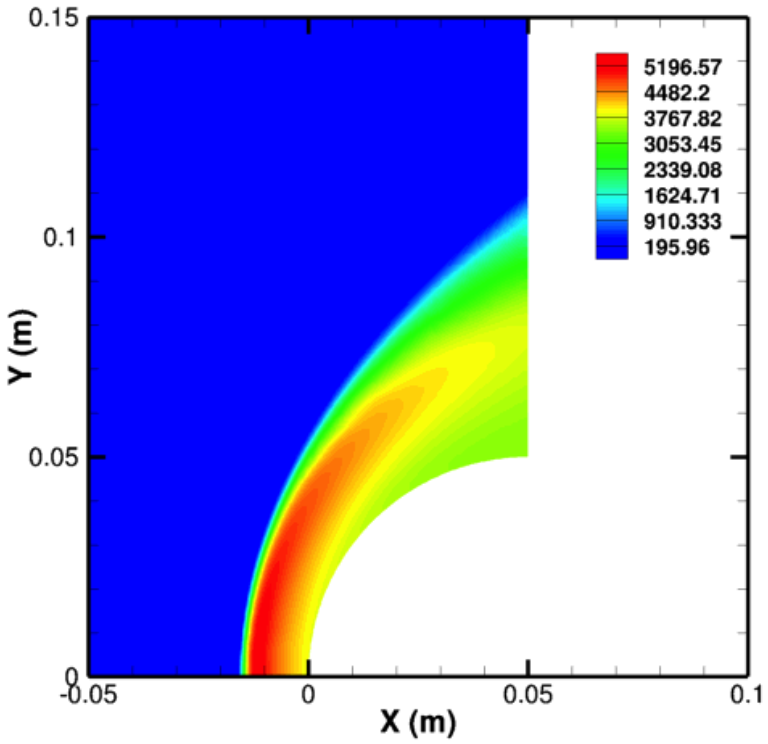

FIGURE 5.44. O_2 vibrational temperature contours using a multi-vibrational temperature formalism: A cylinder in a Mach 12.7 5-species air

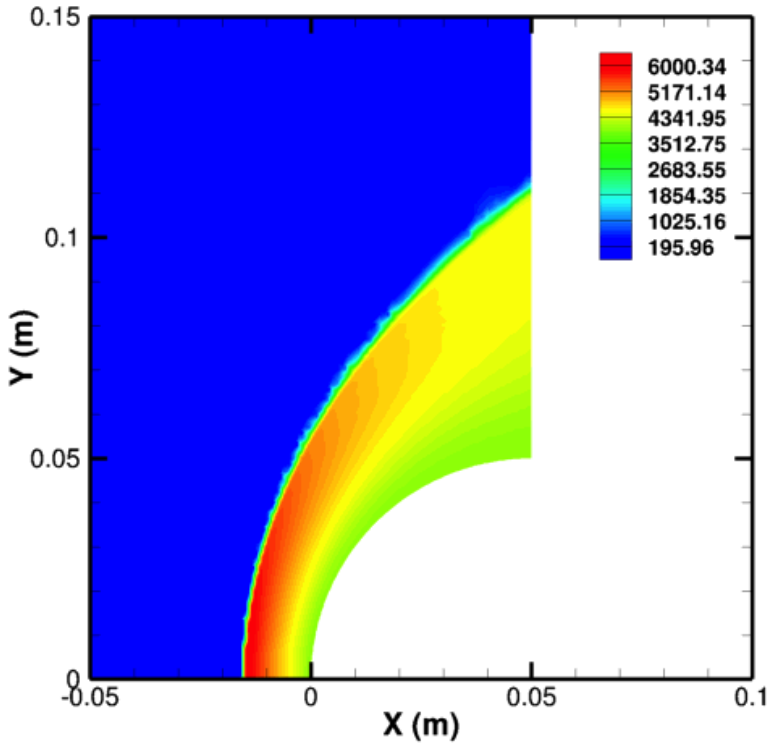

FIGURE 5.45. NO vibrational temperature contours using a multi-vibrational temperature formalism: A cylinder in a Mach 12.7 5-species air

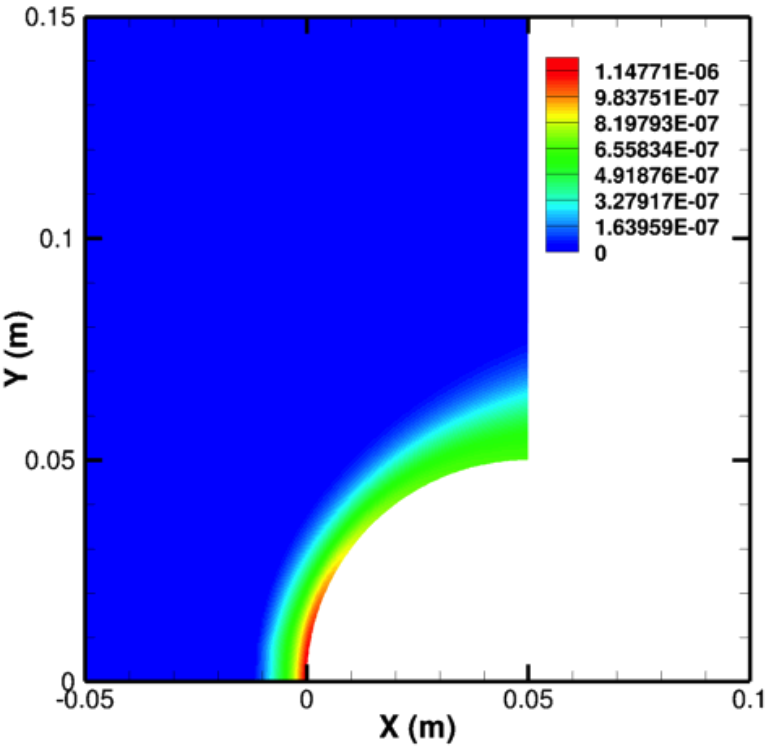

FIGURE 5.46. NO+ mole fraction contours using a multi-vibrational temperature formalism: A cylinder in a Mach 12.7 7-species air

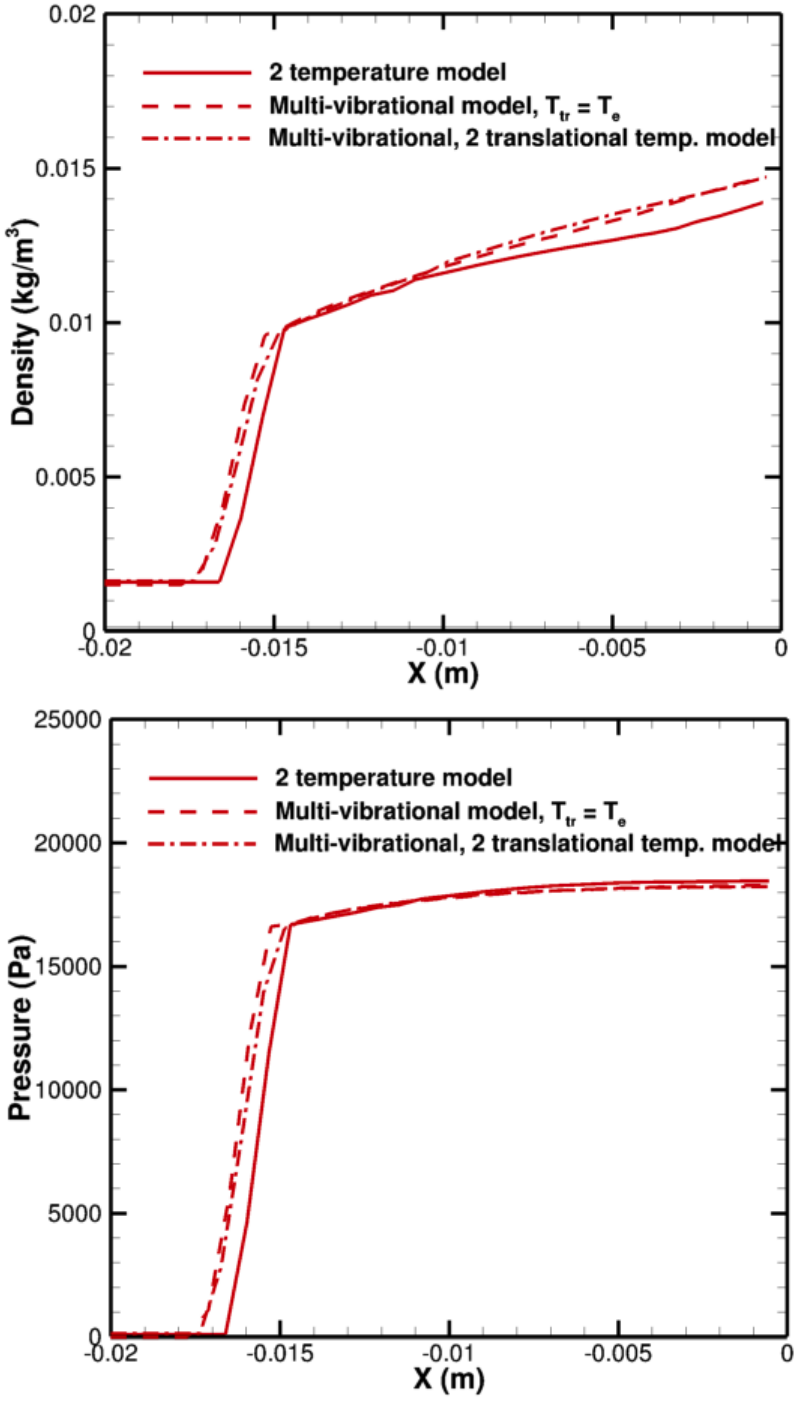

FIGURE 5.47. Stagnation line density (above) and pressure (below) for a cylinder in a 7-species Mach 12.7 air flow

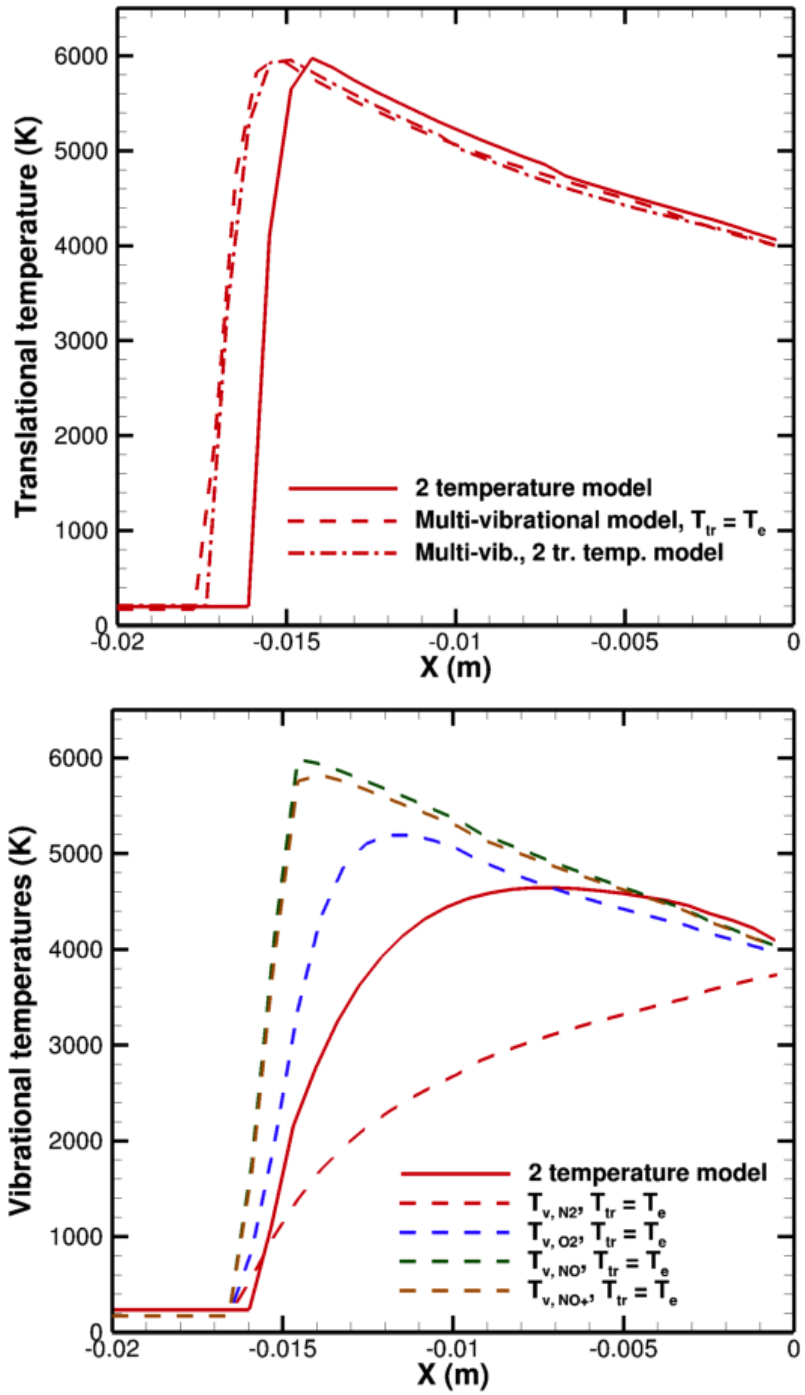

FIGURE 5.48. Stagnation line translational (above) and vibrational (below) temperatures for a cylinder in a 7-species Mach 12.7 air flow

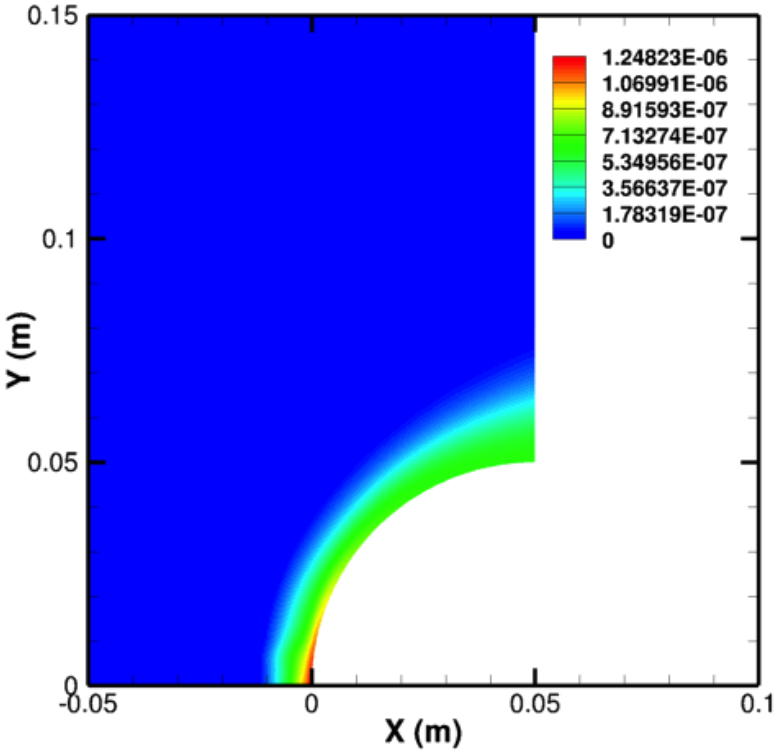

FIGURE 5.49. NO+ mole fraction contours using a multi-vibrational temperature, two translational temperature formalism: A cylinder in a Mach 12.7 7-species air

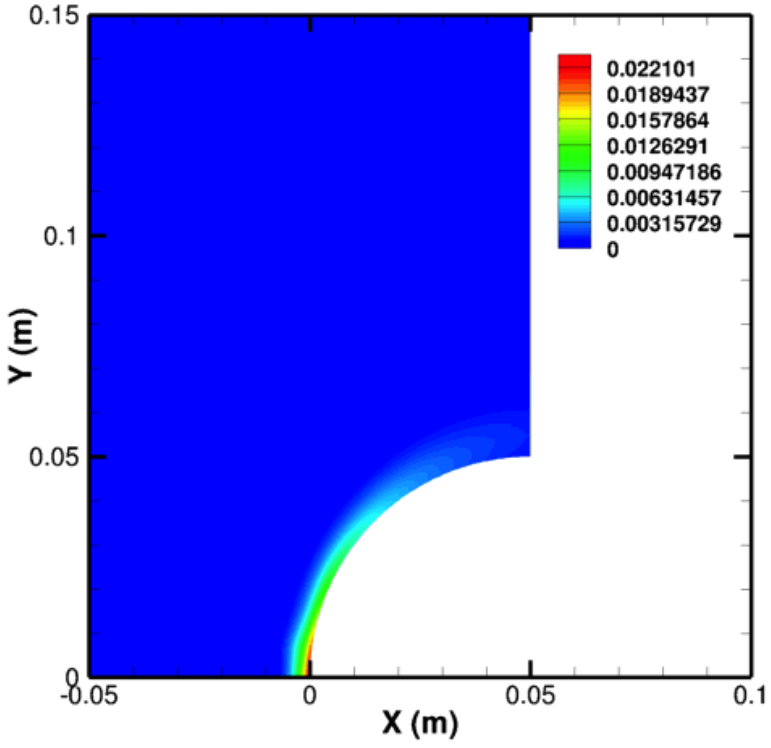

FIGURE 5.50. Plasma pressure contours using a multi-vibrational, two-translational temperature formalism: A cylinder in a Mach 12.7 7-species air

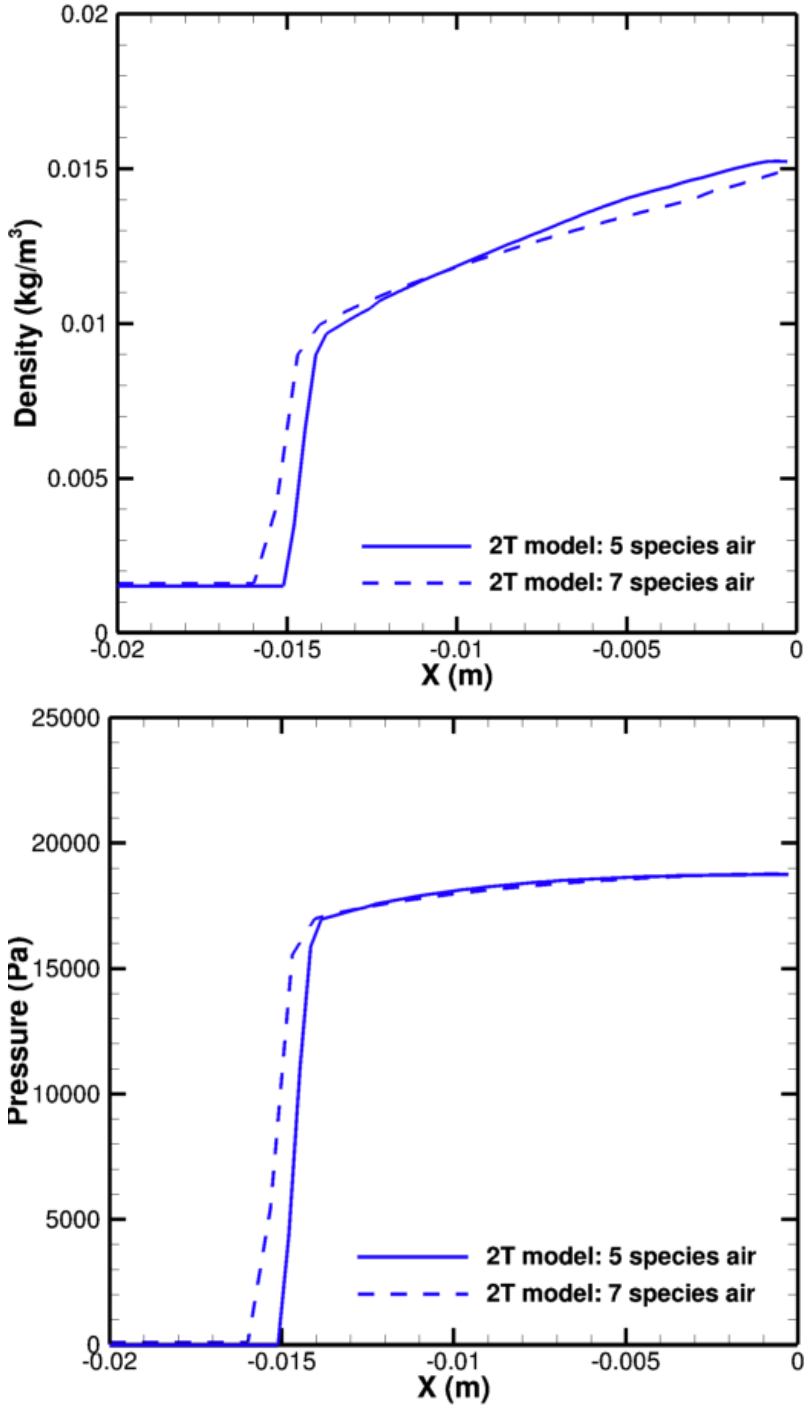

FIGURE 5.51. Stagnation line density (above) and pressure (below) for a cylinder in a 5- and 7-species Mach 12.7 air flow

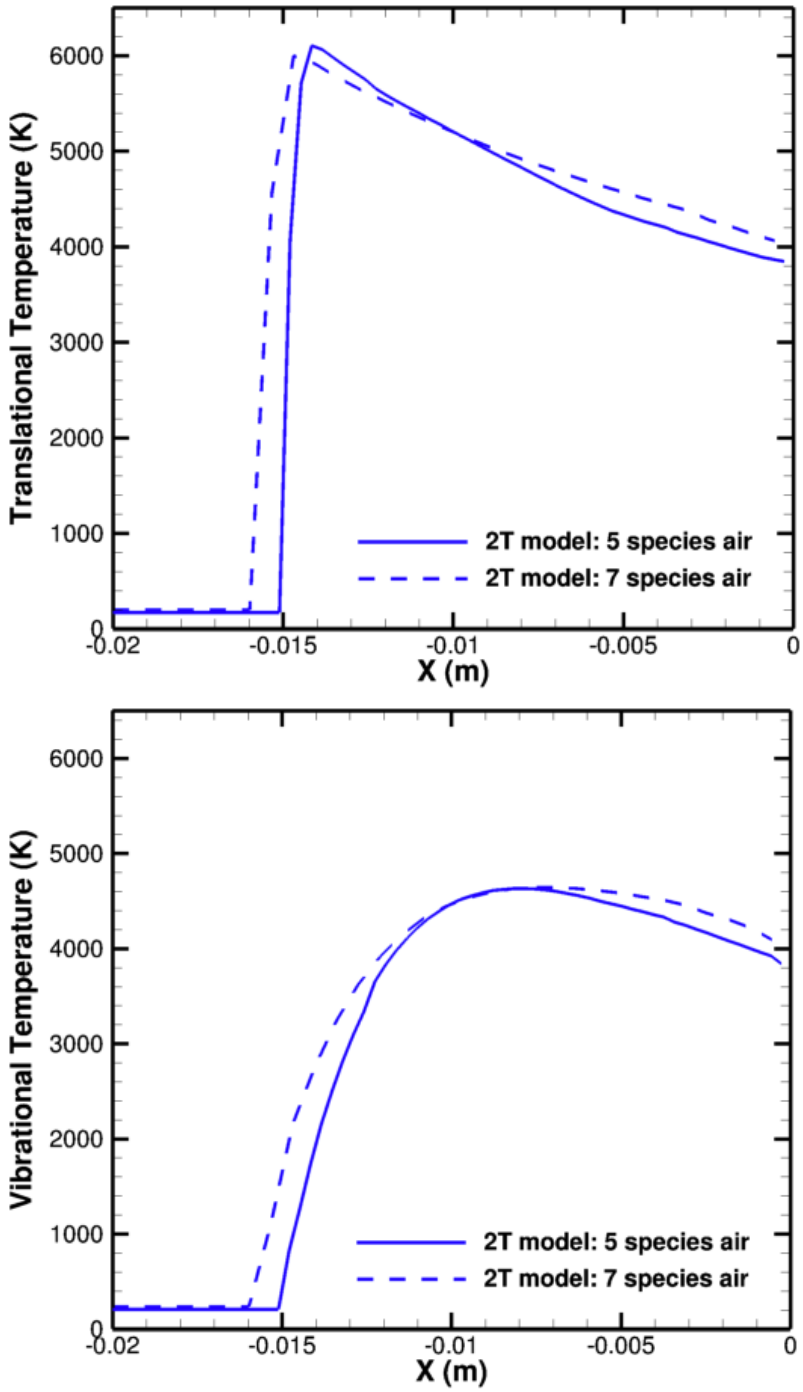

FIGURE 5.52. Stagnation line translational (above) and vibrational (below) temperatures for a cylinder in a 5- and 7-species Mach 12.7 air flow

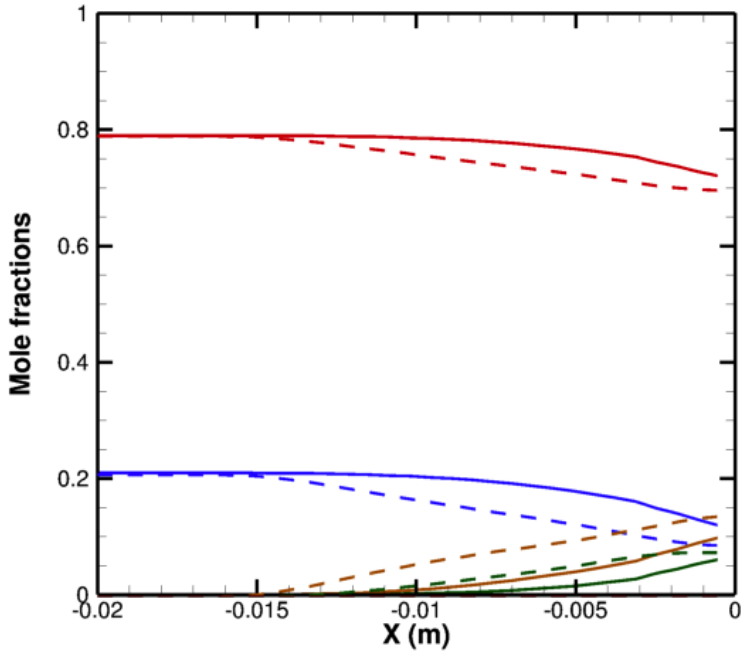

FIGURE 5.53. Comparative stagnation line mole fractions using a 2-temperature and multi-vibrational temperature for a cylinder in a 7-species Mach 12.7 air flow : —— 7-species, two temperature model; -- -- 7-species, multi-vibrational temperature model; (■: N_2 ; ■: O_2 ; ■: NO ; ■: N ; ■: O)

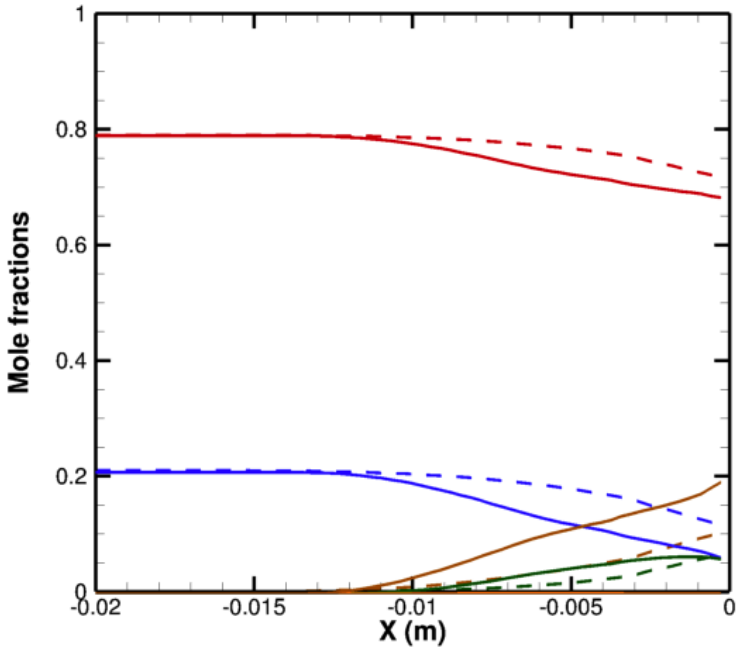

FIGURE 5.54. Comparative stagnation line mole fractions for a cylinder in a 5- and 7-species Mach 12.7 air flow: —— 5-species air chemistry; -- -- 7-species air chemistry; (■: N_2 ; ■: O_2 ; ■: NO ; ■: N ; ■: O)

CHAPTER 6
CONCLUSIONS

Hypersonics has been receiving much attention since the 1980s and that interest contiues [80], [81]. The initial establishment of a set of governing equations was based on a Boltzmann energy distribution for all the energy modes representative of the gas mixture under consideration. Typically, the governing equations were based on the assumption of such an energy distribution and harmonic oscillators in the flow. Upon verifying the validity of these assumptions, researchers discovered that anharmonicity considerations and non-Boltzmann distributions are important for expanding flows. The use of master-equations and therefore state-to-state modeling, and more recently, reduced order modeling, have helped to more accurately represent hypersonic flow fields under a variety of conditions. However, such modeling increases the computational cost of simulations for multi-dimensional flows and have not been able to replace the relative ease of implementation of multi-temperature models initially developed in the field based on simple shock tube experiments.

6.1 Numerical Implementation

The present work involved the implementation of 4 types of non-equilibrium flow capabilities on an object oriented programming platform:

(i) The first framework was to implement chemical non-equilibrium modeling, with all modes of the particles of the gas mixture being represented by a single temperature.

(ii) The second framework was to include the set of governing equations that account for conservation of vibrational energy of all polyatomic molecules considered together, leading to a two temperature formalism. The reaction rates for this two temperature formalism was based on Park's $\sqrt{TT_v}$ model. This model has been widely implemented in several hypersonics codes, and continues to be one which is heavily relied upon.

(iii) The third framework involved expanding the two temperature formulation to a multi-vibrational, single translational temperature model where each polyatomic molecule in the

system is represented by its own vibrational temperature.

(iv) Finally, in order to account for low temperature, weakly ionized plasmas that most accurately represent most re-entry flowfields, the multi-vibrational, single translational temperature model was expanded to a multi-vibrational, two translational temperature model. In the latter model, the light electrons are assumed to be possess a different temperature than all other heavy particles in the system. This separate representation of electron temperature was achieved through coupling the electron energy equation to the total energy conservation, species mass conservation and vibrational energy conservation equations.

Thus, computationally, this dissertation work represents the implementation of a strongly coupled non-equilibrium thermo-chemical library and $N_s + N_{s,m} + 1$ set of coupled governing conservation equations, where N_s represents the number of reacting species in the chemical reaction set and $N_{s,m}$ represents the number of polyatomic species used to represent the flow field.

6.2 Conclusions from Finite Heat Bath Results

The governing equations implemented were initially validated by considering the thermo-chemical non-equilibrium relaxation rates and two-dimensional hypersonic flow fields. The thermal relaxation rate for a dilute gas system was successfully validated with results obtained by Boyd and Josyula [56] using their CFD and DSMC codes. The case used by them involved a gas represented by a translational temperature of 10000 K and a vibrational temperature of 1000 K. The use of a dilute gas mixture results in a system with very little chemical non-equilibrium at any instant in time. The reaction rate for such simulations is based on the $\sqrt{TT_v}$ model and has been widely proven to be a good empirical model in such a temperature range. The present work seeked to understand the physics captured by such models beyond the initial validation of the numerical model implemented. An O_2 dissociation reaction was studied as it is the most reactive species in the typical 5-species model used in hypersonic flow simulations. It was observed that beyond the choice of a 10% by volume of the dissociating gas in a gas mixture, chemical non-equilibrium effects

play a significant role in the relaxation rates observed. The non-equilibrium relaxation curves exhibited a non-linearity in thermal equilibration, with the non-linear effects further enhanced by considering an impacting inert molecule as against an impacting inert atom. The Millikan-White empirial mixing model that accounts for V-T collisions is one significant contributing factor to this enhanced non-linearity. If a non-preferential model where the reaction rate is governed by the translational temperature is used instead of Park's $\sqrt{TT_v}$ model, significantly different chemistry was observed in the time scales between a nano- and a micro-second. Reduced pressures by an order of magnitude below 1 atmospheric pressure resulted in enhanced times to equilibrium by nearly two orders of magnitude for system dilution levels beyond 10% by volume. Most importantly, for all such heating bath cases executed with the two-temperature thermo-chemical non-equilibrium model implemented, a distinct universal transition was noted when the initial mole fraction of the dissociating molecule was increased from 0.1 to 0.2. This transition region is not governed by any non-linear effects, although cooling of the gas due to the endothermic chemical reactions taking place is prominent.

Following the investigation of two-temperature thermo-chemical non-equilibrium relaxation rates, the multi-vibrational thermo-chemical model was examined for relaxation rates in the same temperature range of 1000 K - 10000 K. It was seen that while the final equilibrium characteristics were not altered by employing a multi-vibrational temperature formalism, there were slight alterations in the transient chemistry. The vibrational temperatures predicted by the multi-vibrational temperature models were in accordance with efficient energy transfer rates of the polyatomic gas under consideration.

6.3 Conclusions from Hypersonic Flow Simulations

After investigating the relaxation rate results for the non-equilibrium capabilities implemented under non-traditional but physically more relevant dilution levels, validations and flow physics investigations were carried out for two-dimensional hypersonic flow fields. The validations included the geometries of a cone, cylinder and a challenging flow-field of a double wedge. Good agreements were obtained between the present simulation of a cone in a

pure O_2 flow at Mach 9.42 and Spurk's numerical and experimental data [62].

The double wedge flow cases were tested for three assumptions of internal energy representation: the calorically perfect gas, the one-temperature model flow in chemical non-equilibrium, and the two-temperature model flow in thermo-chemical non-equilibrium. In addition, two sweeps were performed: a variation in freestream Mach number (M_∞ = 9, 11 and 15), and a variation in second wedge angle ($\theta_2 = 45^0$, 46.3^0 and 48^0). This multi-dimensional matrix of cases undertaken verified the type VI Edney interactions for calorically perfect gas assumptions, and more importantly, the transition of type VI to type V for any type of non-equilibrium considerations. The thermo-chemical non-equilibrium results indicated that consideration of vibrational non-equilibrium resulted in second order effects for the conditions of flow tested. The variation of the second wedge angle served to validate the results of Li et al. [72]. The normalized surface pressure variations obtained in the present work are in good agreement with those obtained by them. For these double wedge cases, an increase in freestream Mach number to 15, and a 1.8^0 increase in the second wedge angle led to significant variations in shock physics and chemistry.

Finally, a cylinder in air flow at Mach 12.7 was simulated to validate the two-temperature thermo-chemical framework implemented in the present code. This case was previously used to validate numerical results with those obtained using the Data Parallel Line Relaxation solver, which uses structured grids [49]. The shock stand-off distance was within 5% of those predicted by DPLR. In order to verify other thermo-chemical models implemented in the present code, the multi-vibrational, single translational temperature model was also used to simulate the flow over a cylinder at similar conditions. It was seen that the shock stand-off distance increased by 6% for the multi-vibrational model. Furthermore, the mole fractions in the detachment distance vary between the two-temperature model and multi-vibrational model results in congruence to the dissimilarities observed in the heating bath simulations.

The use of a multi-vibrational temperature formalism had more effect on the shock structure at Mach 12.7 than did the use of an additional electron temperature to describe the flow field. Therefore, higher fidelity non-equilibrium modeling can be deemed to be important at higher freestream Mach numbers or for flows with higher freestream temperatures. Certainly, based on the results obtained here and previous studies (see references [48], [82]

and [2]), it can be stated that the use of multiple vibrational temperatures and 7-species air chemistry model increases accuracy of results at freestream hypersonic Mach numbers of $\leqslant 18$. For Mach numbers higher than 18, and for typical sub-orbital re-entry vehicle speeds, the use of high fidelity non-equilibrium modeling including multiple vibrational temperatures and translational temperatures becomes imperative for accuracy of thermo-chemistry predictions. Results based on the present work suggest that a freestream Mach number of 10 (and corresponding freestream temperature $<$ 500 K) can be considered to be a lower limit for the importance of considering multiple vibrational temperatures in the modeling of non-equilibrium flow. Below this lower limit, a two temperature model is generally adequate to capture thermo-chemical non-equilibrium for hypersonic flows.

In the present work, the use of a 5-species chemical kinetics model resulted in a $\sim$ 7% under-prediction of shock stand-off distance compared to a more complete representation of the involved chemical kinetics using 7 species. The near-surface temperature was also increased by $\sim$ 200 K by using the 7-species air chemical kinetics model. The shock structure for hypersonic flows thus has as significant a sensitivity to chemical kinetics as thermal non-equilibrium model representations.

6.4 Key findings of numerical study

The following can be concluded from all the studies on zero-dimensional heat bath cases and two-dimensional hypersonic flow simulations:

(i) Investigative studies on thermo-chemical relaxation rates for finite heat bath results indicated non-linear and non-monotonic trends in attainment of thermal equilibrium which were enhanced by unlike molecule-molecule collisions.

(ii) Chemical non-equilibrium was observed to universally become predominant between initial dissociating gas mole fractions of 0.1 and 0.2.

(iii) Unlike Park's non-preferential $\sqrt{TT_v}$ model, a non-preferential model based on the translational temperature of the gas exhibited instantaneous changes to temperatures and no appreciable overshoot of vibrational temperature.

(iv) Equilibrium times for finite heat baths scale as the inverse of the initial pressure.

(v) The use of full-scale non-equilibrium computations can yield significantly different shock patterns and physics as against calorically perfect gas assumptions for complex flows involving shock wave interactions.

(vi) Differences in chemistry between the two-temperature and multi-vibrational temperature models in the shock detachment region for hypersonic flows form a parallelism to the transient chemistry results observed for the finite heat bath studies.

(vii) For the hypersonic flow conditions undertaken using NASCART-GT, shock structures were observed to be as sensitive to the underlying chemical kinetics as they were to the use of various thermo-chemical models.

6.5 Recommendations for future work

All the studies carried out in the present work have used diatomic molecules, more specifically, N_2, O_2, NO and NO^+. Future work can investigate the effects of using other diatomic and polyatomic molecules in the gas mixtures of interest, particularly tri-atomic molecules. The effects of using higher fidelity multi-temperature modeling can be investigated by considering such gaseous mixtures. Changes to non-equilibrium rates by introducing such molecules can also be investigated.

This work demonstrates the ability of the code developed to simulate gases and flows under a variety of non-equilibrium representations. The flow simulations were carried out using inviscid flow assumptions. Another recommendation for future work involves investigating the implemented models with viscous effects with relevant modifications made to the flow solver. In addition, the computational times associated with all the implemented models can be investigated. Nonetheless, this thesis and the implemented non-equilibrium computing capabilities provide a foundation to investigate flow physics and resulting chemistry for complex hypersonic flow fields.

REFERENCES

1. Bakos, R. Current Hypersonic Research in the USA: Advances in Propulsion Technology for High-Speed Aircraft. *Educational Notes RTO-EN-AVT-150* **Paper 10,** 1–26 (2008).

2. Candler, G.V., and Maccormack, R.W. Computation of Weakly Ionized Hypersonic Flows in Thermo-Chemical Nonequilibrium. *Journal of Thermophysics and Heat Transfer* **5,** 266–273 (1991).

3. Josyula, E., and Bailey, W.F. Governing Equations for Weakly Ionized Plasma Flowfields of Aerospace Vehicles. *Journal of Spacecraft and Rockets* **40,** 845–857 (2003).

4. Scalabrin, L.C., and Boyd, I.D. Numerical Simulation of Weakly Ionized Hypersonic Flow for Rentry Configurations. *AIAA Paper 2006-3773, San Francisco, CA* (2006).

5. Surzhikov, S.T., and Shang, J.S. Three Dimensional Simulation of Shock Layer Ionization for RAM-C II Flight Tests. *AIAA Paper 2014-1078, National Harbor, MD* (2014).

6. Park, C. Nonequilibrium Hypersonic Aerothermodynamics. *Wiley, New York* (1990).

7. Treanor, C. E. and Marrone, P. V. Effect of Dissociation on the Rate of Vibrational Relaxation. *The Physics of Fluids* **5,** 1022–1026 (1962).

8. Marrone, P.V., and Treanor, C.E. Chemical Relaxation with Preferential Dissociation from Excited Vibrational Levels. *Physics of Fluids* **6,** 1215–1221 (1963).

9. Gorshov, A.B. Effect of Physical and Chemical NonEquilibrium Processes on the Parameteres of the Near Wake Downstream of a Spacecraft. *Fluid Dynamics* **44,** 785–795 (2009).

10. Capitelli, M., Esposito, F., Kustova, E.V., and Nagnibeda, E.A. Rate coefficients for the reaction $N_2(i) + N = 3N$: a comparison of trajectory calculations and the Treanor-Marrrone model. *Chemical Physics Letters* **330,** 207–211 (2000).

11. Armenise, I., Esposito, F., and Capitelli, M. Dissociation-recombination models in hypersonic boundary layer flows. *AIAA Journal* **336,** 83–90 (2007).

12. Şakraker, I., Turchi, A., and Chazot, O. Hypersonic Aerothermochemistry Duplication in Ground Plasma Facilities: A Flight-to-Ground Approach. *Journal of Spacecraft and Rockets* **52,** 1273–1282 (2015).

13. Limbaugh, C.C., Felderman, E.J., Carver, D.B., and Spinetti, R.L. Plasma Aerodynamics Test Techniques. *AIAA 2000-2449, Denver, CO* (2000).

14. Magin, T.E., Panesi, M., Bourdon, A., Jaffe, R., and Schwenke, D. Internal Energy Excitation and Dissociation of Molecular Nitrogen in a Compressing Flow. *Center for Turbulence Research, Annual Research Briefs,* 59–70 (2009).

15. Park, C. Thermochemical Relaxation in Shock Tunnels. *Journal of Thermophysics and Heat Transfer* **20,** 689–698 (2006).

16. Bose, D., and Candler, G.V. Thermal Nonequilibrium Rates of the Zeldovich Reactions. *AIAA Paper 97-0133, Reno, NV* (1997).

17. Park, C. Assessment of Two-Temperature Kinetic Model for Ionizing Air. *Journal of Thermophysics* **3,** 233–244 (1989).

18. Park, C. The Limits of Two-Temperature Model. *AIAA Paper 2010-911, Orlando, FL* (2010).

19. Park, C. Rotational Relaxation of N_2 Behind a Strong Shock Wave. *Journal of Thermophysics and Heat Transfer* **18,** 527–533 (2004).

20. Kim, J.G., and Boyd, I.D. Thermochemical Nonequilibrium Modeling of Electronically Excited Molecular Oxygen. *AIAA 2014-2963, Atlanta, GA* (2014).

21. Sharma, S.P., and Gillespie, W. Nonequilibrium and Equilibrium Shock Front Radiation Measurement. *Journal of Thermophysics and Heat Transfer* **5,** 257–265 (1991).

22. Panesi, M., Jaffe, R.L., Schwenke, D.W., and Magin, T.E. Rovibrational internal energy transfer and dissociation of $N_2(^1\Sigma_g^+)$-$N(^4S_u)$ system in hypersonic flows. *Journal of Chemical Physics* **138,** 044312:1–16 (2013).

23. Adrienko, D.A., and Boyd, I.D. Rovibrational energy transfer and dissociation in O_2-O collisions. *Journal of Chemical Physics* **144,** 104301:1–19 (2016).

24. Lee, J. H. Electron-Impact Vibration Excitation Rates in the Flowfield of Aeroassisted Orbital Transfer Vehicles. *AIAA Paper 1985-1035, Williamsburg, VA* (1985).

25. Bourdon, A., and Vervisch, P. Electron-Vibration Energy Exchange Models in Nitrogen Plasma Flows. *Physical Review E (Statistical Physics, Plasmas, Fluids, and Related Interdisciplinary Topics)* **55,** 4634–4641 (1997).

26. Kim, M., Gülhan, A., and Boyd, I.D. Modeling of Electron Energy Phenomena in Hypersonic Flows. *Journal of Thermophysics and Heat Transfer* **26,** 244–257 (2011).

27. Guy, A., Bourdon, A., and Perrin, M.-Y. Consistent Multi-Internal-Temperature Models for Vibrational and Electronic Nonequilibrium in Hypersonic Nitrogen Plasma Flows. *Physics of Plasmas* **22,** 043507:1–16 (2015).

28. Gupta, R.N., Yos, J.M., Thompson, R.A., and Lee K.-P. A Review of Reaction Rates and Thermodynamic and Transport Properties for an 11-Species Air Model for Chemical and Thermal Non-Equilibrium Calculations to 30,000 K. *NASA RP-1232, Hampton, VA* (1990).

29. Liu, Y., Panesi, M., Sahai, A., and Vinokur, M. General Multi-Group Macroscopic Modeling for Thermo-Chemical Non-Equilibrium Gas Mixtures. *Journal of Chemical Physics* **142,** 134109:1–17 (2015).

30. Munafo, A., Venturi, S., Macdonald, R., and Panesi, M. State-to-State and Reduced-Order Models for Recombination and Energy Transfer in Aerothermal Environments. *AIAA 2016-0505, San Diego, CA* (2016).

31. Grasso, F., and Capano, G. Modeling of Ionizing Hypersonic Flows in Nonequilibrium. *Journal of Spacecraft and Rockets* **32,** 217–224 (1995).

32. Boyd, I. D. Modeling of Associative Ionization Reactions in Hypersonic Rarefied Flows. *Physics of Fluids* **19,** pp. 096102:1–10 (2007).

33. Farber, E.D. Kinetic Simulation of Rarefied and Weakly Ionized Hypersonic Flow Fields. *Ph.D. Thesis, Ann Arbor, MI,* (2010).

34. Qian, J.-W., Zhang, H.-L., and Xia, M.-Y. Modelling of Electromagnetic Scattering by a Hypersonic Cone-Like Body in Near Space. *International Journal of Antennas and Propagation* (2017).

35. Kim, M., Keidar, M., and Boyd, I.D. Analysis of an Electromagnetic Mitigation Scheme for Reentry Telemetry Through Plasma. *Journal of Spacecraft and Rockets* **45,** 1223–1229 (2008).

36. Gillman, E.D., Foster, J.E., and Blankson, I.M. Review of Leading Approaches for Mitigating Hypersonic Vehicle Communications Blackout and a Method of Ceramic Particulate Injection via Cathode Spot Arcs for Blackout Mitigation. *NASA Technical Report 2010-216220, E-17194, Cleveland, OH* (2010).

37. Yuan, K., Yao, M., Shen, L., Deng, X., and Hong, L. Studies on the Effect of Angle of Attack on the Transmission of Terahertz Waves in Reentry Plasma Sheaths. *Progress in Electromagnetics Research M* **54,** 175–182 (2017).

38. Shang, J.S. Three decades of accomplishments in computational fluid dynamics. *Progress in Aerospace Sciences* **40,** 173–197 (2004).

39. Munafo, A., Panesi, M. and Magin, T. E. Boltzmann rovibrational collisional coarse-grained model for internal energy excitation and dissociation in hypersonic flows. *Physical Review E* **89,** 1–13 (2014).

40. Candler, G.V. The Computation of Weakly Ionized Hypersonic Flows in Thermo-Chemical Nonequilibrium. *Ph.D. Thesis, Department of Aeronautics and Astroanutics, Stanford University, Stanford, CA* (1988).

41. Lee, J. H. Basic Governing Equations for the Flight Regimes of Aeroassisted Orbital Transfer Vehicles. *Progress in Aeronautics and Astronautics* **96,** 3–53 (1985).

42. Millikan, R. C., and White, D. R. Systematics of Vibrational Relaxation. *Journal of Chemical Physics* **39,** 3209–3213 (1963).

43. Park, C. Calculation of Nonequilibrium Radiation in the Flight Regimes of Aeroassisted Orbital Transfer Vehicles. *Progress in Aeronautics and Astronautics* **96,** 395–418 (1985).

44. Taylor, R.L., Camac, M., and Feignberg, R.M. Measurements of Vibration-Vibration Coupling in Gas Mixtures. *Proceedings of the Eleventh Symposium on Combustion,* 49–65 (1966).

45. Lee, J. H. Electron-Impact Vibrational Excitation Rates in the Flowfield of Aeroassisted Orbital Transfer Vehicles. *Progress in Aeronautics and Astronautics* **103,** 197–224 (1986).

46. Tu, S. Development of a Solution Adaptive Cartesian-grid Solver for 2-D Thermochemical Nonequilibrium Flows. *Ph.D. Thesis, Georgia Institute of Technology, Atlanta, GA* (2001).

47. Kim, S.-S., Kim, C., Rho, O.-H., and Hong, S.K. Cures for the Shock Instability: Development of a Shock-Stable Roe Scheme. *Journal of Computational Physics* **185,** 342–374 (2003).

48. Kim, K. H., Kim, C., and Rho, O.-H. Methods for the accurate computations of hypersonic flows, I. AUSMPW+ Scheme. *Journal of Computational Physics* **174,** 38–80 (2001).

49. Lee, J.W. Parallelized Cartesian Grid Methodology for Non-Equilibrium Hypersonic Flow Analysis of Ballutes. *Ph.D. Thesis, School of Aerospace Engineering, Georgia Insitute of Technology, Atlanta, GA* (2007).

50. Ruffin, S. M., and Park, C. Vibrational relaxation of anharmonic oscillators in expanding flows. *Journal of Spacecraft and Rockets* **30,** 59–68 (1993).

51. Kim, J. G., and Boyd, I. D. Master Equation Study of Hydrogen Relaxation Using Complete Sets of State-to-state Transition Rates. *AIAA 2012-0362, Nashville, TN* (2012).

52. Tietelbaum, H. Non-equilibrium thermal dissociation of diatomic molecules. I. Extraction of collision-induced rate constants from experimentally measured reaction rates as a function of temperature for ten diatomic molecules dilute in Ar. *Journal of Chemical Physics* **124,** 55–76 (1988).

53. Landrum, D. B., and Candler, G. V. Vibrational-Dissociation Coupling in Nonequilibrium Flows. *Journal of Thermophysics and Heat Transfer* **6,** 643–649 (1992).

54. Gonzales, D. A., and Varghese, P. L. Vibrational relaxation models for dilute shock heated gases. *Journal of Chemical Physics* **195,** 83–91 (1995).

55. Andrienko, D. A. and Boyd, I. D. Master Equation Study of Vibrational and Rotational Relaxations of Oxygen. *Journal of Thermophysics and Heat Transfer* **30,** 533–552 (2016).

56. Boyd, I. D., and Josyula, E. State-Resolved Vibrational Relaxation Modeling for Strongly Nonequilibrium Flows. *Physics of Fluids* **23,** 057101:1–9 (2011).

57. Borgnakke, C., and Larsen, P. S. Statistical collision model for Monte Carlo simulation of polyatomic gas mixture. *Journal of Computational Physics* **18,** 405–420 (1975).

58. Zhang, W., Lani, A. and Panesi, M. Analysis of non-equilibrium phenomena in inductively coupled plasma generators. *Physics of Plasmas* **23,** 073512 (2016).

59. Knab, O., Freuhauf, H. -H. and Messerschmid, E. W. Theory and validation of the physically consistent coupled vibration-chemistry-vibration model. *Journal of Thermophysics and Heat Transfer* **9,** 219–226 (1995).

60. Macharet, S. O., and Adamovich, I. V. Semiclassical modeling of state-specific dissociation rates in diatomic gases. *Journal of Chemical Physics* **113,** 7351–7361 (2000).

61. Candler, G. On the Computation of Shock Shapes in Nonequilibrium Hypersonic Flows. *AIAA-89-0312, Reno, NV* (1989).

62. Spurk, J. H. Experimental and Numerical Nonequilibrium Flow Studies. *AIAA Journal* **8,** 1039–1045 (1970).

63. Camac, M., and Vaughan, A. O_2 dissociation rates in O_2-Ar mixtures. *Journal of Chemical Physics* **34,** 460–470 (1961).

64. Park, C. Review of chemical-kinetic problems of future NASA missions. I –Earth entries. *Journal of Thermophysics and Heat Transfer* **7,** 633–648 (1993).

65. Stupochenko, E. V., Losev, S. A., and Osipov, A. I. Relaxation in Shock Waves. *Springer-Verlag, Berlin,* 258–286 (1967).

66. Olejniczak, J., Wright, M. J. and Candler, G. V. Numerical study of inviscid shock interactions on double-wedge geometries. *Journal of Fluid Mechanics* **352,** 1–25 (1997).

67. Bertin, J. J., and Hinkle, J. C. Experimental investigation of supersonic flow past double wedge configurations. *AIAA Journal* **13,** 897–901 (1975).

68. Edney, B. Anomalous heat transfer and pressure distributions on blunt bodies at hypersonic speeds in the presence of an impinging shock. *Rep. 115. Flygetkniska Forsoksanstalten (The Aeronautical Research Institute of Sweden)* (1968).

69. Coratekin, T., van Keuk, J. and Ballman, J. Performance of Upwind Schemes and Turbulence Models in Hypersonic Flows. *AIAA Journal* **42,** 945–957 (2004).

70. Liou, M. S. and Steffen, C. J. A New Flux Splitting Scheme. *Journal of Computational Physics* **107,** 23–39 (1993).

71. Wada, Y. and Liou, M. S. An Accurate and Robust Flux Splitting Scheme for Shock and Contact Discontinuities. *SIAM Journal on Scientific Computing* **18,** 633–648 (1997).

72. Li, J., Zhu, Y. and Luo, X. On Type VI-V transition in hypersonic double-wedge flows with thermo-chemical non-equilibrium effects. *Physics of Fluids* **26,** 1–16 (2014).

73. Hu, Z. M., Wang, C., Zhang, Y., and Myong, R. S. Computational confirmation of an abnormal Mach reflection wave configuration. *Physics of Fluids* **21** (2009).

74. Grasso, F., Purpura, B., Chanetz, B., and Delery, J. Type III and type IV shock/shock interferences: Theoretical and environmental aspects. *Journal of Aerospace Science and Technology* **7** (2003).

75. Xiong, W., Zhu, Y., and Luo, X. On transition of type V interaction in double-wedge flow with non-equilibrium effects. *Theoretical and Applied Mechanics Letters* **6,** 282–285 (2016).

76. Ait-Ali-Yahia, D., and Habashi, W. G. Finite Element Adaptive Method for Hypersonic Thermochemical Nonequilibirum Flows, *AIAA Journal* **35,** 1294–1302 (1997).

77. Liepmann, H. W. and Roshko, A. Elements of Gasdynamics. *John Wiley & Sons, New York/London/Sidney* (1966).

78. Billig, F. Shock-wave shapes around spherical-and cylindrical-nosed bodies. *Journal of Spacecraft and Rockets* **4,** 822–823 (1967).

79. Sharma, M., Austin, J. M., Glumac, N. G. and Massa, L. NO and OH Spectroscopic Vibrational Temperature Measurements in a Postshock Relaxation Region. *AIAA Journal* **48,** 1434–1443 (2010).

80. Bertin, J. J., and Cummings, R. M. Fifty years of hypersonics: where we've been, where we're going. *Progress in Aerospace Sciences* **39,** 511–536 (2003).

81. Schmisseur, J. D. Hypersonics into the 21st century: A perspective on AFOSR-sponsored research in aerothermodynamics. *Progress in Aerospace Sciences* **72,** 3–16 (2015).

82. Josyula, E. and Shang, J. S. Computation of Nonequilibrium Hypersonic Flowfields Around Hemisphere Cylinders. *Journal of Thermophysics and Heat Transfer* **7,** 668–679 (1993).